Synthesis and luminescence properties of Bi^{3+}, Yb^{3+} co-doped Y_2O_3 phosphor powder and thin film for application in solar cells

by

Edward Lee

Bachelor of Science Honours: Physics

A dissertation submitted in accordance with the requirement for a degree

Magister Scientiae: Physics

in the

Department of Physics

of the

Faculty of Natural and Agricultural Sciences

at the

University of the Free State

Supervisor: Professor Hendrik C Swart

Co-supervisor: Professor Jacobus J Terblans

Acknowledgements

I would like to express my sincere gratitude to the following individuals without which this thesis would be impossible:

- My parents, George and Tammy Lee and my sister Michelle for their continuous support through difficult times.
- Prof H.C. Swart, my supervisor for his mentorship, positive attitude, guidance and support throughout this study.
- Prof J.J. Terblans, my co-supervisor for his mentorship, positive attitude and support throughout this study.
- Prof R.E. Kroon, for his assistance with the photoluminescence measurement and for his invaluable advices.
- Ms P.P. Mokoena, for all her patience and assistance with the field-emission scanning electron microscope measurements.
- Dr. S. Cronjé for his guidance and support with the X-ray diffractometer.
- Prof E. Coetsee-Hugo for her assistance in X-ray photoelectron spectroscopy measurements.
- Dr M.M. Duvenhage for her help with time-of-flight secondary ion mass spectroscopy measurements.
- Dr. V. Craciun, Dr. D. Craciun and Ms. O. Fufa from the National Institute for Laser, Plasma and Radiation Physics, Magurele, Romania, for their assistance in pulsed laser deposition synthesis and X-ray diffraction measurements.
- Prof P. Bergman from Linköping University, Sweden, for this help with life-time measurements.
- Mr. L.J.B. Erasmus for his assistance in photoluminescence measurements and his help with the pulsed laser deposition synthesis.
- Ms K. Cronjé and Mrs Y. Loots, the secretaries of the Department of Physics for their help with administrative tasks during my studies.
- To my friends and colleagues for their fruitful discussion and encouragement through my studies.

Abstract

Solar cells based on Si are currently the most widely studied and adopted form of photovoltaic cells used to convert solar energy into electrical energy. However, Si solar cells are known for its poor conversion efficiencies due to the spectral mismatch between the solar spectrum and the absorption spectrum of the Si solar cell.

This study focuses on synthesising the Y_2O_3:Bi^{3+},Yb^{3+} phosphor powder using the co-precipitation technique. Various parameters such as: varying the pH levels, Bi^{3+} and Yb^{3+} concentrations during preparation in order to so study their effect on the structural and luminescence properties of the phosphor. After optimisation of the above mentioned parameters, Y_2O_3:Bi^{3+},Yb^{3+} thin films were prepared using the spin coating and pulsed laser deposition techniques.

The X-ray diffraction patterns showed that the Y_2O_3:Bi^{3+},Yb^{3+} phosphor powders all crystallised as a single phase cubic structure even at high doping concentrations. While in the thin films the monoclinic phase of Y_2O_3 was present in addition to the single phase cubic structure. The results from the diffraction patterns also revealed that the crystallite size of the phosphor powders was mostly dependent on the pH during the synthesis process rather than the concentration of the dopants present in the host. Using a scanning electron microscope, it was found that the surface morphology of the thin films varied significantly between the two preparation techniques. The spin coating technique yielded smooth films but at higher molarities and with an increased number of coatings the films started cracking and peeling due to the poor adhesion between the substrate and the film. With the pulsed laser deposition technique, the films adhered to the substrate very well but were significantly rougher. Films prepared using the KrF laser had only some particulates present on the films, while the films prepared using the Nd:YAG laser were covered with particulates.

X-ray photoelectron spectroscopy and energy dispersive spectroscopy results provided proof that the dopants Bi^{3+} and Yb^{3+} were successfully incorporated into the host material and that they were homogenously spread throughout the material.

The photoluminescence spectra showed and confirmed that the dopants may occupy two sites within the host material namely, the S_6 and C_2 sites. With an increase in the Bi^{3+} and Yb^{3+} ion concentration an increase in the visible and infrared emission intensity, respectively, was observed. Both the visible and infrared emission intensities increased up to a certain molarity (Bi^{3+} = 2.0 mol% and Yb^{3+} = 10.0 mol%) before decreasing dramatically due to concentration quenching. For the cathodoluminescence spectra the results showed that with an increase in the Bi^{3+} concentration a decrease in the emission intensity ratio between the S_6 and C_2 sites occurred due to the limited available S_6 sites. However, by introducing the Yb^{3+} ions some of the Bi^{3+} ions were forced to occupy some of the unoccupied S_6 sites leading to an increase in the Bi^{3+} emission intensity originating from the S_6 site. The photoluminescence of the thin films was also studied and found to be similar to that obtained from the bulk powder samples. With an increase in the molarity and an increase in the number of coatings, the emission intensity prepared using the spin coating also increased due to more material being present on the substrate. As for the films prepared using pulsed laser deposition the film that was prepared at a high substrate temperature had a significantly lower emission intensity than the film prepared at a lower substrate temperature. Both the spin coating and pulsed laser deposition prepared thin films exhibit visible and more importantly infrared emission, which may be used to modify the solar spectrum with the aim of improving the efficiency of solar cells.

Abbreviations

Ammonium hydroxide	-	NH_4OH
Arbitrary units	-	arb.u.
Bismuth^{3+}	-	Bi^{3+}
Bismuth oxide	-	Bi_2O_3
Caesium		Cs
Carbon	-	C
Cathodoluminescence	-	CL
Copper	-	Cu
Energy dispersive X-ray spectroscopy	-	EDS
Full width at half maximum	-	FWHM
Hydroxide	-	OH
Near-infrared	-	NIR
Nitric acid	-	HNO_3
Oxygen^{2-}	-	O^{2-}
Photoluminescence	-	PL
Photomultiplier tube	-	PMT
Pulsed laser deposition	-	PLD
Quantum efficiency	-	QE
Rare earth	-	RE
Scanning electron microscopy	-	SEM
Silicon	-	Si
Time-of-flight secondary ion mass spectroscopy	-	TOF SIMS
Ultraviolet	-	UV
Visible	-	Vis
Water	-	H_2O
Xenon		Xe
X-ray diffraction	-	XRD
X-ray photoelectron spectroscopy	-	XPS
Ytterbium^{3+}	-	Yb^{3+}
Ytterbium oxide	-	Yb_2O_3
Yttrium oxide	-	Y_2O_3

Table of Contents

Chapter 1: Introduction

1.1 Literature review

As the global population continues to increase so does the demand for energy. Currently the primary sources of energy consist of: nuclear energy, fossil fuels (such as natural gas, oil and coal) and renewable energy (like solar wind and hydro) [1]. Electrical energy produced using fossil fuels generates a large amount of carbon dioxide and other pollutants which causes health risks. Nuclear energy produces almost no carbon dioxide but presents radioactive waste hazards. On the other hand, energy produced from a renewable source releases almost no pollution thus posing little to no health risks. Solar energy is becoming a very popular form of energy. It is more reliable due to the absence of any mechanical part, it is also able to work year-round with moderate operations cost [2]. Despite all the benefits, solar cells constructed from single junction crystalline silicon suffer from low conversion efficiencies due to the mismatch between the band gap of the semiconductor and energy distribution of the solar spectrum as shown in Figure 1.1 [3]. As a result, researchers have developed solar cells which consist of multiple p-n junctions which are responsible for absorbing different wavelengths present in the solar spectrum [4]. Due to their high cost of manufacturing, multi-junction solar cells are however only used in very specialised situations such as in aerospace. For consumers, single junction amorphous or crystalline silicon is still the most economical option. Improving the efficiency of single junction solar cells that are already in service and those still to be manufactured is thus highly desired.

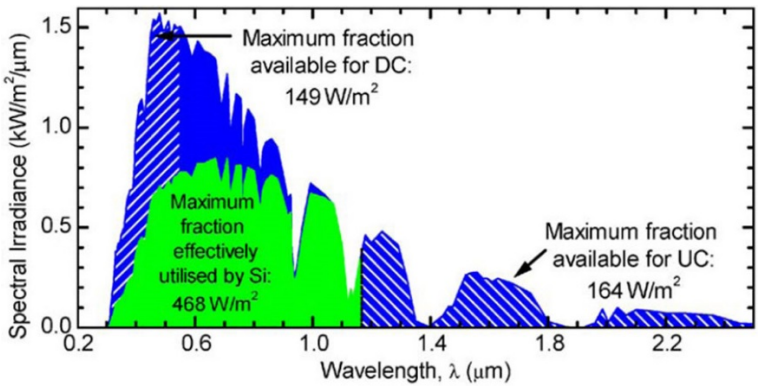

Figure 1.1 Solar spectrum absorbed by crystalline silicon solar cell in addition to regions that are suitable for up-conversion (UC) or down-conversion (DC) [5].

Luminescent materials have and will continue to play an important role in society for their role in lighting and electronic displays [6]. As the properties of luminescent materials are well documented, researchers have shown their potential to enhance the efficiency of solar cells [7,8]. Thus, focus has been placed on synthesising luminescent materials that can convert the broad solar spectrum into photons that can be more efficiently utilised in solar cells. In the case of silicon based solar cells, the maximum absorption occurs in the near-infrared region (NIR) at around 1000 nm.

The proposition of using luminescent materials to down or up convert the solar spectrum for improving the efficiency of silicon based solar cells was theorised by Trupke et al in 2002 [7,8]. In the past decade, very intensive research has been done focusing on the effect of down-conversion/shifting of ultraviolet or visible photons to near-infrared photons. Phosphors with co-doped Ln^{3+} - Yb^{3+} (Ln = Tb, Pr, Nd, Er and Tm) have been of great interest for developing highly efficient solar cells [9,10]. The Yb^{3+} ion in this system serves as the most preferable acceptor and emitter due to the NIR emission in the region of 900 nm to 1100 nm, which closely matches the optimal spectral response of crystalline silicon (c-Si) solar cells [9]. Chen et al. demonstrated an efficient NIR down-conversion in Ce^{3+} - Yb^{3+} co-doped YBO_3 phosphor [3]. The research showed a cooperative energy transfer (CET) from Ce^{3+} to Yb^{3+} ions where an absorbed UV photon (358 nm) resulted in the emission of two NIR photons (approximately 973 nm). The energy transfer from Ce^{3+} to Yb^{3+} was proven when a single doped YBO_3: Yb^{3+} phosphor was excited by 358 nm light and no emission peaks between 900 nm to 1100 nm were observed. Due to the parity forbidden 4f-4f transition, lanthanides are generally poor at absorbing photons in the UV and blue regions [3,9]. Lanthanides also have narrow absorption lines which prevent the ions from absorbing a significant part of the solar spectrum [11]. An experiment performed by Wei et al., showed the possibility of quantum-cutting down-conversion where two NIR photons could be generated from one UV photon through a cooperative energy transfer process in a Bi^{3+} - Yb^{3+} co-doped Y_2O_3 phosphor [12]. Under UV excitation, the NIR emission from Yb^{3+} was observed at around 980 nm due to the $^2F_{5/2} \rightarrow {}^2F_{7/2}$ transition. The excitation spectra obtained from the co-doped phosphor verified the energy transfer from Bi^{3+} to Yb^{3+} as the $^1S_0 \rightarrow {}^3P_1$ excitation band of Bi^{3+} that is ranging between 320 nm and 360 nm was detected when observing the Yb^{3+} emission at 979 nm. The emission spectra obtained under 325 nm excitation of the co-doped Y_2O_3:Bi^{3+},Yb^{3+} phosphor showed

strong Yb^{3+} emissions in the range between 950 nm and 1100 nm with the main emission bands at 979, 1033 and 1077 nm. Rambabu et al. demonstrate down-conversion from ultraviolet light to near-infrared emission using vanadate-based phosphor, synthesised using the co-precipitation technique [13]. The experiment showed the dependence of pH on the structure morphology and luminescent properties during synthesis of the phosphor. Similar to the product synthesised by Wei et al, the photoluminescence excitation (PLE) spectra of $Y_{0:97}VO_4:Bi^{3+}{}_{0:03}$ phosphor also showed a broad excitation band associated with the Bi^{3+} $^1S_0 \rightarrow {}^3P_1$ transition. As a result of the broad absorption band researchers such as Huang et al. has successfully synthesised a $Gd_2O_3:Bi^{3+},Yb^{3+}$ phosphor material that achieved a quantum cutting efficiency of 173.8 % [9].

1.2 Research aims and objectives

The goal of the research project was to synthesis a $Y_2O_3:Bi^{3+},Yb^{3+}$ phosphor material in the powder form and as a thin film to study its luminescence properties for possible applications in solar cells.

The project consisted of 6 objectives which were addressed as followed:

1. Synthesis and characterise the $Y_2O_3:Bi^{3+}$ phosphor powder using the co-precipitation method.
2. Study the luminescence properties of the $Y_2O_3:Bi^{3+}$ phosphor powder.
3. Investigate the effects of pH and Bi^{3+} concentration on the $Y_2O_3:Bi^{3+}$ phosphor powder.
4. Study the down-conversion property of $Y_2O_3:Bi^{3+},Yb^{3+}$ powder phosphor
5. Prepare $Y_2O_3:Bi^{3+},Yb^{3+}$ thin films using pulsed laser deposition (PLD) and spin coating.
6. Characterise the thin films.

1.3 Thesis layout

This thesis consists of eight chapters. Chapter 1 contains an introduction and a literature review about using phosphor materials to enhance solar cell efficiencies, in addition to the aims of the study. Chapter 2 includes an introduction to photoluminescence and a description of the host and dopant materials used. Chapter 3 focuses on the experiential techniques used to synthesise the phosphor powders and thin films. In chapter 4 the various characterisation techniques used are discussed. The effect of pH on the luminescent properties of Y_2O_3:Bi^{3+} is discussed in chapter 5. The dependence of Bi concentration on the luminescence properties of Y_2O_3:Bi^{3+} is presented in chapter 6. In chapter 7 the effect of varying Yb^{3+} ion concentration on the Y_2O_3:Bi^{3+},Yb^{3+} phosphor is studied. Chapter 8 compares the luminescence properties of Y_2O_3:Bi^{3+},Yb^{3+} thin films grown using the spin coating and pulsed laser deposition techniques. Finally, a summary and future work suggestions are given in chapter 9.

1.4 References

[1] O. Ellabban, H. Abu-rub, F. Blaabjerg, "Renewable energy resources : Current status , future prospects and their enabling technology", *Renew. Sustain. Energy Rev.*, **39,** 748–764 (2014)

[2] A. R. Jha, "Solar Cell Technology and Applications", *CRC Press, Taylor and Francis Group, Boca Raton, Florida*, (2009)

[3] C. J. Chen, "Physics of Solar Energy", *John Wiley & Sons, Inc., Hoboken, New Jersey*, (2011)

[4] A. Luque, S. Hegedus, "Handbook of Photovoltaic Science and Engineering", *Wiley, New York*, (2010)

[5] B. S. Richards, "Enhancing the performance of silicon solar cells via the application of passive luminescence conversion layers", *Sol. Energy Mater. Sol. Cells*, **90,** 2329–2337 (2006)

[6] A. Kitai, "Luminescent Materials and Applications", *John Wiley & Sons, Ltd, Chichester, West Sussex, England*, (2008)

[7] T. Trupke, M. A. Green, P. Würfel, "Improving solar cell efficiencies by down-conversion of high-energy photons", *J. Appl. Phys.*, **92,** 1668–1674 (2002)

[8] T. Trupke, M. A. Green, P. Würfel, "Improving solar cell efficiencies by up-conversion of sub-band-gap light", *J. Appl. Phys.*, **92,** 4117–4122 (2002)

[9] X. Y. Huang, X. H. Ji, Q. Y. Zhang, "Broadband downconversion of ultraviolet light to near-infrared emission in Bi^{3+}-Yb^{3+}-codoped Y_2O_3 phosphors", *J. Am. Ceram. Soc.*, **94,** 833–837 (2011)

[10] B. S. Richards, "Luminescent layers for enhanced silicon solar cell performance: Down-conversion", *Sol. Energy Mater. Sol. Cells*, **90,** 1189–1207 (2006)

[11] B. M. van der Ende, L. Aarts, A. Meijerink, "Lanthanide ions as spectral converters for solar cells", *Phys. Chem. Chem. Phys.*, **11,** 11081–11095 (2009)

[12] W. Xian-Tao, Z. Jiang-Bo, C. Yong-Hu, Y. Min, L. Yong, "Quantum cutting downconversion by cooperative energy transfer from Bi^{3+} to Yb^{3+} in Y_2O_3 phosphor", *Chinese Phys. B*, **19,** 77804–77809 (2010)

[13] U. Rambabu, S. Do Han, "Broad band down conversion from ultra violet light to near infrared emission in YVO_4:Bi^{3+},Yb^{3+} as spectral conversion phosphor for c-Si solar cells", *Ceram. Int.*, **39,** 1603–1612 (2013)

Chapter 2: Background theory

This chapter aims to provide the necessary background theory used to explain the results that were obtained in Chapters 4 – 7. In the first section a brief introduction on the various types of luminescence is given along with their trigger source. The next three sections focus on a detailed discussion on the absorption of radiation and the radiative and non-radiative emission mechanisms. The last section discusses the structural, chemical and luminescence properties of the Y_2O_3 host material along with the Bi^{3+} and Yb^{3+} ions used in the phosphor material.

2.1 Luminescence

Luminescence is a radiative process where a material known as phosphors, emits optical light (Infrared to UV) when stimulated with various energy sources. The type of luminescence can therefore be classified by the type of excitation source used to trigger the luminescence [1].

Table 2.1: Types of luminescence.

Phenomenon	**Type of excitation**
Bioluminescence	Biochemical reaction
Cathodoluminescence	Bombardment of electrons
Chemiluminescence	Chemical reaction
Electroluminescence	Current passing through the substance
Photoluminescence	Absorption of photons
Thermoluminescence	Heat stimulated emission of previously absorbed energy

Though different excitation sources can be used to achieve luminescence they all follow a similar mechanism. An electron is excited from a lower energy level to a higher energy level where it relaxes back to the lower level releasing energy [2]. The energy released during the transition can either be radiative or non-radiative as shown in Figure 2.1. In radiative transition energy is emitted in the form of photons, originating from defects within the phosphor material as indicated in Figure 2.1 [3]. In non-radiative transition, energy is released in the form of phonons (heat). This process is generally undesired as it leads to a decrease in the luminescence efficiency of the phosphor material, which will be discussed in section 2.4.

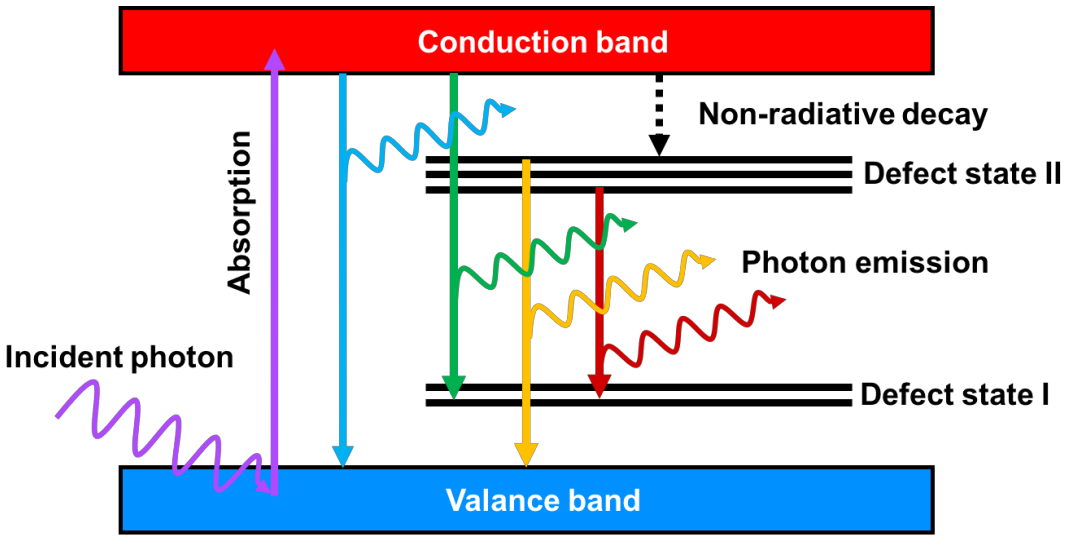

Figure 2.1 Schematic of the luminescence mechanism.

2.2 Absorption of radiation

Photoluminescence is a type of luminescence where the primary trigger for spontaneous emission are photons. If a phosphor material is radiated with photons with energies lower than the band gap, they will not be absorbed and are therefore transparent to the material. If a phosphor material absorbs photons with an energy greater or equal to its band gap the excitation of electrons to a higher energy level becomes possible. Utilising the absorption coefficient $\alpha(hv)$, the magnitude of absorption of the phosphor material can be determined by the following equation,

$$\alpha(hv) = A \sum p_{if} n_i n_f \tag{2.1}$$

where A is a constant related to the mass of the electrons and holes, n_i is the number density of occupied electronic states in the initial ground state, n_f is the number density of unoccupied electronic states in the final excited state and p_{if} represents the transition probability from a ground state to an excited state [4].

In equation (2.1) quantum mechanics requires that both the conservation of energy and the conservation of momentum are satisfied. In energy conservation, the energy difference

between the initial and final states should be equal to that of the incident photon where the condition can be represented as [4],

$$(\hbar^2/2m^*)k_f^2 = (\hbar^2/2m^*)k_i^2 + hv \tag{2.2}$$

where $\hbar$ represents Planck's constant h divided by 2π, m^* is the effective mass of the photon, v is the photon frequency, k_i and k_f are the initial and final wave vectors, respectively.

Similarly, in momentum conservation the difference between the two states should also be equal, giving rise to the following expression,

$$\hbar k_f = \hbar(k_i + q) \tag{2.3}$$

where q is the photon momentum [4].

Figure 2.2 illustrates a direct transition where the top of the valence band and the bottom of the conduction band have equal momentum. In this case the absorption coefficient (equation 2.1) can be rewritten as [4],

$$\alpha(hv) = A^*(hv - E_g)^{1/2} \tag{2.4}$$

where A^* represents a constant related to the effective mass of the electrons and holes and E_g the band gap between the valence and conduction band. In cases where the transition at $k = 0$ is forbidden due the j selection rule, the absorption coefficient in the region $k \neq 0$ is given by,

$$\alpha(hv) = A'(hv - E_g)^{3/2} \tag{2.5}$$

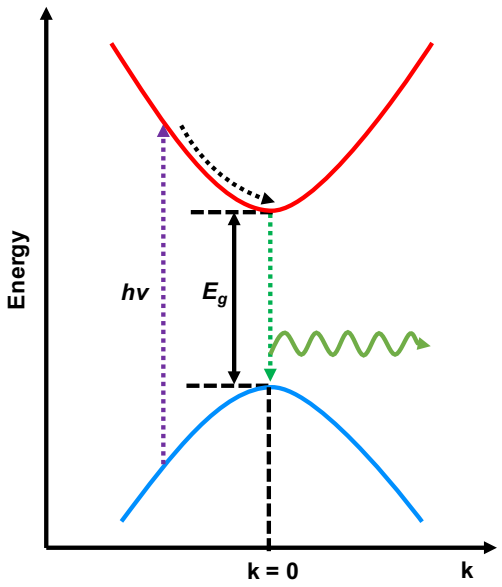

Figure 2.2: Direct transition from the valence to conduction band due to optical absorption.

In addition to direct transitions some material may exhibit indirect transitions shown in Figure 2.3. In indirect transitions, both the momentum and energy of the electrons changes when they are excited from the valence to the conduction band. As the two states no longer share the same k-value, the conservation momentum can longer be supplied by the photon. The transition therefore, required the absorption of emission of a phonon in order to complete the transition. The absorption coefficient for an indirect transition where a phonon is absorbed, is expressed as [4],

$$\alpha(hv) = A^*(hv - E_g + E_p)^2 \left(\exp\left(\frac{E_p}{k_B T}\right) - 1\right)^{-1} \tag{2.6}$$

while the absorption coefficient expression for the emission of a phonon is given by,

$$\alpha(hv) = A^*(hv - E_g - E_p)^2 \left(1 - \exp\left(\frac{E_p}{k_B T}\right)\right)^{-1} \tag{2.7}$$

where in both equations, E_p is the phonon energy, k_B is the Boltzmann constant and T the temperature.

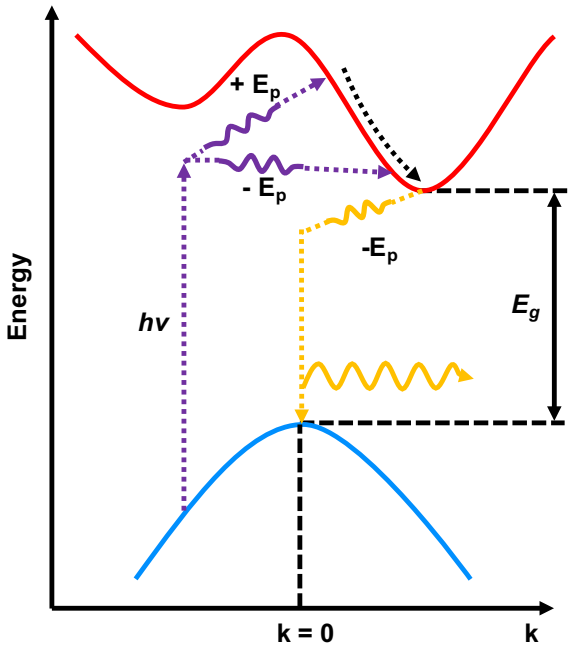

Figure 2.3: Indirect transition from the valence to the conduction band.

2.3 Radiative emission

As mentioned in the introduction, luminescence is a radiative process where electromagnetic radiation is emitted when an excited electron returns to its initial ground state. Similar to the magnitude of absorption, the magnitude of emission R can be expressed by,

$$R = B \sum p_{ul} n_u n_l \tag{2.8}$$

where B represents a constant related to the mass of the electrons and holes, n_u is the number density of electrons that occupy the upper energy states, n_l is the number density of unoccupied states in the lower energy state and p_{ul} is the transition probability from the upper state to the lower state [4]. By applying the conservation of energy and momentum Equation 2.8 can we rewritten as,

$$\alpha(hv) = B^*(hv - E_g + E_p)^{1/2} \exp\left(-\frac{hv - E_g}{k_B T}\right) \tag{2.9}$$

where, at a given temperature T electrons are located in the vicinity of the minimum region of the conduction band separated from the valence band by a band gap E_g [4].

2.3.1. Stokes shift

The photons emitted by the phosphor are generally lower in energy than the energy of the photons absorbed causing the emission spectrum to be red-shifted. This phenomenon is known as Stokes shift which can be explained through the Franck-Condon principle [5].

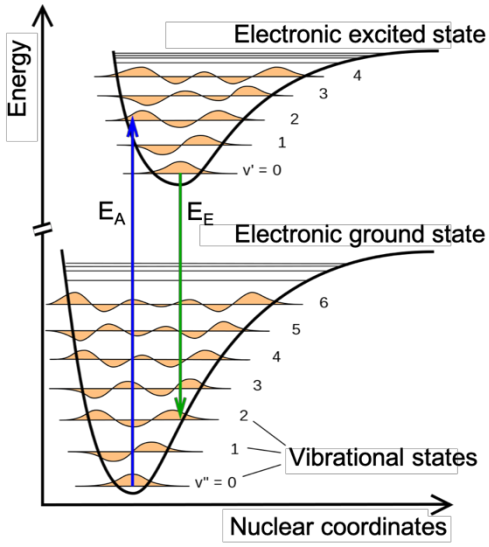

Figure 2.4: Schematic illustration of the Franck-Condon principle. Adapted from [6].

When a photon is absorbed by a molecule, it is not only a transition to an excited electronic state but, the molecule also gains some vibrational energy [5]. Figure 2.4 illustrates two potential curves of a molecule as a function of the nuclear coordinates of the electronic ground state and excited state. According to the Born – Oppenheimer approximation an electron weighs around 1870 times lighter than a proton or a neutron [7]. Thus, during the absorption of photons represented by the vertical line E_A, electrons can easily move to the excited state while the much heavier nuclei does not have enough time to reposition itself as the absorption act occurs in the order of femtoseconds [8]. As a result, the absorption line E_A hits the upper region of the excited state potential curve instead of the lowest point of the curve which corresponds to a non-vibrating state. The molecule finds itself in a non-equilibrium state which causes the molecule to vibrate [5]. These vibrations are in the order of 10^{12} oscillations per second, which gives the molecule enough time to achieve several thousand vibrations since the lifetime of an electronic excited state is around 10^{-9} s. During this time, the vibration energy of the oscillating molecule is lost to the medium and the molecule quickly relax to its lowest

vibrational level in the excited state [5,8]. The molecule then decays to the electronic ground state a photon is emitted. Similar to the absorption mechanism the emission line E_E does not hit the lowest point of the ground state curve, and the excess excitation energy is converted to vibrational energy [5]. As a result, the wavelength emitted by a material is typically longer than the wavelength it absorbed. This phenomenon, known as Stokes shift is illustrated in Figure 2.5.

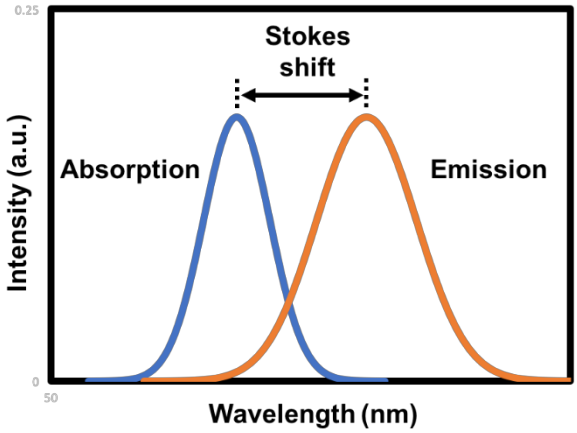

Figure 2.5 An absorption and emission spectrum illustrating Stokes shift.

2.3.2. Luminescence life-time

The luminescence life-time of a phosphor material is defined by the amount of time a phosphor material continues to glow after the excitation source is removed. Thus, a phosphor material can be characterised in two categories namely fluorescence or phosphorescence as shown in Figure 2.6 [9].

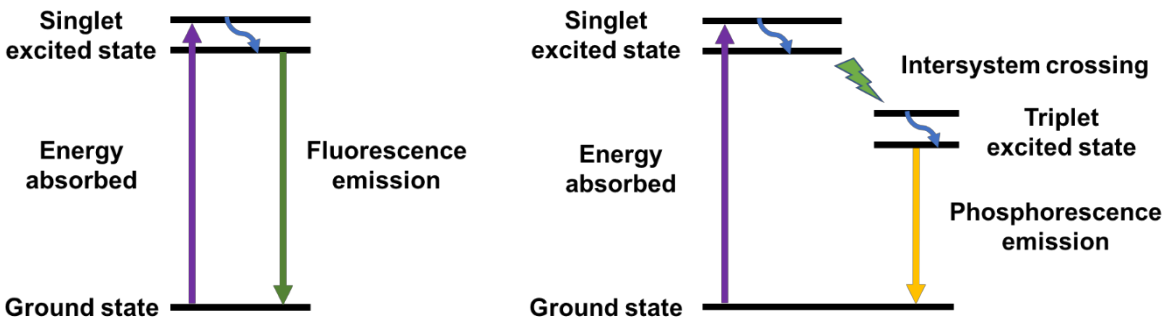

Figure 2.6: Schematic illustrating the fluorescence and phosphorescence mechanism.

In fluorescence materials, the electron from ground state have an opposite spin to the electron in the excited singlet state. The transition from the ground state to the excited state is an allowed transition leading to a rapid return to the ground state for an electron in the excited state. Thus, the emission rates for fluorescence materials are in the order of nano-seconds [9]. In phosphorescence materials, the electron in the excited triplet state has an identical spin orientation to the electron in the ground state. The transition for the excited triplet state to ground state is thus a forbidden transition resulting in a slower emission rate as compared to a fluorescence material. Thus, emission life-times for phosphorescence materials are typically in the order of milli-seconds to seconds [9].

2.3.3. Down-conversion

Down-conversion is a process whereby two or more photons can be created by one parent photon, thus a phosphor material with such a property is able to have a quantum efficiency greater than 100 % [10]. Down-converting phosphor materials have gained interest in recent years for possible applications in solar cells where high energy photons are converted to wavelengths that are better utilised by the cells and improve their overall efficiency [11]. Figure 2.7 shows the various possible mechanisms where NIR down-conversion can be achieved using one or more different activator ions. In single-ion down-conversion, shown in Figure 2.7a an activator is excited to its highest excited state where stepwise relaxation to the ground state can yield two NIR photons [12]. In a multi-ion down-conversion mechanism, illustrated in Figure 2.7b-e, resonant energy transfer between two luminescence centres, which are required to be close proximity to each other. In Figure 2.7b a two-step energy transfer process occurs where the interaction between the two ions results in an emission of two NIR photons [12]. Figure 2.7c shows a down-conversion mechanism involving a single-step energy transfer process [12]. Figure 2.7d illustrates the emission of two NIR photons by the acceptor ions due to the cross-relaxation between the donor and acceptor ions [13]. Lastly, in Figure 2.7e two NIR photons are generated during relaxation of the donor ions, which triggers a simultaneous excitation of the two acceptor ions [12].

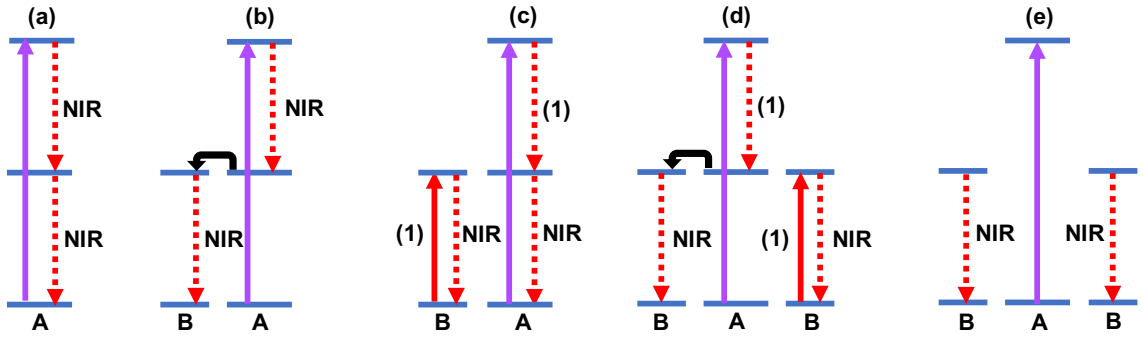

Figure 2.7: Schematic illustration of different down-conversion mechanisms. (a) down-conversion of a high energy photon into two NIR photons by a single ion. (b-d) NIR down-conversion as a result of energy transfer from ion A to ion B. (e) Cooperative down-conversion. Adapted from [12,13].

2.3.4. Up-conversion

Up-conversion is a spectral manipulation process where two or more low energy photons are combined to produce a high energy photon. Similar to down-conversion the process of up-conversion has also gained interest over recent years for improving the efficiency of solar cells.

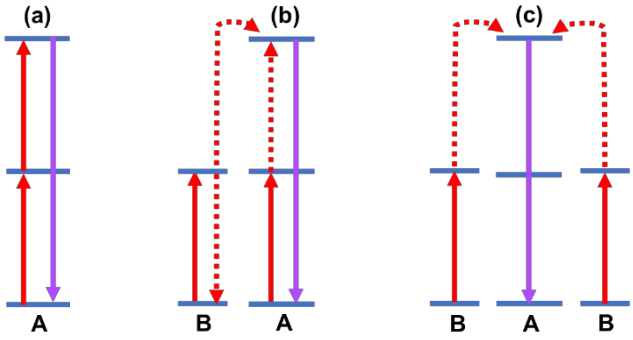

Figure 2.8: Schematic illustrating the different mechanisms for up-conversion. (a) Excited state absorption, (b) energy transfer up-conversion and (c) cooperative up-conversion [12].

The process of up-conversion can occur through either a single or a combination of several mechanisms as shown in Figure 2.8. Figure 2.8a shows a typical excited state absorption where a higher energy photon is produced through stepwise absorption of lower energy photons by a singular ion. The energy transfer up-conversion process shown in Figure 2.8b involves the absorption of two photons by two ions in order to populate their metastable energy level. Rather

than the stepwise absorption process, energy transfer (B → A) between two neighbouring ions occur which produces a high energy photon. Figure 2.8c shows the cooperative up-conversion mechanism where the emission level of the (A) ion is populated by two adjacent ions due to the absence of any intermediate energy levels present in the donor (B) ions.

2.4 Non-radiative emission

Luminescence quenching is the phenomenon where a decrease in the overall luminescence intensity of a phosphor material is observed. This process can be categorised into two main categories: thermal quenching and concentration quenching.

2.4.1. Thermal quenching

Thermal quenching is a process where an electron in the excited state relaxes to the ground state non-radiatively by the addition of thermal energy. An intersection of two energy curves representing the ground and excited state is shown in Figure 2.9. When optical absorption occurs an electron in the ground state A is promoted to the excited state B where it then relaxes to the equilibrium position C. The excited electron may now follow one of two paths, the radiative path (C, D and A) or the non-radiative path (C, E and A). In the non-radiative path an electron from point C is thermally excited with an energy U to the intersection point E after which the electron relaxes back to the ground state. The non-radiative transition rate k_{NR} is given by [14],

$$k_{NR} = F \exp \frac{-\Delta U}{kT} \tag{2.10}$$

where F is the frequency factor typically in the order of 10^{13} s^{-1}, ΔU is the activation energy and kT is the thermal energy.

The quantum efficiency can be determined by,

$$\mathrm{QE} = \left[1 + C \exp \frac{-\Delta U}{kT}\right]^{-1} \tag{2.11}$$

where C is a dimensionless constant.

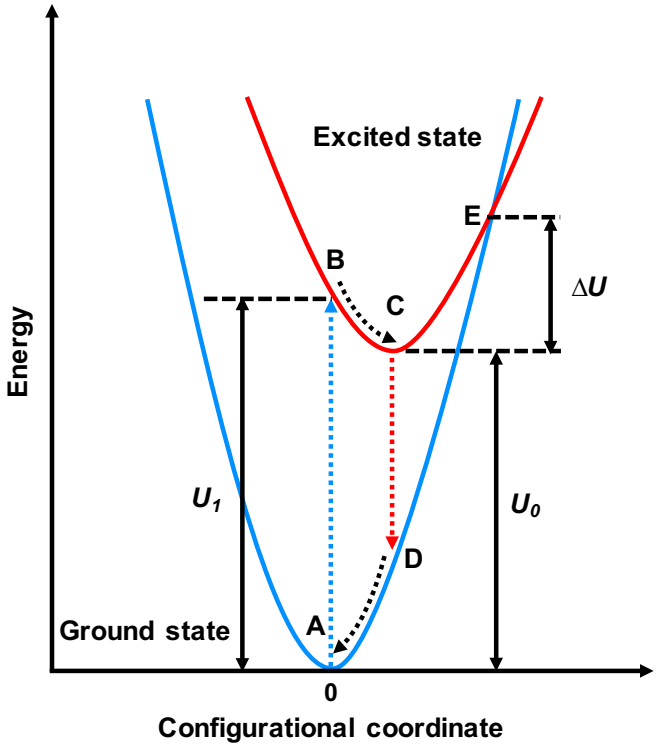

Figure 2.9: Illustration of a configurational coordinate diagram representing the non-radiative transition [15].

2.4.2. Concentration quenching

Concentration quenching is process caused by cross-relaxation between two activator ions [15]. When the concentration of an activator is increased, luminescence intensity of a material generally improves up to a certain threshold where any further increase in the activator concentration leads to a decrease in the intensity due to cross-relaxation between the ions.

An excited ion loses some energy by relaxing to a lower energy state, another ion then acquires the energy and is excited to a higher state [16]. An illustration of cross-relaxation between two Tb^{3+} ions are shown in Figure 2.10. In Tb^{3+} the energy difference between $^5D_3$ and $^5D_4$ excited states is approximately equal the $^7F_6$ ground state and the ^7F_J excited states. At low Tb concentrations, the probability of cross-relaxation is low and it is thus possible to observe emission from both the $^5D_3$ and $^5D_4$ energy states [17]. However, at higher concentrations the

Tb-Tb distances are shorter which promotes the process of cross-relaxation reducing the probability of emission from the $^5D_3$ level and favouring the $^5D_4$ emission [15,17].

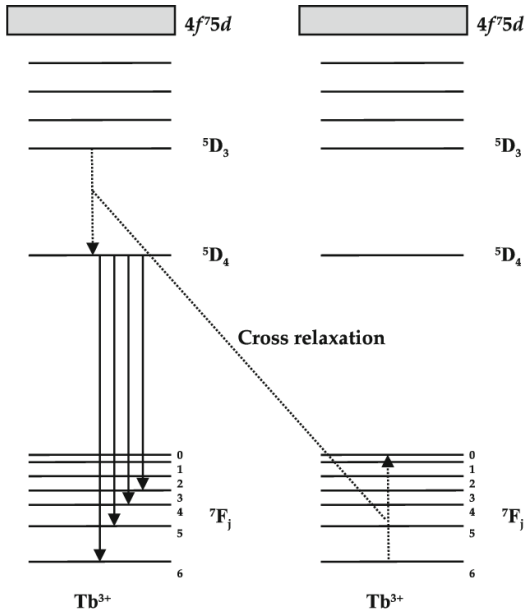

Figure 2.10: Energy level diagram of two neighbouring Tb^{3+} ions and the scheme for cross-relaxation mechanism of the two ions [18].

2.5 Composition of a phosphor

Phosphors are generally constructed from crystalline host lattices doped with activators and in some cases sensitizers. The host lattice serves as vessel for the dopant ions and it is therefore important that it exhibits good thermal, optical and mechanical properties [19]. Activators are structural defects or foreign ions that are placed in the host lattice and forms the luminescent centre of the phosphor material. The kind of luminescent centre chosen depends on the desired emission colour and the valance change and ionic radius of the host lattice cation. To reduce lattice distortion within the host material it is important that the valance charge of the host cation should match the valance charge of the dopant ions. Additionally, using dopants with a similar ionic radius to that of the host cation may further reduce the stresses and strain within the host lattice. In cases where the activator shows weak absorption at certain wavelengths of the excitation source, a second type of dopant known as a sensitizer is added to the host lattice [17]. The sensitizer absorbs the underutilised radiation and transfers the energy to the activator ion improving the overall efficiency of the phosphor material [20]. Traditionally, rare-earth ions have been used as both the activator and sensitizer in applications where specific emission

wavelengths are desired. This is due to their narrow emission and absorption bands as a result of their 4f-4f parity forbidden transitions. However, in applications such as solar spectrum converters, sensitizers are required to absorb at much broader range of emission in order to improve the overall efficiency of the phosphor material. In such a case, non-rare-earth ions with a boarder absorption band is more desired.

2.5.1. Yttrium oxide (host lattice)

Yttrium oxide (Y_2O_3) has proven to be a useful host material in recent years for technological and scientific applications such as light emitting diodes (LEDs) where europium (Eu) doped Y_2O_3 phosphors are used to produce the red emission [21–23]. The host material has good optical and physical properties such as a large band gap at around 5.8 eV, a broad optical transparency between 200 nm – 8000 nm and a relatively high melting point in the region of 2410 °C [21,24–27]. Y_2O_3 is a *c*-type crystal structure which forms part of the I*a*-3 space group. Figure 2.11 shows the cubic crystal structure of Y_2O_3, the Y^{3+} ions are distributed into two non-equivalent Wykoff positions namely the 8b and 24d positions which corresponds to the S_6 and C_2 symmetry respectively. By observing the bonding length between the Y and O atoms, it is clear that the 8b position has a larger volume than the 24d position and therefore dopants with an ionic radius larger than that of Y^{3+} ion (r = 0.090 nm) would prefer to occupy the 8b position over the 24d position [28]. The unit cell dimensions for cubic Y_2O_3 are, $a = b = c =$ 1.0604 nm [29,30].

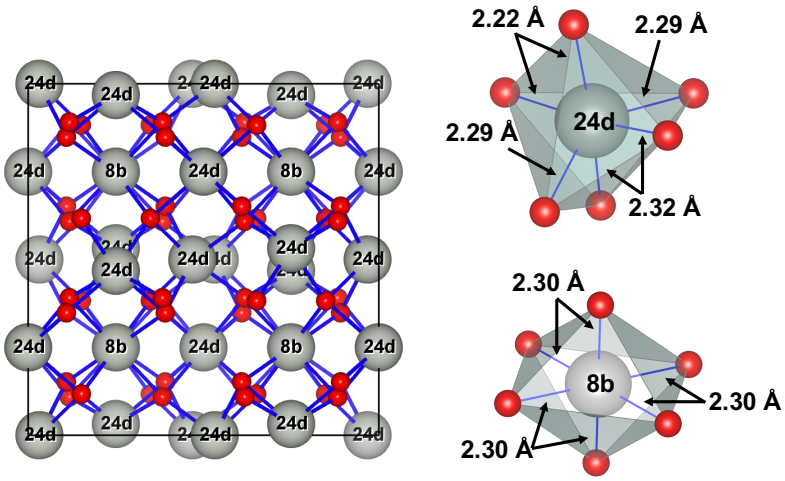

Figure 2.11: The crystal structure of Y_2O_3 (Y ions – grey spheres and O ions – red spheres). Adapted from [31].

2.5.2. Ytterbium (Activator)

Ytterbium is a rare earth element forming part of the lanthanide series. Similar to other lanthanides, ytterbium is commonly found as in the +3 state. Yb^{3+} has an electron configuration of [Xe] $4f^{13}$ which lacks a single electron when compared to a filled 4f shell. This means that Yb^{3+} has only two energy states: a $^2F_{7/2}$ ground state and a $^2F_{5/2}$ excited state where the two states are separated by approximately 10 000 cm^{-1} [32,33]. Unlike the other RE^{3+} ions with a narrow absorption band, Yb^{3+} displays a rather broad near-infrared absorption band between 870 nm to 1050 nm [34]. This suggests that the electrons in the 4f shell of the Yb^{3+} does not experience much shielding from the outer 5s5p shells compared to the other RE^{3+} [35]. When Yb^{3+} ions are placed in a host lattice the electrostatic interaction between the crystal field of the host lattice and the ion causes a phenomenon known as Stark splitting. This process splits the ground state of Yb^{3+} into 4 sub levels (Z_1, Z_2, Z_3, Z_4) and the excited state is split into 3 sub levels (A_1, A_2, A_3) shown in Figure 2.12 [36].

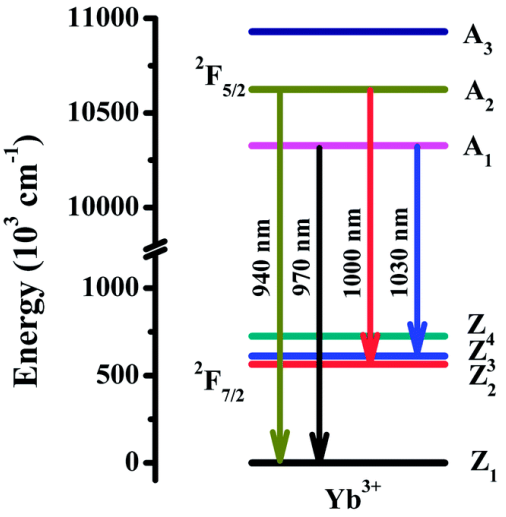

Figure 2.12: Energy level diagram of Yb^{3+} caused by the crystal field Stark splitting [36].

2.5.3. Bismuth (sensitizer)

Bismuth is a post-transition metal which are elements situated between the transition metals and metalloids. These metals have relatively low melting points and low mechanical strength compared to the transition metals and are brittle or soft. Bismuth is situated in group 15 on the periodic table with an electron configuration of [Xe] $4f^{13}5d^{10}6s^26p^3$ yielding 5 valance

electrons. This gives bismuth a large number of valance state ranging from -3 to +5, with the most stable state being the Bi^{3+} state, and depending on its valance state bismuth may exhibit different luminescence properties. In the case of Bi^{+} a broad emission in the near infrared region is observed [37]. Bi^{2+} shows strong red-orange emission while Bi^{3+} emits strongly in the UV to green region [38–40]. In addition to the broad emission Bi^{3+} also displays a broad absorption band in the UV region. These superb luminescence properties of bismuth can therefore be attributed to the absence of shielding experienced by the outer electron orbitals.

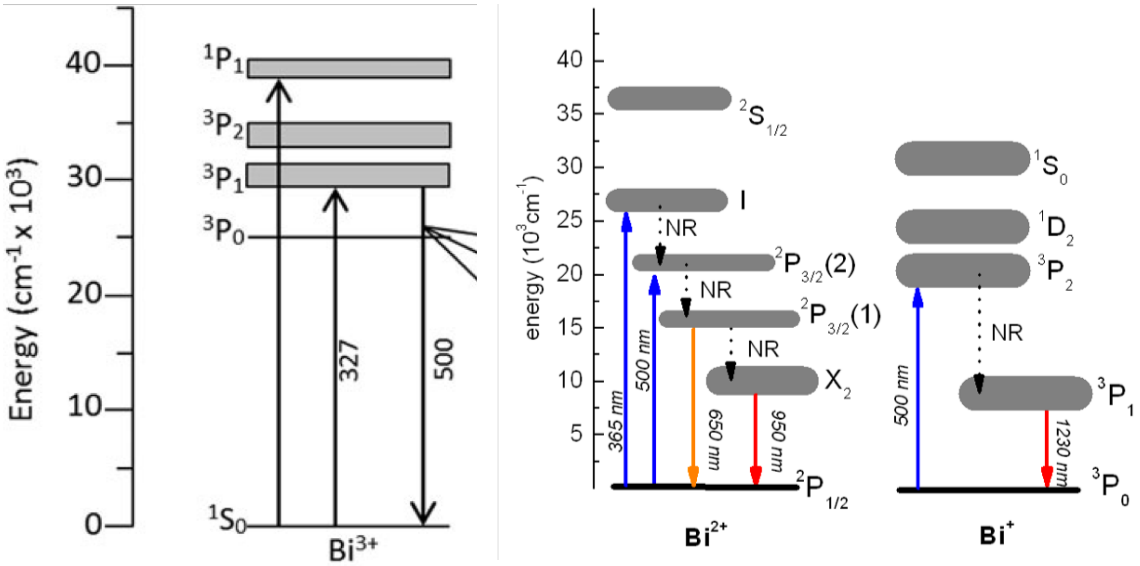

Figure 2.13: Simplified energy level diagram for Bi^{3+}, Bi^{2+} and Bi^{+} [41,42].

2.6 References

[1] B. Valeur, M. N. Berberan-Santos, "Molecular Fluorescence: Principles and Applications", *WILEY-VCH Verlag GmbH & Co. KGaA, Weinheim*, (2013)

[2] B. P. Straughan, S. Walker, "Spectroscopy", *Springer, Netherlands*, (1976)

[3] K. N. Shinde, S. J. Dhoble, H. C. Swart, K. Park, "Basic Mechanisms of Photoluminescence", *Springer-Verlag, Berlin Heidelberg*, (2013)

[4] S. Nara, S. Ibuki, "Fundamentals of luminescence", *in Fundamentals of Phosphors* (eds. Yen, W. M., Shionoya, S. & Yamamoto, H.) , Chapt. 1 Sec. 2, *CRC Press, Taylor and Francis Group, New York*, (2007)

[5] M. Sauer, J. Hofkens, J. Enderlein, "Basic Principles of Fluorescence Spectroscopy", *in Handbook of Fluorescence Spectroscopy and Imaging* , Chapt. 1, *WILEY-VCH Verlag GmbH & Co. KGaA, Weinheim*, (2011)

[6] Wikimedia Commons, "Franck-Condon", Available at: https://commons.wikimedia.org/wiki/File:Franck-Condon-Prinzip.svg. (Accessed: 01 November 2017)

[7] F. Bechstedt, "Born – Oppenheimer approximation", *in Many-Body Approach to Electronic Excitations* , Chapt. 1, *Springer-Verlag, Berlin Heidelberg*, (2015)

[8] E. Rabinowitch, Govindjee, "Photosynthesis", *John Wiley & Sons, Inc., New York*, (1969)

[9] J. R. Lakowicz, "Principles of Fluorescence Spectroscopy", *Springer, New York*, (2007)

[10] B. S. Richards, "Enhancing the performance of silicon solar cells via the application of passive luminescence conversion layers", *Sol. Energy Mater. Sol. Cells*, **90,** 2329–2337 (2006)

[11] B. M. van der Ende, L. Aarts, A. Meijerink, "Lanthanide ions as spectral converters for solar cells", *Phys. Chem. Chem. Phys.*, **11,** 11081–11095 (2009)

[12] X. Huang, S. Han, W. Huang, X. Liu, "Enhancing solar cell efficiency: the search for luminescent materials as spectral converters", *Chem. Soc. Rev.*, **42,** 173–201 (2013)

[13] M. Y. A. Yagoub, "Effect of broadband excitation ions in the luminescence of Ln^{3+} doped SrF_2 nanophosphor for solar cell application", PhD dissertation, *University of the Free State*, *South Africa*, (2015)

[14] E. Nakazawa, "Fundamentals of luminescence", *in Fundamentals of Phosphors* (eds. Yen, W., Shionoya, S. & Yamamoto, H.) , Chapt. 1 Sec. 7, *CRC Press, Taylor and Francis Group, New York*, (2007)

[15] E. Nakazawa, "Fundamentals of luminescence", *in Fundamentals of Phosphors* (eds. Yen, W. M., Shionoya, S. & Yamamoto, H.) , Chapt. 1 Sec. 1, 1–9 *CRC Press, Taylor and Francis Group, Boca Raton, Florida*, (2007)

[16] K. N. Shinde, S. J. Dhoble, H. C. Swart, K. Park, "Phosphate Phosphors for Solid-State Lighting", *Springer-Verlag Berlin Heidelberg*, (2012)

[17] C. R. Ronda, "Emission and Excitation Mechanisms of Phosphors", *in Luminescence: From Theory to Applications* (ed. Ronda, C. R.) , Chapt. 1, *WILEY-VCH Verlag GmbH & Co. KGaA, Weinheim*, (2008)

[18] M. Back, A. Massari, M. Boffelli, F. Gonella, P. Riello, D. Cristofori, C. Studi, E. Fermi, "Optical investigation of Tb^{3+}-doped Y_2O_3 nanocrystals prepared by Pechini-type sol-gel process", *J Nanopart. Res.*, **14,** 792–801 (2012)

[19] Y. Zhang, J. Hao, "Metal-ion doped luminescent thin films for optoelectronic applications", *J. Mater. Chem. C*, **1,** 5607–5618 (2013)

[20] G. Sharma, P. Sehgal, A. K. Narula, "Luminescent Lanthanide Sensors and Lanthanide Doped Upconversion Nanoparticles: Current Status and Future Expectations", *in Reviews in Fluorescence 2015* (ed. Geddes, C. D.) , Chapt. 11, *Springer International Publishing, Switzerland*, (2015)

[21] L. Robindro Singh, R. S. Ningthoujam, V. Sudarsan, I. Srivastava, S. Dorendrajit Singh, G. K. Dey, S. K. Kulshreshtha, "Luminescence study on Eu^{3+} doped Y_2O_3 nanoparticles: particle size, concentration and core–shell formation effects", *Nanotechnology*, **19,** 55201 (2008)

[22] L. S. Chi, R. S. Liu, B. J. Lee, "Synthesis of Y_2O_3:Eu,Bi Red Phosphors by Homogeneous Coprecipitation and Their Photoluminescence Behaviors", *J. Electrochem. Soc.*, **152,** 93 (2005)

[23] V. H. Mudavakkat, V. V. Atuchin, V. N. Kruchinin, A. Kayani, C. V. Ramana, "Structure, morphology and optical properties of nanocrystalline yttrium oxide (Y_2O_3) thin films", *Opt. Mater. Amst.*, **34,** 893–900 (2012)

[24] H. Guo, W. Zhang, L. Lou, A. Brioude, J. Mugnier, "Structure and optical properties of rare earth doped Y_2O_3 waveguide films derived by sol–gel process", *Thin Solid Films*, **458,** 274–280 (2004)

[25] D. F. Bezuidenhout, R. Pretorius, "The optical properties of evaporated Y_2O_3 films", *Thin Solid Films*, **139,** 121–132 (1986)

[26] S. Som, M. Chowdhury, S. K. Sharma, "Band gap and trapping parameters of color tunable Yb^{3+}/Er^{3+} codoped Y_2O_3 upconversion phosphor synthesized by combustion route", *J. Mater. Sci.*, **49,** 858–867 (2014)

[27] Yttrium(III) Oxide, "ThermoFisher Scientific, MSDS, CAS# 1314-36-9", Available at: https://www.fishersci.com/shop/msdsproxy?productName=AC194610500&productDescription=YTTRIUM%28III%29-OXIDE+99.9+50GR&catNo=AC194610500&vendorId=VN00032119&storeId=10652. (Accessed: 23 October 2017)

[28] R. D. Shannon, "Revised effective ionic radii and systematic studies of interatomic distances in halides and chalcogenides", *Acta Crystallogr. Sect. A*, **32,** 751–767 (1976).

[29] R. J. Gaboriaud, F. Pailloux, P. Gueriun, F. Paumier, "Yttrium oxide thin films, Y_2O_3, grown by ion beam sputtering on Si", *J. Phys. D Appl. Phys.*, **33,** 2884–2889 (2000).

[30] A. Huignard, A. Aron, P. Aschehoug, B. Viana, J. Théry, A. Laurent, J. Perrière, "Growth by laser ablation of Y_2O_3 and Tm:Y_2O_3 thin films for optical appications", *J. Mater. Chem.*, **10,** 549–554 (2000)

[31] R. M. Jafer, "Luminescence properties of Y_2O_3:Bi^{3+} as powder and thin film phosphor for solar cell application", MSc dissertation, *University of the Free State*, *South Africa*, (2015)

[32] L. D. Deloach, S. A. Payne, L. L. Chase, L. K. Smith, W. L. Kway, W. F. Krupke, "Evaluation of Absorption and Emission Properties of Yb^{3+} Doped Crystals for Laser Applications", *IEEE J. Quantum Electron*, **29,** 1179–1191 (1993)

[33] L. Zhang, H. Hu, "Evaluation of spectroscopic properties of Yb^{3+} in tetraphosphate glass", *J. Non Cryst. Solids*, **292,** 108–114 (2001)

[34] L. A. Diaz-Torres, E. De la Rosa, P. Salas, H. Desirena, "Enhanced cooperative absorption and upconversion in Yb^{3+} doped YAG nanophosphors", *Opt. Mater.*, **27,** 1305–1310 (2005)

[35] O. Meza, L. A. Diaz-Torres, P. Salas, E. De la Rosa, C. Angeles-Chavez, D. Solis, "Cooperative Pair Driven Quenching of Yb^{3+} Emission in Nanocrystalline ZrO_2:Yb^{3+}", *J. Nano Res.*, **5,** 121–134 (2009)

[36] Z. Fang, R. Cao, F. Zhang, Z. Ma, G. Dong, J. Qiu, "Efficient spectral conversion from visible to near-infrared in transparent glass ceramics containing Ce^{3+} –Yb^{3+} codoped $Y_3Al_5O_{12}$ nanocrystals", *J. Mater. Chem. C*, **2,** 2204–2211 (2014)

[37] A. R. Muhammad, P. Harshavardhan Reddy, H. Haris, S. W. Harun, A. Halder, Shyamal Das, Anirban Dhar, Mukul Chandra Paul, "Near Infrared Amplified Spontaneous Emission of Bismuth Doped Fiber", *J. Optoelectron. Biomed. Mater.*, **8,** 131–135 (2016)

[38] L. Seijo, Z. Barandiara, "Blue absorption and red emission of Bi^{2+} in solids: strongly spin–orbit coupled 6p levels in low symmetry fields", *Phys. Chem. Chem. Phys.*, **2,** 17305–17314 (2014)

[39] X. Y. Huang, Q. Y. Zhang, "Near-infrared quantum cutting via cooperative energy transfer in Gd_2O_3:Bi^{3+},Yb^{3+} phosphors", *Chin. Phys. B*, **19,** 3–6 (2010)

[40] U. Rambabu, S. Do Han, "Broad band down conversion from ultra violet light to near infrared emission in YVO_4:Bi^{3+},Yb^{3+} as spectral conversion phosphor for c-Si solar cells", *Ceram. Int.*, **39,** 1603–1612 (2013)

[41] A. Winterstein, S. Manning, H. Ebendorff-Heidepriem, L. Wondraczek, "Luminescence from bismuth-germanate glasses and its manipulation through oxidants", *Opt. Mater. Express*, **2,** 1320–1328 (2012)

[42] A. M. Ramírez, M. G. Hernández, J. Y. Ávila, A. G. Murillo, F. C. Romo, E. de la Rosa, V. G. Febles, J. R. Miranda, "Eu^{3+},Bi^{3+} codoped Lu_2O_3 nanopowders: Synthesis and luminescent properties", *J. Mater. Res.*, **28,** 1365–1371 (2013)

Chapter 3: Phosphor powder and thin film synthesis

In this chapter, the co-precipitation method used to synthesis the phosphor powder, spin coating and pulsed laser deposition technique used to synthesis the thin films are discussed. Research techniques used to characterise the structural, chemical and luminescence properties of the synthesised material are also discussed. X-ray diffraction (XRD) was used to obtain crystal structure and structural parameters. Photoluminescence (PL) spectroscopy provided optical information about the sample material. The chemical composition and oxidation states of elements present in the phosphor material are obtained using the X-ray photoelectron spectroscopy (XPS) technique. Finally, to study the morphology and chemical composition of the material a field emission scanning electron microscope (FE-SEM) couple energy dispersive X-ray spectroscopy (EDS) system was used.

3.1 Preparation techniques

The physical and chemical properties of a material is dependent on its synthesis environment and therefore it is important to select an appropriate synthesis technique for the application of the material. The two most widely used methods for the synthesis of phosphor materials are the solid state reaction and wet reaction method [1]. In solid state reactions, the phosphor product is produced by mixing the starting material together until a homogenous mixture is achieved before sintering at high temperatures [2]. For wet reactions such as sol-gel and co-precipitation, the starting materials are dissolved in some solvent to achieve homogeneity and by addition of a second solvent the desired product can be forced to precipitate.

3.1.1. Co-precipitation

The co-precipitation synthesis is a technique that is used to simultaneously remove dissolved sample material from an aqueous solution [3]. An example of the co-precipitation reaction mechanism used in this study is shown below,

$$(1\text{-}x)Y_2O_{3\,(s)} + xBi_2O_{3\,(s)} + 6HNO_{3\,(aq)} \rightarrow 2(Y_{1\text{-}x}Bi_x)(NO_3)_{3\,(aq)} + 3H_2O_{\,(l)}$$

$$2(Y_{1\text{-}x}Bi_x)(NO_3)_{3\,(aq)} + 3H_2O_{\,(l)} + 6NH_4OH_{\,(aq)} \rightarrow 2Y_{1\text{-}x}Bi_x(OH)_{3\,(s)} + 6NH_4NO_{3\,(s)} + 3H_2O_{\,(l)}$$

$$2Y_{1\text{-}x}Bi_x(OH)_{3\,(s)} + \text{Heat} \rightarrow (Y_{\text{-}x}Bi_x)_2O_{3\,(s)} + 3H_2O_{\,(g)} \uparrow$$

In this study stoichiometric amounts of yttrium oxide (Y_2O_3), bismuth oxide (Bi_2O_3) and ytterbium oxide (Yb_2O_3) were placed in 20 mL of distilled water in order to keep the starting material in suspension. To increase the rate of dissolution, the oxide slurry was heat to 60 ºC before the addition of acid. Nitric acid (70 %) was added to the oxide slurry dropwise until all the starting material completely dissolved. Once the nitrate solution was cooled to room temperature, ammonia hydroxide (NH_4OH) was added to the solution. The volume of NH_4OH added to the nitrate solution was determined by the pH value that was desired. To ensure that all the starting material precipitated simultaneously the entire volume NH_4OH solution was added to the nitrate solution in a single instance. The once clear solution has then formed a white precipitate which indicated that the starting material has been forced out of the solution. The slurry was allowed to stir for 2 h to ensure that all the reagent has reacted. The precipitate was separated from the liquid using a centrifuge. In order to remove any non-reacted reagents, the precipitate was washed using ethanol (99.9 %) and then with distilled water. The washing of the precipitate was repeated a total of 3 times, after each wash the precipitate was separated from the solvent using a centrifuge. The washed precipitate was then transferred to a drying oven, where it dried at 100 ºC for 12 h. The dried hydrate product was grounded and placed in an annealing oven where the hydrate was heated in air at 450 ºC for 1 h then at 1000 ºC for 2 h. This high temperature annealing process oxidised the hydrate by converting the hydrate back into an oxide forming the final product.

3.1.2. Sol-gel process

The sol-gel process is a synthesis technique used to prepare ultra-fine metal or ceramic oxide bulk powders or thin films [4]. An example showing the sol-gel preparation of an yttrium citrate gel is shown below,

$$Y_2O_{3\,(s)} + 6HNO_{3\,(aq)} \rightarrow 2Y(NO_3)_{3\,(aq)} + 3H_2O_{\,(l)}$$

$$2Y(NO_3)_{3\,(aq)} + 3H_2O_{\,(l)} + 6C_6H_8O_{7\,(s)} + \text{Heat} \rightarrow 2Y(C_6H_7O_7)_{\,(l)} + 3H_2O_{\,(l)} + 3HNO_{3\,(g)} \uparrow$$

In this study a co-precipitation prepared $Y_2O_3:Bi^{3+},Yb^{3+}$ phosphor material was used as the starting material to prepare the citrate gel. The phosphor material was placed in 20 mL of distilled water heated to 60 ºC. Concentrated HNO_3 (70 %) was added to the oxide slurry dropwise until all the oxide has dissolved. The phosphor powder was kept in suspension by placing the oxide in heated distilled water, which aided the rate of dissolution when the acid was added. Once dissolved stoichiometric amounts of citric acid was added to the nitrate solution. The citrate solution was heated and stirred at 80 ºC until a thick transparent gel was produced. Citric acid was used as a binding agent, which helps in keeping the Y, Bi and Yb complex ions evenly distributed within the gel. The prepared gel was then diluted in ethanol to be used as the solution for spin coating, discussed in the next section.

3.2 Deposition techniques

3.2.1. Spin coating

Spin coating is a commonly used technique for producing uniform thin films. This technique can be seen in industry for production on optical mirrors, anti-reflective coating, solar cells and integrated circuits. The process of spin coating can be broken down into 4 stages namely, deposition, spin-up, spin-off and evaporation, shown in Figure 3.1 [5].

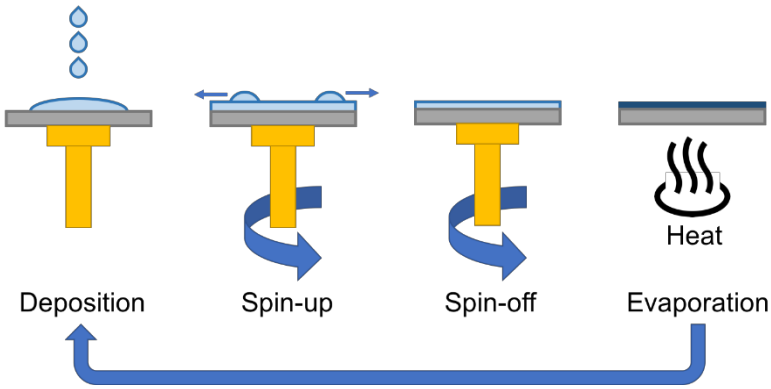

Figure 3.1: Illustration of the stages involved in the spin coating process.

The first stage involves depositing of the thin film solution on to a substrate. The quantity of solution placed on the substrate depends mainly on the area of the substrate. Thus, the general accepted volume of solution is a volume that should cover the entire surface of the substrate as any excess solution would be ejected during the next stage.

For the second stage the substrate is accelerated at a constant rate up to the requested rotation speed. This acceleration forces the solution sideways towards the edges of the substrate flattening any irregularities and ensures the solution is uniformly distributed on the substrate. In the process, the excess solution is expelled from the substrate. The thickness of the solution is dependent on a number of parameters such as the viscosity and surface tension of the solution, the type of substrate used and on the rate and speed of rotation [6].

In the third stage the substrate is rotating at a constant speed. During this process, the solution begins thinning due to the evaporation of the volatile solvents which can be seen by the changes in the inference colours on the substrate [5,7].

The formation of the thin film is achieved by the final stage which involves the evaporation of all the solvents and stabilisers used in producing the thin film solution. This process, depending on the volatility of the solvent and stabiliser, may require the sample to be heated. Depending on the desired thickness of the thin film the above-mentioned stage may need to be repeated on the dried substrate.

In this research the prepared Y_2O_3:$Bi_{2.0\ mol\%}$,$Yb_{10.0\ mol\%}$ powder samples were converted into solution form using the sol-gel method. The viscosity of the gel solution was controlled by addition of ethanol (99.9 %) which in turn changes the amount of sample present in a given volume of solution (molarity). Thus, by adding more ethanol the viscosity and molarity of the solution is lowered. The films were prepared by adding 100 μL of the prepared sample solution onto a 2 cm x 2 cm silicon (100) substrate. The substrate was spun at 5000 rpm for 30 s with a ramping rate of 1000 rpm/sec. The substrate was then moved to an oven where it was dried at 300 ^{o}C for 1 h. This process was repeated several times depending on the desired thickness of the film. Once the desired number of coats was achieved the substrate was annealed at 1000 ^{o}C for 2 h to produce the final thin film.

3.2.2. Pulsed laser deposition

Pulsed laser deposition (PLD) is a type of physical vapour deposition that is readily used in the production of thin films [8]. Similar to the other forms of physical vapour deposition techniques the PLD process needs to be conducted in a vacuum chamber in order to prevent contamination of both the target and substrate. In Figure 3.2 a pulsed laser generated by a Nd:YAG or any other appropriate laser source is directed and focused onto the surface of the target material. If the absorbed laser pulse has sufficient energy, the target material will be ejected from the target in the form of a plasma plume [9]. To ensure that the entire target material is utilised it is placed on a carousel that is able to both rotate and oscillate the target. The amount of energy required to generate the plume is dependent on the duration of the laser pulse and also on the wavelength of the laser, as different target materials have different absorption wavelengths [9,10]. Once the plume reaches the substrate a thin film consisting of the evaporated target material is formed [11]. To control the rate of growth of the thin film, the background gas pressure within the vacuum chamber is adjusted by addition of gas such as oxygen, argon or nitrogen [12,13]. The introduction of gas atoms serves to decrease the kinetic energy of the ejected particles, lowering the number of particles reaching the substrate [13]. In some cases, background gas is used for a reaction where the evaporated target material reacts with the ambient gas before reaching the substrate and forming a thin film with a different composition to that of the target. If changes in the thin film morphology is required, heat is usually applied to the substrate during the deposition process. Heating the substrate provides the incident particles with sufficient mobility for the thin films to grow to its preferred crystal orientation [9,14].

In this study, a Y_2O_3 co-doped Bi^{3+} and Yb^{3+} sample was compressed into a pellet to be used as a target for laser ablation. A silicon (100) substrate was mounted on a substrate holder which was also used as the heater. Once the desired vacuum was reached, background gas was introduced into the deposition chamber, the substrate was heated to a specified temperature and the laser power was maximised. The target was ablated for 30 s to remove any contaminants that might have accumulated on the surface of the target. After cleaning, the target was ablated for some time in order to obtain the required thin film.

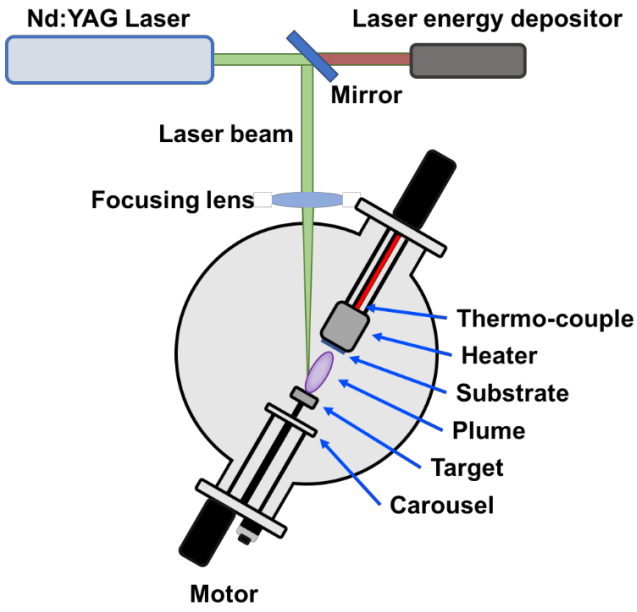

Figure 3.2: Schematic illustration of the pulsed laser deposition setup.

3.3 Characterisation techniques

3.3.1. X-ray diffraction

XRD is a characterisation technique used to obtain the structural properties such as: the crystal structure and phases present within powder or crystalline materials. The XRD system consists of three main components, the X-ray generator, the sample stage and the X-ray detector shown in Figure 3.3.

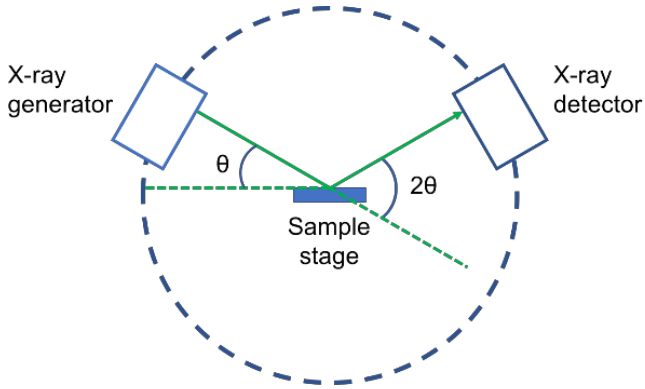

Figure 3.3: Illustration of the XRD setup. Adapted from [15].

The X-ray used in the XRD are generated in a cathode ray tube shown in Figure 3.4. Current is applied though a tungsten filament causing the filament to liberate electrons. A potential difference is applied between the filament and metal target, which accelerates the free electrons towards the target. The metal targets are generally made from copper, chromium, molybdenum or iron. When an electron strikes the metal target two types of X-rays can be generated, characteristic X-rays or Bremsstrahlung radiation as shown in Figure 3.5 [16].

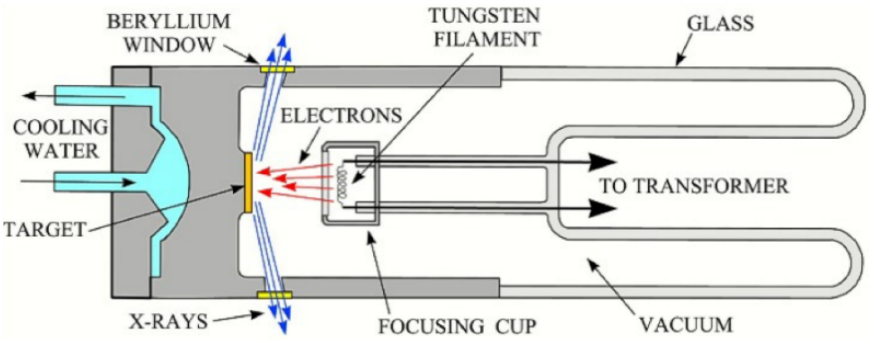

Figure 3.4: Schematic cross section of an X-ray tube [17].

To generate characteristic X-rays the incident electron first strikes and ejects a core shell electron leaving a vacancy, which is quickly filled by an electron in the outer cell. During the transition energy in the form of X-rays, equal to the difference between the higher and lower state is released. Due to the quantised energy states the X-rays produced have discrete energies therefore the X-ray wavelength produced is unique and dependent on the target metal used in the X-ray tube. A Bremsstrahlung X-ray is produced when an incident electron travelling through a material decelerates or is completely stopped when it encounters an atom. When a high-speed incident electron proceeds towards an atom it interacts with the negative forces from the electrons and positive forces from the nucleus of the target metal. This interaction slows down the incident electron decreasing its kinetic energy, which is emitted as an X-ray [16]. The amount of kinetic energy that is converted to a Bremsstrahlung X-ray is dependent on how close the incident electron approaches the nucleus. The closer the electron approaches the nucleus, the stronger the electrostatic interaction between the nucleus, the greater the loss in its kinetic energy, which results in a higher energy Bremsstrahlung X-ray [16,18].

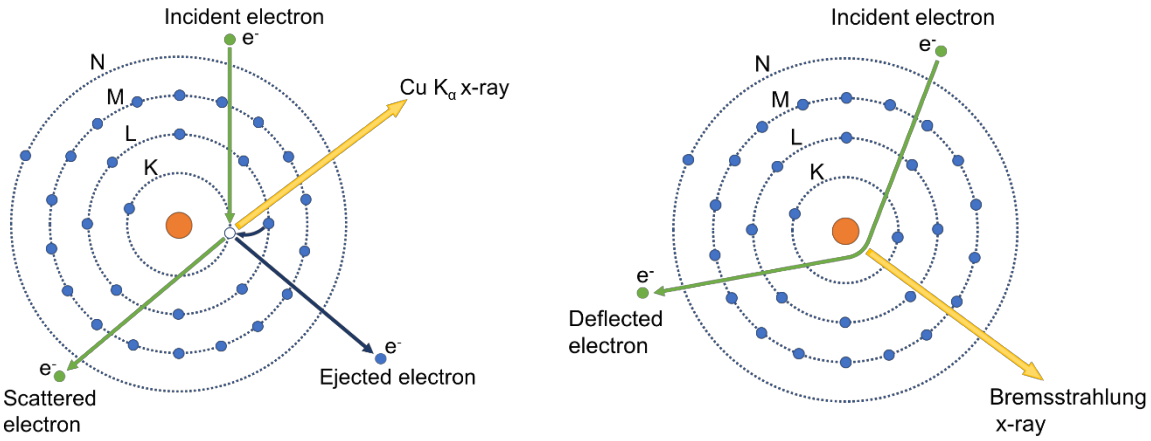

Figure 3.5: Illustration on the generation of characteristic and Bremsstrahlung X-rays.

For X-ray diffraction characterisation, it is required that the X-rays be as monochromatic as possible. The X-rays generated by the X-ray source are, however, not monochromatic as it contains the continuous Bremsstrahlung radiation and also the K_α and K_β emission lines shown in Figure 3.6. To obtain K_α X-rays a filter made from a material with an atomic number less than the metal target is used, for a copper target a nickel filter will absorb the Bremsstrahlung radiation along with the K_β emission line.

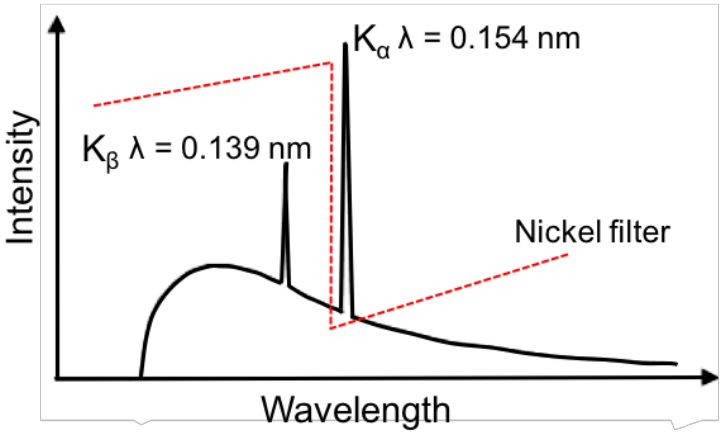

Figure 3.6: The Bremsstrahlung and characteristic X-ray emission of copper (Cu) [19].

When a crystalline or powder material is radiated with monochromatic X-ray, constructive interference is observed at certain incident angles shown in Figure 3.7. The occurrence is known as Bragg's Law which was first derived by William L. Bragg along with his son William H. Bragg in 1913 [20].

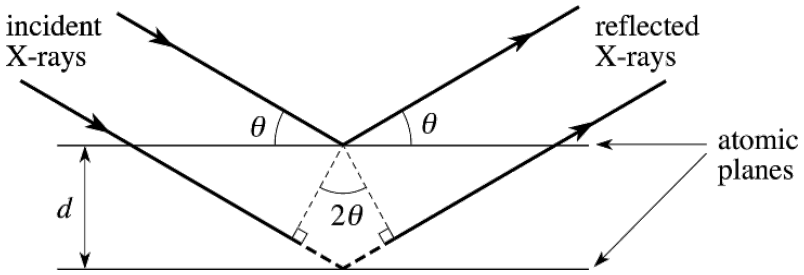

Figure 3.7: Schematic diagram showing the scattering of X-rays by a well-arranged crystal lattice [21].

The Bragg expression is given by:

$$n\lambda = 2d \sin\theta \tag{3.1}$$

where n is an integer, λ is the monochromatic X-ray wavelength projected onto the sample, d is the inter-planar spacing and θ is the Bragg angle. Using the inter-planar spacing d and the Miller index (h k l) for the reflection, the lattice parameter a for a cubic structure can be determined using the following expression,

$$a = d_{hkl}\sqrt{h^2 + k^2 + l^2} \tag{3.2}$$

The X-rays reflected from the material travels toward a detector where the intensity of the X-rays along with its 2θ scattering angle are measured.

The XRD results obtained in this study were measured using a Bruker D8 Advanced diffractometer. The system was equipped with a copper X-ray tube (λ = 0.154 nm) which operated using a filament current of 40 mA and an accelerating voltage of 40 kV. Additionally, a Nickel filter was used to achieve the monochromatic X-ray and to absorb the K_β Cu and Bremsstrahlung radiation.

3.3.2. Photoluminescence spectroscopy

PL spectroscopy is a technique used to characterise the luminescence property of a phosphor material by observing the spontaneous emission of light when excited with an optical source.

An emission spectrum is obtained by exciting a material with a constant wavelength while varying the emission wavelength. While an excitation spectrum is achieved by keeping the emission wavelength fixed and varying the excitation wavelength. A basic schematic showing the main components of a spectrometer is given in Figure 3.8.

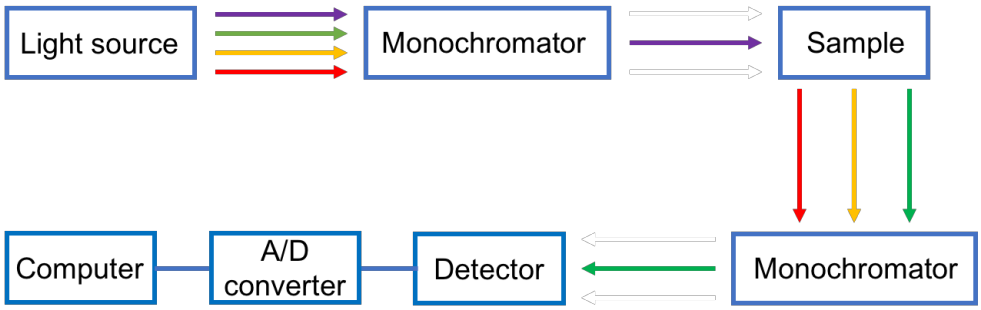

Figure 3.8: Schematic illustration containing the main components of a spectrometer.

Photons generated by the light source are directed towards a monochromator, which has been set to transmit a specific excitation wavelength toward a sample material. The light emitted by the sample is directed towards a second monochromator where it disperses the light into various wavelength components before its analysed by the detector. Because the detectors are in a fixed position, the photomultiplier tube (PMT) or solid-state semiconductor detector can only analyse a section of the spectrum at a time. In order for the detector to analyse the entire emission spectra, the diffraction grating is able to rotate clockwise or anti-clockwise. This changes the reflection angle of the spectral lines and thus changes which section of the spectrum will incident on the detector [22].

Light enters the PMT and incidents on a photocathode, emitting electrons due to the photoelectric effect as shown in Figure 3.9. A high potential is placed between the photocathode and the anode, which cause electrons to accelerate towards the anode. Between the cathode and anode are dynodes; when struck by an electron they will emit more electrons thus the number of electrons is amplified before reaching the anode. Therefore, the flux of electrons collected by the anode can be translated to a current, where a higher current will relate to a high flux of electrons [23]. This makes the PMT much more sensitive than other detectors, but also comes with a disadvantage; for instance if the intensity of light is too bright it may damage the photomultiplier which is expensive to replace.

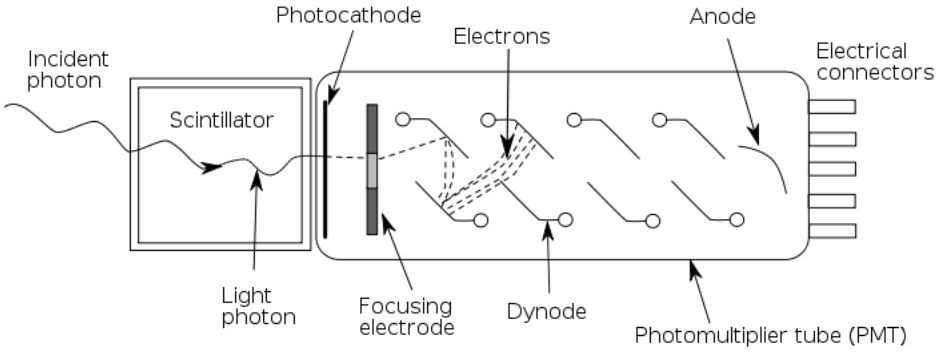

Figure 3.9: Internal construction of a photomultiplier tube [24].

In addition to a PMT detector, a solid-state detector made from a semiconductor material can be used to analyse the radiation emitted by the sample. When radiation strikes the semiconductor free-carriers namely electrons and holes are produced. The production of the free-carriers generates an electrical signal which can be measured [25]. The strength of the electrical signal is dependent on the energy of the radiation incident on the detector: the higher the energy, the more free-carriers are produced resulting in a stronger electrical signal and visa-versa. In order to achieve the fast response and excellent signal-to-noise ratio that solid-state detectors are known for, cooling is required especially for detectors used to analyse long wavelengths such as infrared radiation [25]. Cooling the detector will help lower the background noise as it prevents thermal radiation from generating free-carriers.

The PL results for this study were collected using three systems: a Cary Eclipse fluorescence spectrometer, a Edinburgh FLS980 fluorescence spectrometer and a laser PL system. The Cary Eclipse fluorescence spectrometer is equipped with two single monochromators, a PMT detector and a xenon (Xe) lamp, which is used as the excitation source due to its wide emission spectrum between 200 nm to 1100 nm (see Figure 3.8). The Cary Eclipse fluorescence spectrometer was utilised mainly to measure the visible emission and excitation spectrums of the sample material.

The laser PL system shown in Figure 3.10, is equipped with a He-Cd laser, a PMT detector, an indium gallium arsenide (InGaAs) solid-state IR detector which are attached to a Horiba iHR320 monochromator and two filters. The first filter placed after the laser helps to block the 442 nm emission from the He-Cd and only allows the 325 nm to pass through. The second filter positioned before the spectrometer blocks any reflected 325 nm radiation from entering

the spectrometer. The system is also equipped with an optical chopper, the chopper frequency controller and Lock-in amplifier, which operate in tandem to improve the signal-to-noise ratio of the spectrometer. The optical chopper is constructed from a disk that contain slits that are equally spaced. As the chopper rotates, the slits allow the light beam either through the slits or it can be completely blocked, where the speed at which the chopper rotates is controlled by a frequency controller. Aside from attenuating the light beam the frequency generated by the frequency controller also serves as a reference for the Lock-in amplifier. When an electrical signal is generated by the detector it is feed to the Lock-in amplifier where the frequency of the signal is compared to the reference frequency [26]. Any frequencies that does not match the reference frequency are rejected by the Lock-in amplifier, while frequencies that match the reference pass though the amplifier and is registered by the computer [26]. In this way, the signal-to-noise ratio of this PL system can be greatly increased. In this study, the laser PL system was used to measure the IR radiation emitted by the material.

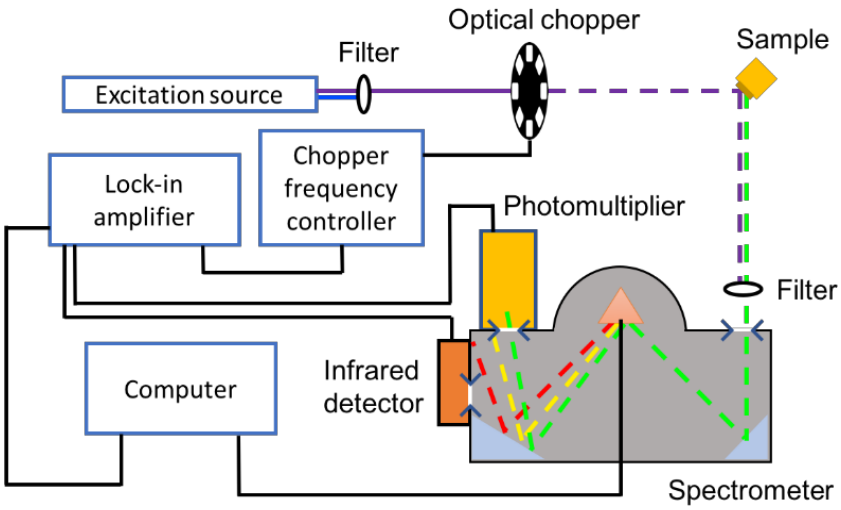

Figure 3.10: Schematic illustration of the laser PL spectrometer equipped with a He-Cd laser. Adapted from [27].

The Edinburgh FLS980 spectrometer works on a similar principle to that of the Cary Eclipse spectrometer, the difference being additional add-ons that can be installed on the FLS980 system and more sophisticated components such as two double monochromators. For this study, a Xe lamp was again used as the excitation source along with a liquid nitrogen cooled IR detector. The system was primarily used to determine the quantum efficiency of the synthesised material, which was achieved by housing the sample in an integrating sphere shown in Figure 3.11.

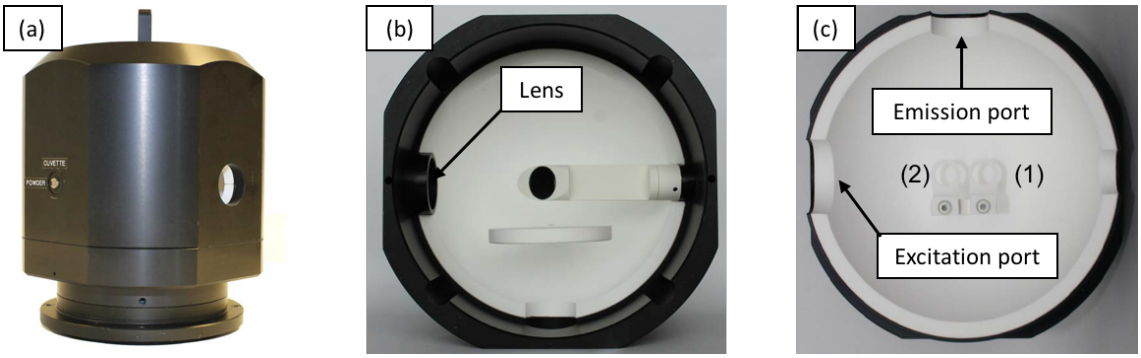

Figure 3.11: (a) External view of the integrating sphere, (b) upper half of the sphere, (c) lower half of the sphere for analysis of solid materials [28].

Monochromatic photons enter the integrating sphere through a focusing lens where they are reflected onto the sample by a mirror. The light emitted by the material strikes the inner walls of the sphere and is scattered towards the emission port where it is measured by the detector. The integrating sphere is made from a type PTFE material that has a > 99 % spectral reflectance between 400 nm to 1500 nm and a > 95 % reflectance between 200 nm to 2500 nm [28].

3.3.3. X-ray photoelectron spectroscopy

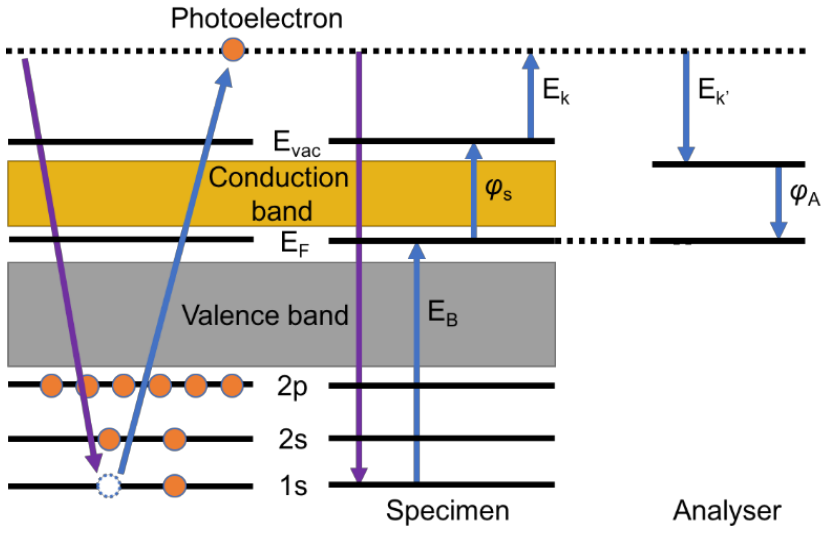

Figure 3.12: Schematic diagram of the XPS process, showing the generation of the photoelectron and the energy levels that are involved in photoemission spectroscopy.

XPS, also referred to as ESCA (electron spectroscopy for chemical analysis), is a research technique used to study the chemical composition on the surface of solid materials [29]. The XPS technique utilises the photoelectric effect where photoelectrons may be ejected from a material when radiated with X-ray photons as shown in Figure 3.12.

The kinetic energy (E_k) of the ejected photoelectron is not a unique property of a material as it is dependent of the energy of the X-ray source (hv) used as shown in equation (3.3) [29].

$$E_k = hv - \varphi_s - E_B \tag{3.3}$$

where E_B is the binding energy of the material and φ_s is the material's work function. The binding energy of a material is the energy difference between its Fermi level and the shell from which the electron was ejected [29]. Therefore, the binding energy is unique for different materials and used as the identifier for determining the elements present in a material. The work function of a material is the energy that is required to completely remove the electron from the material [30]. Due to the E_B and φ_s being dependent on the material being analysed it would be impossible to use equation (3.3) to identify the composition of the material. Fortunately, by grounding both the analyser and sample together it causes their Fermi levels to align, giving rise to the following equation [31],

$$E_k + \varphi_s = E_{k\prime} + \varphi_A \tag{3.4}$$

where $E_{k\prime}$ is the kinetic energy of the photoelectron measured by the analyser and φ_A the work function of the analyser which is a known value. Thus, the kinetic energy of the photoelectron measured by the analyser can be rewritten as,

$$E_{k\prime} = hv - \varphi_A - E_B \tag{3.5}$$

Thus, the binding energy of the ejected photoelectron can be determined in the absence of the sample's work function.

An ultra-high vacuum (UHV) environment is essential for the XPS due to the surface sensitivity of this technique. Depending on the energy and the incident angle of the X-ray relative to the material, the penetration depth of the X-ray can be of the order of several microns [30]. Unfortunately, a photoelectron originating from several microns beneath the surface of the material almost never passes out of the material and move into the analyser due to its stopping power being orders of magnitude higher than that of an X-ray [30]. Only photoelectrons formed near the surface, typically within 2 - 10 monolayers, will reach the analyser with little to no energy lost in its kinetic energy [29,30]. In addition to the UHV environment, a XPS system will also contain an ion gun which is used to sputter the surface of the material using inert ions such as argon (Ar) in order to remove any contaminates that might have settled on the material. A schematic diagram showing a typical XPS setup is shown in Figure 3.13.

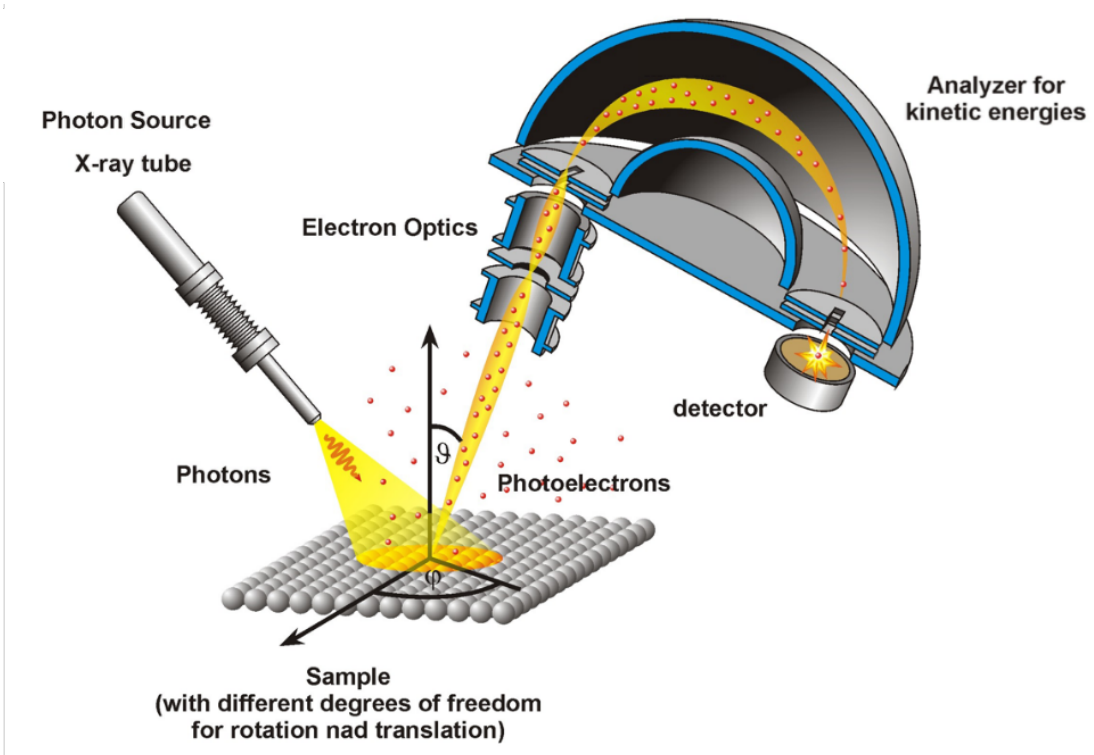

Figure 3.13: Schematic of the XPS setup [32].

The XPS measurements were collected using the PHI 5000 Versaprobe equipped with an aluminium (Al) X-ray source. The monochromatic Al K_α X-ray beam had a diameter of 100 µm and was generated by a 25 W, 15 kV electron beam. The system was also equipped with a low energy electron gun for neutralising or minimising charging effects on the surface of the material, and a low energy Ar^+ ion gun for sputtering.

3.3.4. Field Emission Scanning Electron Microscopy

FE-SEM is a research technique where the interaction between an electron beam and the sample material gives information about the morphology, topography, chemical composition and luminescence properties on the surface of a sample material. The various components that form the electron microscope is shown in Figure 3.14a.

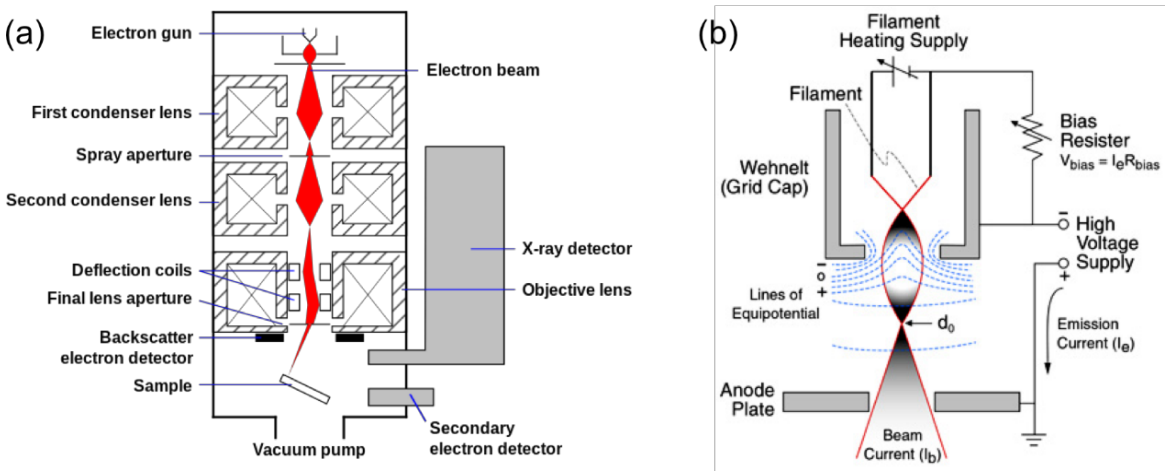

Figure 3.14: (a) Schematic diagram displaying the components present in a scanning electron microscope [33] and (b) basic construction of an electron gun [34].

The electron beam emitted by the electron gun is generated by passing a current through a lanthanum hexaboride (LaB_6) filament, thereby liberating electrons from the tip of the filament which are projected out of the electron gun by high voltage shown in Figure 3.14b.

The electron beam passes through the first condenser lens which serves to control the density of electrons that passes through a spray aperture. A narrow electron beam on the aperture means that more electrons are able to pass through the aperture while a broad beam decreases the number of electrons that pass through the aperture [35]. The beam then enters a second condenser lens, which helps to shape the electrons into a coherent beam before reaching the deflection coils. The deflection coils serve to raster the electron beam, allowing the SEM system to scan the surface of the sample material. The electron beam then passes through the final objective lens which ensures that the beam is well focused on the sample material.

The electrons incident on the sample triggers a variety of emissions such as: secondary electrons, Auger electrons, backscattered electrons, photons and heat. The backscattered and secondary electron detectors work in conjunction to generate a surface image of the sample. The backscattered electrons assist in the contrast of the image while the secondary electrons provide details on the morphology and topography of the sample's surface.

The addition of an X-ray detector gives the SEM system the capability to determine the elemental composition of individual crystals present in the sample. This technique is known as energy dispersive X-ray spectroscopy (EDS). The X-rays emitted by the sample are in the form of characteristic X-rays, the mechanism of how characteristic X-rays are generated is shown in Figure 3.5. By cross referencing the energy of the characteristic X-rays emitted with known standards, the elemental composition of the sample material can be determined.

Aside from using the emitted photons to determine the elemental composition, it is possible to utilise the emitted photon to study the luminescence properties of the sample material. This research technique is known as cathodoluminescence (CL) spectroscopy. Similar to photoluminescence, CL can also be used to examine the defects present within a material due to the introduction of impurities [36]. When the electron beam strikes the sample material, electrons in the ground state (valance band) are excited to an excited stated (conduction band) generating an electron-hole pair (EHs) [36]. The EHs later recombine and energy in the form of a photon is released and measured.

In this study the SEM, EDS and CL results were collected using a Jeol JSM-7800F Field Emission SEM which was also equipped with an Oxford Aztec EDS and a Gatan Mono CL4.

3.3.5. Time-of-flight secondary ion mass spectroscopy

TOF-SIMS is a characterisation technique used to provide detailed elemental and molecular information about the surface of a material [37]. A schematic diagram showing the basic components of the TOF-SIMS is represented in Figure 3.15. Primary ions (Bi, Cs or micro-focused Ga) are generated within an ion gun where they are accelerated by around 20 - 30 kV, producing an ion beam. The ion beam then passes through a pulsing unit, producing an ion beam with a pulse width of 25 ns, the beam is then further bunched. This ensures that the entire

pulsed ion beam incidents the sample within 1 ns. The incident primary ions sputter the surface of the sample liberating secondary ions. The secondary ions are then collected and accelerated by the ion extractor into the time-of-flight mass analyser through an applied potential U_0 (usually +2000 V for negative secondary ions and -2000 V for positive ions). The kinetic energy *KE* of the secondary ion entering the analyser is given by

$$KE = \frac{mv^2}{2} = zU_0 \tag{3.6}$$

where *m* is the mass of the secondary ion, *v* is its velocity and *z* is the charge of the ion. Ions with different mass will travel at different velocities thus the mass of the ion can be obtained by its flight time *t* within the time-of-flight mass analyser. The flight time of an ion can be determined by,

$$t = \frac{L}{v} = L\sqrt{\frac{m}{2zU_0}} \tag{3.7}$$

where *L* represents the effective length of the mass analyser (approximately 2 m). Equation 3.7 can now be rewritten in terms of a mass-to-charge *m/z* ratio given by [38],

$$\frac{m}{z} = \frac{2U_0t^2}{L^2} \tag{3.8}$$

From the above equation, it can be seen that all the ions passing through the ion extractor are given the same initial kinetic energy. As the ions drift in the field free mass analyser they are separated by their mass-to-charge ratio, meaning that all ions with the same *m/z* ratio will arrive at the detector at the same time. This makes the TOF-SIMS the most sensitive technique for gathering the elemental composition of a material as it is capable of detecting atomic masses ranging from 0 to 10 000 amu.

With the emission of secondary ions and electrons, samples that are non-conducive may be susceptible to surface charging causing a change in the secondary ion's energy and therefore changing its time of flight. In order to neutralise charging on the surface of the sample, electrons emitted by the electron flood gun are directed towards the sample. The electrons

emitted by the flood gun are low energy electrons (< 20 eV), which reduces the possibility of damaging the sample [39].

In this study, all data were collected using a ionTOF TOF.SIMS 5 equipped with a Bi primary ion source along with a dual sputtering source of oxygen and caesium which can act as two active ion sources. The flight distance from the sample to the analyser is 2 m and the analyser consists of a multi-channel plate with 2 million channels.

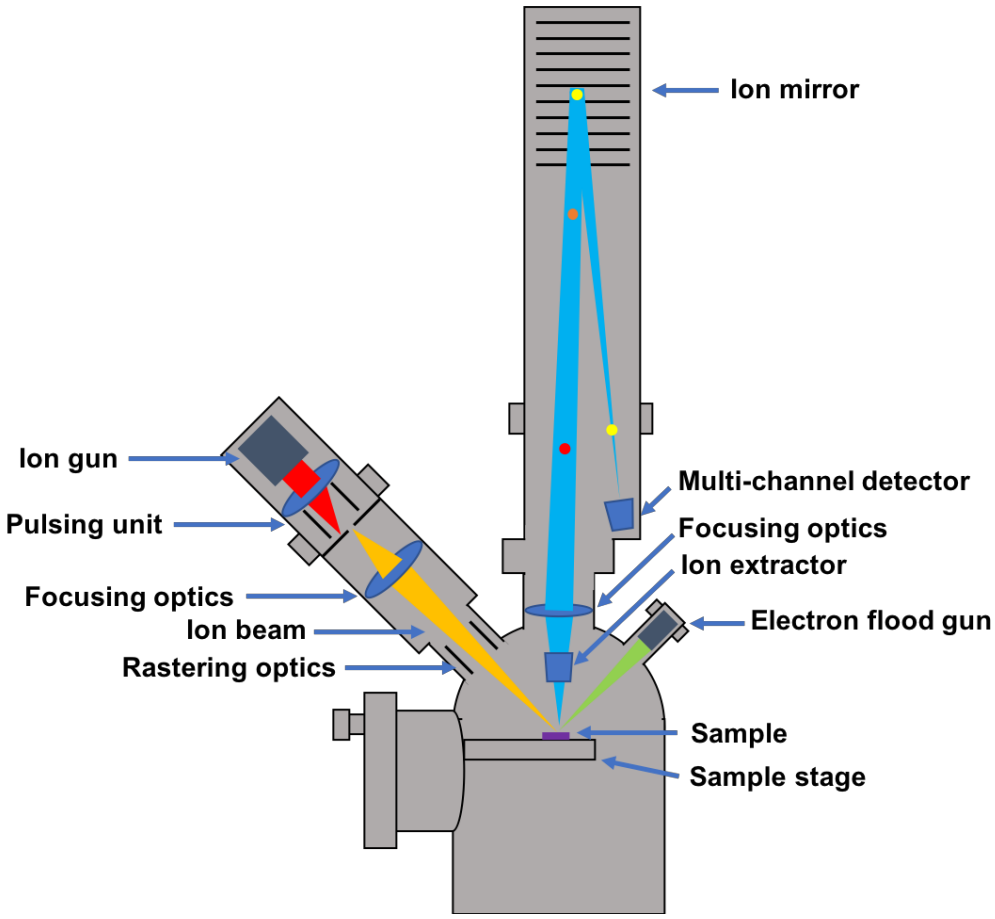

Figure 3.15: Schematic diagram displaying the main components present in the TOF-SIMS. Adapted from [40].

3.3.6. Atomic force microscopy

The AFM is a characterisation technique used to obtain topographical and mechanical information about the material [41]. A schematic showing the main components of the AFM system is given in Figure 3.16. The cantilever is made from silicon nitride with a triangular tip which has a radius of curvature in the order of nanometres and gold film on the back side of

the lever used to reflect the laser beam [42]. The AFM operates by moving a sample across the tip (probe) of the cantilever using the piezo-scanner and measuring the force between the probe and the sample. A focused laser beam is directed towards the back of the lever onto the reflective gold film where it is reflected into a photodetector [41]. Analysing the signals obtained from the different quadrants within the photodetector, the laser deflection can be measured which can be correlated to height measurement at that particular point.

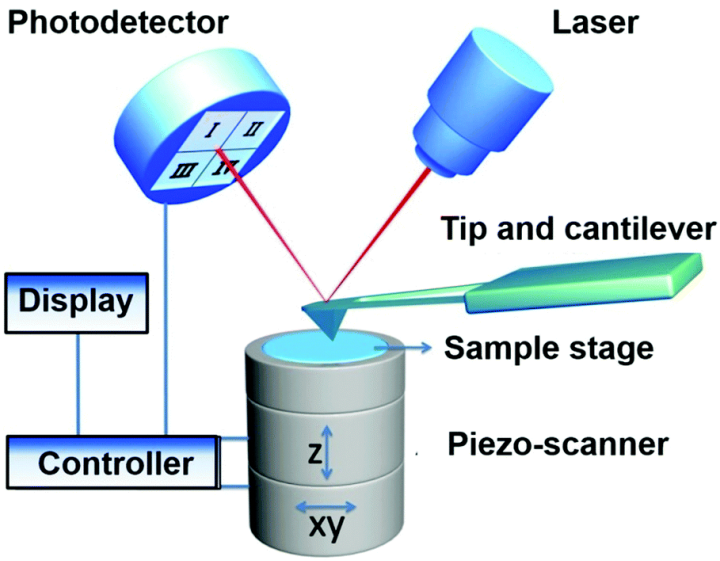

Figure 3.16: Schematic diagram showing the main components used in the AFM setup [43].

In this study, the AFM data was collected using a Shimadzu SPM-9600 scanning probe microscope and the images were captured using the contact mode.

3.4 References

[1] T. P. Mokoena, "Synthesis and luminescence properties of aluminium oxide - titanium dioxide nanocomposites doped with different rare-earth ions", Msc dissertation, *University of the Free State*, *South Africa*, (2016)

[2] J. Li, J. Zhang, X. Zhang, Z. Hao, Y. Luo, "Cooperative downconversion and near infrared luminescence of Tm^{3+}/Yb^{3+} codoped Calcium Scandate phosphor", *J. Alloys Compd.*, **583,** 96–99 (2014)

[3] C. Zhu, S. Martin, R. Ford, N. T. Nuhfer, "Experimental and modeling studies of coprecipitation as an attenuation mechanism for radionuclides, metals, and metalloid mobility", *Geophys. Res. Abstr.*, **5,** 6552 (2003)

[4] H. Henschel, A. M. Schneider, M. H. Prosenc, "Initial Steps of the Sol - Gel Process : Modeling Silicate Condensation in Basic Medium", *Chem. Mater.*, **22,** 5105–5111 (2010)

[5] N. Sahu, B. Parija, S. Panigrahi, "Fundamental understanding and modeling of spin coating process: A review", *Indian J. Phys.*, **4,** 493 (2009)

[6] A. M. Taleb, W. A. A. Twej, B. T. Chiad, A. J. H. Al-wattar, "Study of Spinning Speed, Multilayer Coating and Formaldehyde Effect on Preparation of Xerogel Film Doped with Laser Dyes", *African Phys. Rev.*, **3,** 117–124 (2009)

[7] H. K. Raut, V. A. Ganesh, A. S. Nair, S. Ramakrishna, "Anti-reflective coatings: A critical, in-depth review", *Energy Environ. Sci.*, **4,** 3779–3804 (2011)

[8] D. P. Norton, "Pulsed Laser Deposition of Complex Materials: Progress Toward Applications", *in Pulsed Laser Deopsition of Thin Films* (ed. Eason, R.) , Chapt. 1 *John Wiley & Sons*, (2007)

[9] C. W. Schneider, T. Lippert, "Laser Ablation and Thin Film Deposition", *in Laser Processing of Materials* (ed. Schaaf, P.) , Chapt. 5 *Springer-Verlag Berlin Heidelberg*, (2010)

[10] J. M. Lackner, W. Waldhauser, R. Ebner, W. Lenz, C. Suess, G. Jakopic, G. Leising, H. Hutter, "Pulsed laser deposition: a new technique for deposition of amorphous SiOx thin films", *Surf. Coatings Technol.*, **163–164,** 300–305 (2003)

[11] A. Yousif, R. M. Jafer, J. J. Terblans, O. M. Ntwaeaborwa, M. M. Duvenhage, V. Kumar, H. C. Swart, "TOF SIMS induced artificial topographical effects on the $Y_2(Al,Ga)_5O_{12}:Tb^{3+}$ thin films deposited on Si substrates by the pulsed laser deposition technique", *Appl. Surf. Sci.*, **313,** 524–531 (2014)

[12] D. B. Geohegan, D. N. Mashburn, R. J. Culbertson, S. J. Pennycook, J. D. Budai, R. E. Valiga, B. C. Sales, D. H. Lowndes, L. A. Boatner, E. Sonder, D. Eres, D. K. Christen, W. H. Christie, "Pulsed laser deposition of thin superconducting films of $Ho_1Ba_2Cu_3O_{7-x}$ and $Y_1Ba_2Cu_3O_{7-x}$", *J. Mater. Res.*, **3,** 1169–1179 (1988)

[13] T. Scharf, H. U. Krebs, "Influence of inert gas pressure on deposition rate during pulsed laser deposition", *Appl. Phys. A Mater. Sci. Process.*, **75,** 551–554 (2002)

[14] R. L. Nyenge, H. C. Swart, O. M. Ntwaeaborwa, "The influence of substrate temperature and deposition pressure on pulsed laser deposition thin films of $CaS:Eu^{2+}$ phosphors", *Phys. B Condens. Matter*, **480,** 186–190 (2016)

[15] S. Kiamehr, "Material Solutions to Mitigate the Alkali Chloride-Induced High Temperature Corrosion", PhD thesis, *Techinical University of Denmark*, *Denmark*, (2014)

[16] R. Jenkins, "Encyclopedia of Analytical Chemistry: Applications, Theory and Instrumentation", *John Wiley & Sons*, (2000)

[17] "X-Ray Diffraction Primer", Available at: https://pubs.usgs.gov/of/2001/of01-041/htmldocs/xrpd.htm. (Accessed: 7 September 2017)

[18] B. D. Cullity, "Elements of X-ray diffraction", *Addison-Wesley Publishing Company, Inc*, (1956)

[19] "X-ray spectrum", Available at: https://www.toktol.com/notes/section/981/physics/quantum-physics/x__ray-spectrum (Accessed: 7 September 2017)

[20] W. H. Bragg, W. L. Bragg, "The Reflection of X-rays by Crystals", *Proceeding R. Soc. A*, **88,** 428 (1913)

[21] PPLATO, "The atomic basis of matter", Available at: http://www.met.reading.ac.uk/pplato2/h-flap/phys7_1.html (Accessed: 12 September 2017)

[22] J. R. Lakowicz, "Principles of Fluorescence Spectroscopy", *Springer, New York*, (2007)

[23] H. Photonics, "Photomultiplier Tubes Basic and Applications", *Hamamatsu Photonics K. K.*, (2007)

[24] Scintillator Materials Group, "Research Fundamentals", Available at: https://web.stanford.edu/group/scintillators/scintillators.html (Accessed: 27th September 2017)

[25] A. Rogalski, "Infrared detectors : status and trends", **27,** 59–210 (2003)

[26] PerkinElmer instruments, "Low Level Optical Detection using Lock-in Amplifier Techniques", *PerkinElmer Inc*, (2010)

[27] L. J. B. Erasmus, "Development of an optical thermometry system for phosphor materials", MSc dissertation, *University of the Free State*, *South Africa*, (2017)

[28] Edinburgh Instruments, "FLS980 Series Reference Guide", *Edinburgh Instruments Ltd*, (2016)

[29] C. S. Fadley, "Basic Concepts of X-ray Photoelectron Spectroscopy", *in Electron Spectroscopy Theory, Techniques and Applications* (eds. Brundle, C. R. & Baker, A. D.), Chapt. 1 *Academic Press*, (1978)

[30] A. B. Christie, "X-ray photoelectron spectroscopy", *in Methods of surface analyis techniques and applications* (ed. Walls, J. M.) , Chapt. 5 *Cambridge University Press*, (1989)

[31] S. Hüfner, "Photoelectron Spectroscopy Principles and Application", *Springer Berlin*, (1995)

[32] "Ultra High Vacuum Lab", Available at: http://jacobs.physik.uni-saarland.de/instrumentation/uhvl.htm (Accessed: 22 September 2017)

[33] Wikiwand, "Scanning electron microscope", Available at: https://upload.wikimedia.org/wikipedia/commons/thumb/0/0d/Schema_MEB_%28en%29.svg/640px-Schema_MEB_%28en%29.svg.png?1506800030731 (Accessed: 22 September 2017)

[34] Northern Arizona University, "Electron Microprobe Instrumentation", Available at: https://nau.edu/cefns/labs/electron-microprobe/glg-510-class-notes/instrumentation/ (Accessed: 1 October 2017)

[35] JEOL, "Scanning Electron Microscope A To Z", *JEOL Ltd*

[36] L. Ozawa, "Cathodoluminescence and Photoluminescence: Theories and Pratical Applications", *CRC Press*, (2007)

[37] A. Benninghoven, "Chemical Analysis of Inorganic and Organic Surfaces and Thin Films by Static Time-of-Flight Secondary Ion Mass Spectrometry (TOF-SIMS)", *Angew. Chemie Int. Ed.*, **33,** 1023–1043 (1994)

[38] W. C. Wiley, I. H. Mclaren, "Time-of-Flight Mass Spectrometer with Improved Resolution", *Rev. Sci. Instrum.*, **26,** 1150–1157 (1955)

[39] F. M. Green, I. S. Gilmore, M. P. Seah, "TOF-SIMS : Accurate Mass Scale Calibration", *J. Am. Soc. Mass Spectrom.*, **17,** 514–523 (2006)

[40] V. Smentkowski, "What is ToF-SIMS in Materials Characterization?", *GE Global Research* (2012). Available at: http://ww2.geglobalresearch.com/blog/what-is-tof-sims-in-materials-characterization. (Accessed: 5 May 2018)

[41] B. Bhushan, O. Marti, "No TitleScanning Probe Microscopy - Principle of Operation, Instrumentation, and Probes", *in Nanotribology and Nanomechanics An Introduction* (ed. Bhushan, B.) , Chapt. 2 37–110 *Springer-Verlag Berlin Heidelberg*, (2011)

[42] Shimadzu, "SPM-9600 Scanning probe microscope, instruction manual", *Shimadzu corporation, analytical and measuring instruments division, Kyoto, Japan*

[43] Y. Shan, H. Wang, "The structure and function of cell membranes examined by atomic force microscopy and single-molecule force spectroscopy", *Chem. Soc. Rev.*, **44,** 3617–3638 (2015)

Chapter 4: The synthesis of $Y_2O_3:Bi^{3+}$ phosphor by co-precipitation and the effects of pH on the luminescent properties

In this chapter, the changes in structural, compositional and luminescence properties of $Y_2O_3:Bi_{2.0\ mol\%}$ due to changes in the pH during synthesis was investigated. Characterisation was done using the various research techniques discussed in Chapter 3. The XRD pattern revealed that pH primarily affected the crystallite size of the phosphor material. EDS showed that the Bi^{3+} were homogenously distributed within the material. Lastly the PL analysis showed the emission intensity of the material was dependant on the pH during the synthesis procedure and also that two emission centres were present, which were associated with the two sites (C_2 and S_6) that Bi^{3+} ions may occupy within the Y_2O_3 host matrix.

4.1 Introduction

Luminescent materials doped with rare-earth elements are used extensively in the lighting industry, as they are able to produce a wide variety of electromagnetic radiation ranging from the ultraviolet (UV) through the visible and near-infrared (NIR) regions [1,2]. The process of down-conversion using RE^{3+}-Yb^{3+} (RE = Tb, Ce, Er and Pr) co-doped phosphors have gained interest for improving the efficiency of solar cells [3]. Unfortunately, rare-earth metals are generally poor at absorbing photons in the UV to blue regions due to their parity forbidden 4f transition [4]. Thus, more attention has been placed on metal ions as possible alternatives to the current rare-earth sensitisers [5,6]. Metal ions such as Bi^{3+} which has a $6s^2$ electron configuration, making the $6s^2 \rightarrow 6s6p$ transition an allowed transition [7]. The $6s^2$ ground state splits into a singular singlet $^1S_0$ level while the 6s6p excited state splits into four levels: three triplet levels ($^3P_0$, $^3P_1$ and $^3P_2$) and a singlet level ($^1P_0$) [8,9]. Due to the spin-orbital coupling transitions between $^1S_0$ to $^3P_1$ and $^1P_1$ are allowed transitions, whereas transitions from $^1S_0$ to $^3P_0$ and $^3P_2$ are forbidden as a result of the Δj selection rule [6,9]. As mentioned in Section 2.5.1 Y_2O_3 is used as the host material for its good optical, physical and thermal properties. Y_2O_3 crystallises into a C-type cubic structure containing two different cation sites namely, the C_2 site which is non-centrosymmetric and the centrosymmetric S_6 site [10–12].

In this study we will investigate $^1S_0 \rightarrow {}^3P_1$ transition of Bi^{3+} as its absorption occurs in the desired UV region (300 – 400 nm). The effect of pH and the two cation sites of Y_2O_3, on the emission of the phosphor will be studied and characterised using techniques such as XRD, SEM, EDS, XPS and PL.

4.2 Experimental procedure

The $Y_2O_3 : Bi^{3+}$ powder phosphor was prepared using the co-precipitation technique discussed in Section 3.2.1. Synthesis of the phosphor material was performed at a pH of 6, 7, 9 and 10 to study their effect on the luminescence properties of the material.

The phase structure was characterised from the XRD spectrum using a Bruker D8 Advance diffractometer with KαCu X-rays (1.54Å). The excitation and emission properties were measured using a Varian Cary Eclipse fluorescence spectrometer equipped with a xenon lamp. The particle morphology and chemical composition were captured and measured using a Jeol JSM-7800F Field Emission SEM equipped with an Oxford Artic EDS. X-ray photoelectron spectroscopy measurement were carried out using a PHI 5000 Versaprobe.

4.3 Results and Discussion

4.3.1. Structural analysis

The XRD pattern for the Y_2O_3:$Bi_{2.0\ mol\%}$ phosphor powder prepared at varying pH levels is shown in Figure 4.1 along with the JCPDS file number 01-83-0927 reference data. The structure of the prepared materials was consistent with the referenced data indicating that the prepared powder samples crystallised into a single phase cubic structure with a Ia-3 space group.

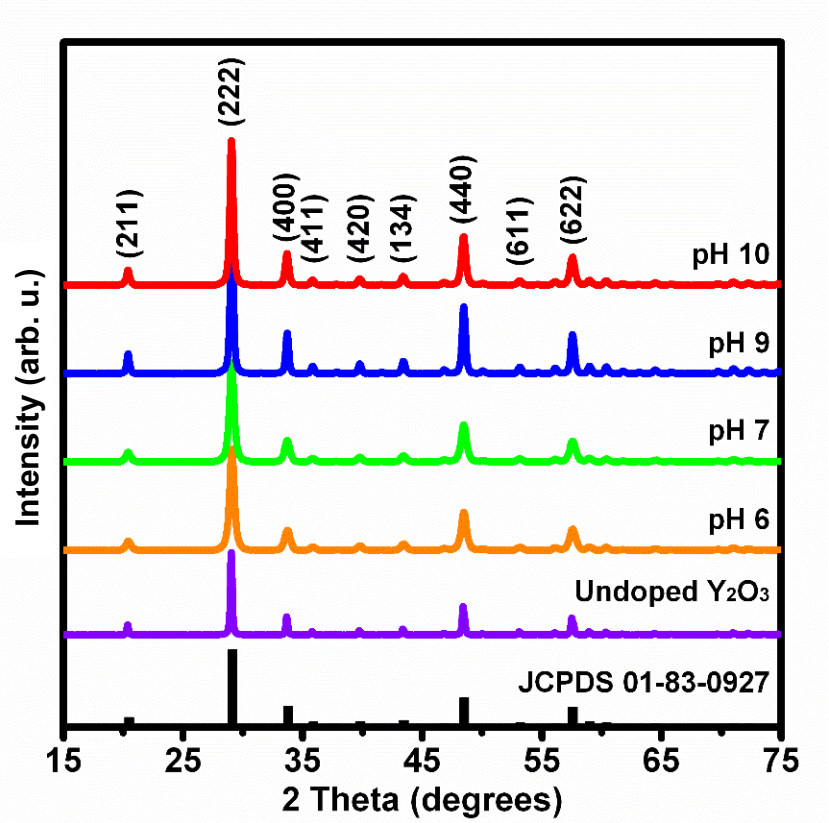

Figure 4.1: XRD pattern of Y_2O_3:$Bi_{2.0\ mol\%}$ phosphor powder synthesised at varying pH levels.

The doping of Bi^{3+} caused shifting of the peaks to lower Bragg angles shown in Figure 4.2. This shifting is an indication of lattice distortions caused by the difference in the ionic radius of Bi^{3+} (0.103 nm) and of Y^{3+} (0.090 nm) ions. This indicates that Bi^{3+} ions were successfully introduced into the Y_2O_3 host material [13]. The lattice parameter, shown in Table 4.1, of the undoped host material and doped material synthesised at different pH levels were calculated using the Bragg expression (eq. 4.1 and 4.2). The result shows a slight increase in the lattice parameter of the doped material as compared to the undoped material, which was expected as the ionic radius of the Bi^{3+} ion is slightly larger than that of Y^{3+} ion [13]. Additionally, the lattice parameters of the materials synthesised at different pH levels correspond well with each other, which was again expected as the amount of doped Bi^{3+} ions was kept constant.

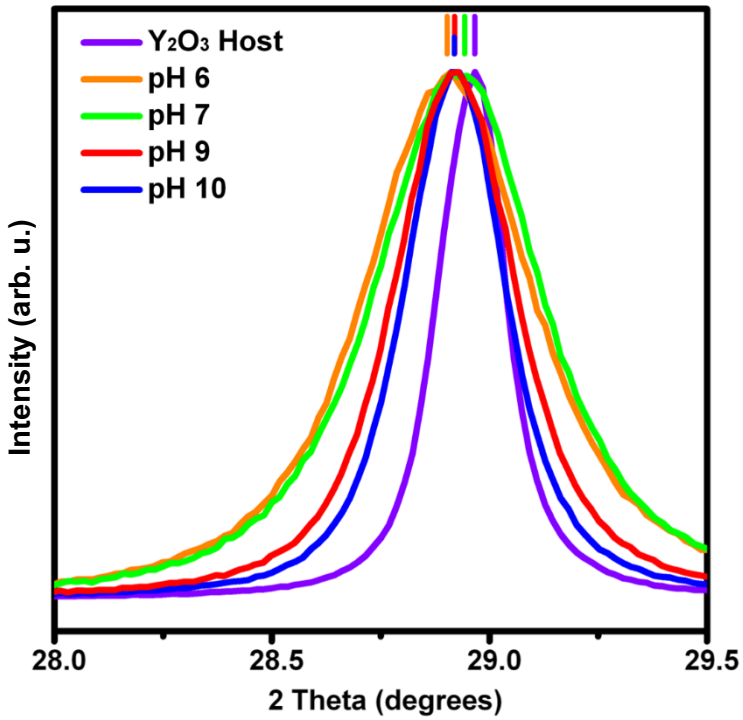

Figure 4.2: (222) peak analysis of Y_2O_3:$Bi_{2.0\ mol\%}$ synthesised at different pH levels.

With an increase in pH narrowing of the Y_2O_3 diffraction peaks were observed. The narrowing of these peaks can be caused by factors such as instrumental parameters, strain within host lattice and crystallite size of the prepared material. As the samples were analysed using the same system parameters under the same conditions, changes in the full-width half maximum (FWHM) of the diffraction peaks are largely attributed to the stain and crystallite size of the prepared material, which can be determined using the Williamson-Hall plot. The equation used to construct the Williamson-Hall plot is given by,

$$\frac{\beta_{hkl}\cos\theta}{K\lambda} = \frac{4\varepsilon\sin\theta}{K\lambda} + \frac{1}{D} \tag{4.1}$$

where β_{hkl} is the full width at half maximum (FWHM) of the diffraction peak, θ is the Bragg angle, K is a constant usually 0.9, related to the crystallite shape of a spherical crystal with a cubic unit cell, λ is the wavelength in nm of the X-ray used, ε represents the strain and D the crystallite size. The results from the plot are tabulated in Table 4.1.

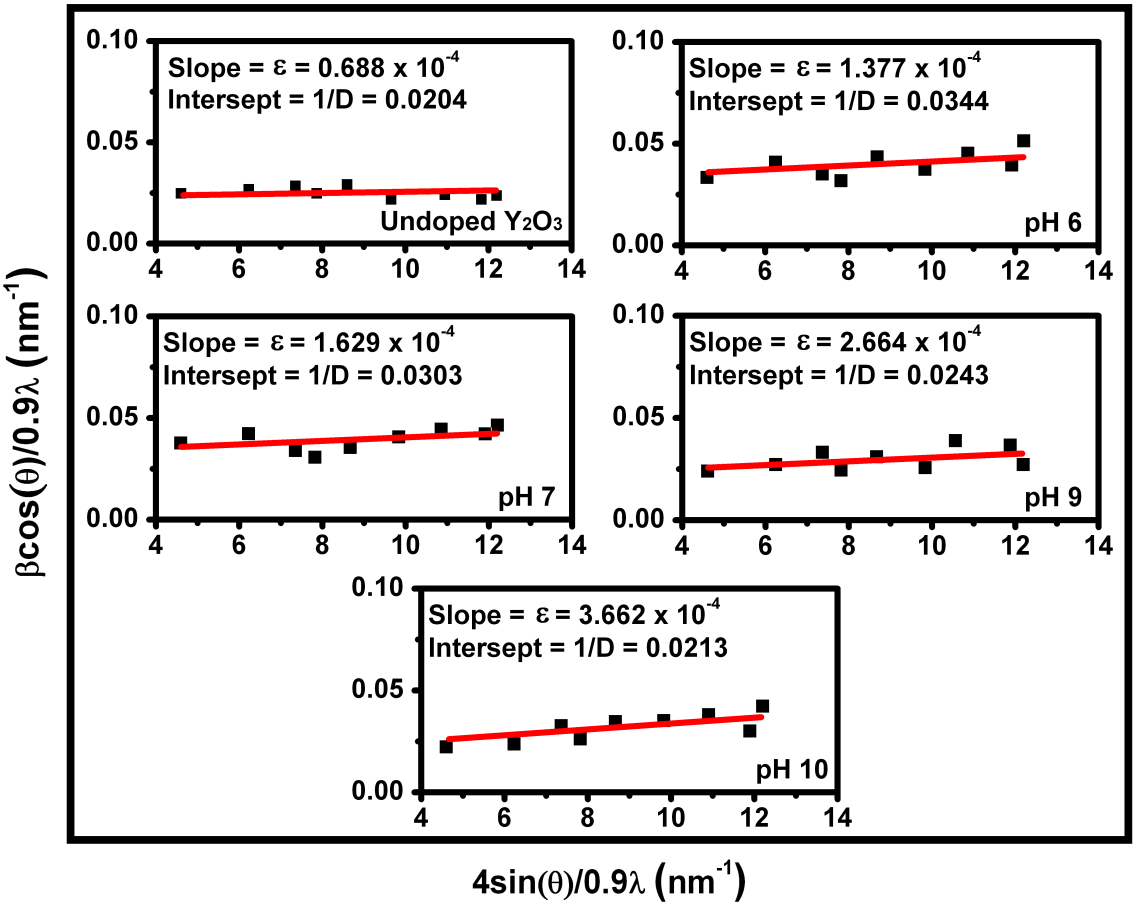

Figure 4.3: Williamson-Hall plot of undoped Y_2O_3 and Y_2O_3:$Bi_{2.0\ mol\%}$ synthesised at different pH levels.

Table 4.1: The structure for both undoped Y_2O_3 and Y_2O_3:$Bi_{2.0\ mol\%}$ phosphor synthesised at different pH levels (JCPDS lattice parameter a = 10.60 Å).

Sample	Lattice parameter a (Å)	Crystallite size D (nm)	Micro-strain ε (x 10^{-4})
Undoped Y_2O_3	10.61	49 ± 5	0.688
pH 6	10.62	29 ± 7	1.377
pH 7	10.62	31 ± 6	1.629
pH 9	10.63	41 ± 7	2.664
pH 10	10.63	47 ± 8	3.662

With an increase in the pH during synthesis the lattice parameter remained fairly consistent as the concentration of Bi ions present were kept constant. An increase in pH does however change the crystallite size of the final product. With pH = 6 the solution has an acidic nature

which may restrain the growth of the particles. At pH greater than 7 the solution became alkaline and therefore supports in hydrolysis which enhanced particle growth, increasing the particle size [14].

4.3.2. Compositional analysis

The XPS technique was used to obtain the chemical states of the Y_2O_3:$Bi_{2.0\ mol\%}$ phosphor material. The XPS survey spectra of Y_2O_3:$Bi_{2.0\ mol\%}$ prepared at a pH 6 and 10 are shown in Figure 4.4.

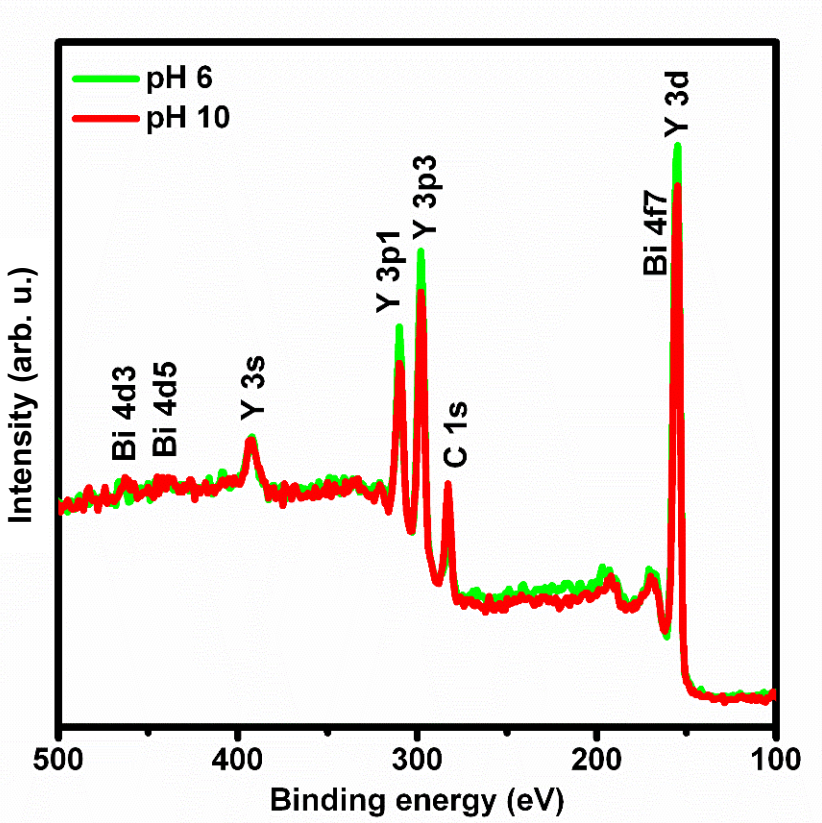

Figure 4.4: XPS survey spectra of Y_2O_3:$Bi_{2.0\ mol\%}$ synthesised at pH 6 and pH 10.

To compensate for the effect of charging on the material during analysis carbon (C) 1s was used to correct the XPS spectrum. A closer look at the C 1s high resolution scan showed that the peak was asymmetric which indicates that several chemical bond components for carbon were present. A deconvolution of the C 1s was performed in order to resolve the different carbon bonds as seen in Figure 4.5. The results show that the measured binding energy value for the C-C chemical bond was 282.6 eV. The known binding energy for the C-C chemical

bond was 284.8 eV which was 2.2 eV more than that of the measured value. The deviation in the binding energy is due to charging of the material and as a result all measured spectrums were shifted by 2.2 eV when processing the data.

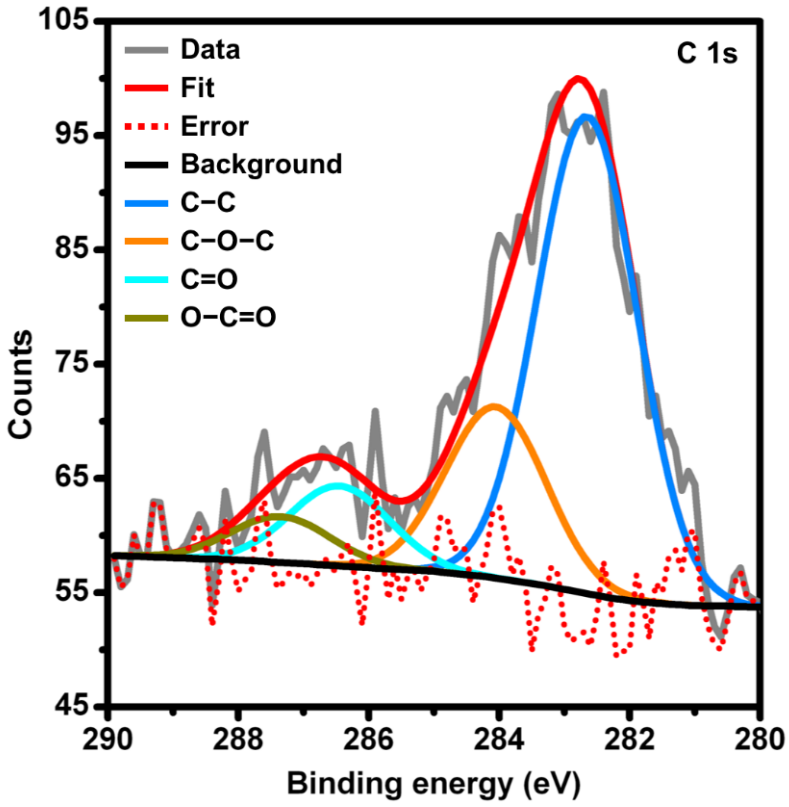

Figure 4.5: High resolution XPS peak deconvolution of C 1s peak for Y_2O_3:$Bi_{2.0\ mol\%}$ synthesised at pH 10.

Similar to the C 1s peak, both the Y 3d and O 1s peaks were asymmetric which indicates that the Y and O ions reside in more than one coordination site within the host crystal structure leading to more than one bonding state. Through the deconvolution of the Y 3d spectra it was revealed that ten sub peaks were combined to produce the Y 3d peak as shown in Figure 4.6. Due to the spin orbital coupling the Y 3d and Bi 4f photoemission peak split into two peaks which are assigned to the Y $3d_{3/2}$, Y $3d_{5/2}$ and Bi $4f_{5/2}$, Bi $4f_{7/2}$ peaks [15]. The binding energy for the Y $3d_{5/2}$ in Y_2O_3 was referenced at 156.8 eV [16]. The peaks found at 156.5 and 158.7 eV was attributed to the Y^{3+} $3d_{5/2}$ and Y^{3+} $3d_{3/2}$ ions located in the C_2 site, while the peaks at 157.3 and 159.5 eV were for the Y^{3+} $3d_{3/2}$ and Y^{3+} $3d_{5/2}$ ions found in the S_6 site. The binding energy for Bi $4f_{7/2}$ was referenced at 159.3 eV [16]. Therefore, the peaks found at 158.7 and 163.9 eV were assigned to the Bi^{3+} $4f_{7/2}$ and Bi^{3+} $4f_{5/2}$ ions positioned in the C_2 site while the

peaks located at 159.9 and 165.1 eV were attributed to the Bi^{3+} $4f_{7/2}$ and Bi^{3+} $4f_{5/2}$ ions found in the S_6 site. The two final peaks associated to the binding energy of Y^{3+} $3d_{3/2}$ and Y^{3+} $3d_{5/2}$ bound to OH was positioned at 157.6 eV and 160.3 eV respectively [17]. The broad peak centred at around 170 eV, also known as a "Shake-Up" peak was caused by the inelastic energy loss emerging from the sample. During the measurement process, a well-defined Y 3d peak was formed as photoelectrons emerging from the sample had little to no energy loss before reaching the detector. This is however not the case for all the photoelectrons, some electrons may interact with its environment (other electrons and atoms) thus losing some of its kinetic energy before reaching the detectors, which increased the background at binding energies higher than the main Y 3d peak [17].

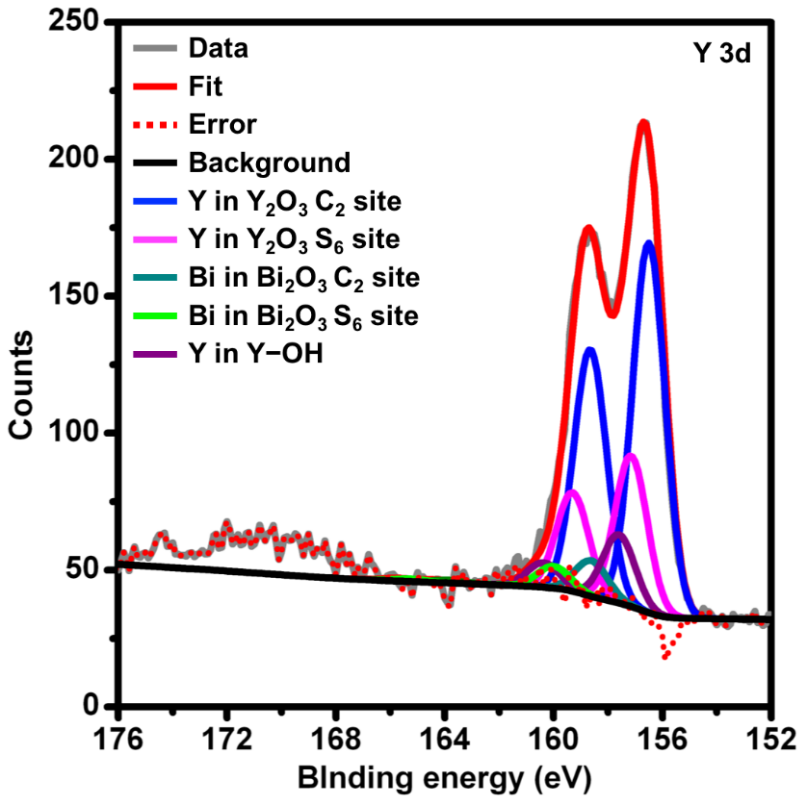

Figure 4.6: High resolution XPS peak deconvolution of Y 3d peak for Y_2O_3:$Bi_{2.0\ mol\%}$ synthesised at pH 10.

Figure 4.7 shows the deconvolution of the O1s XPS spectra, which revealed that the O 1s peak consisted of eight sub peaks. The standard binding energy of O^{2-} in Y_2O_3 was located at 530 eV [18]. Thus, the two peaks found at positions 529.1 eV and 530.1 eV were assigned to O^{2-} ions located in the C_2 and S_6 site respectively within the host Y_2O_3 host. The other two peaks

found at 530.4 eV and 531.5 eV were assigned to the O^{2-} ions located in the two different sites present in Bi_2O_3. The peak situated at 530.9 eV was due to the Y–OH bond which was referenced to have a binding energy of 531.7 eV [19]. The peaks associated with the C–O–C bond, C=O bond and O–C=O bond were located at 531.6 eV, 532.0 eV and 533.1 eV respectively [16].

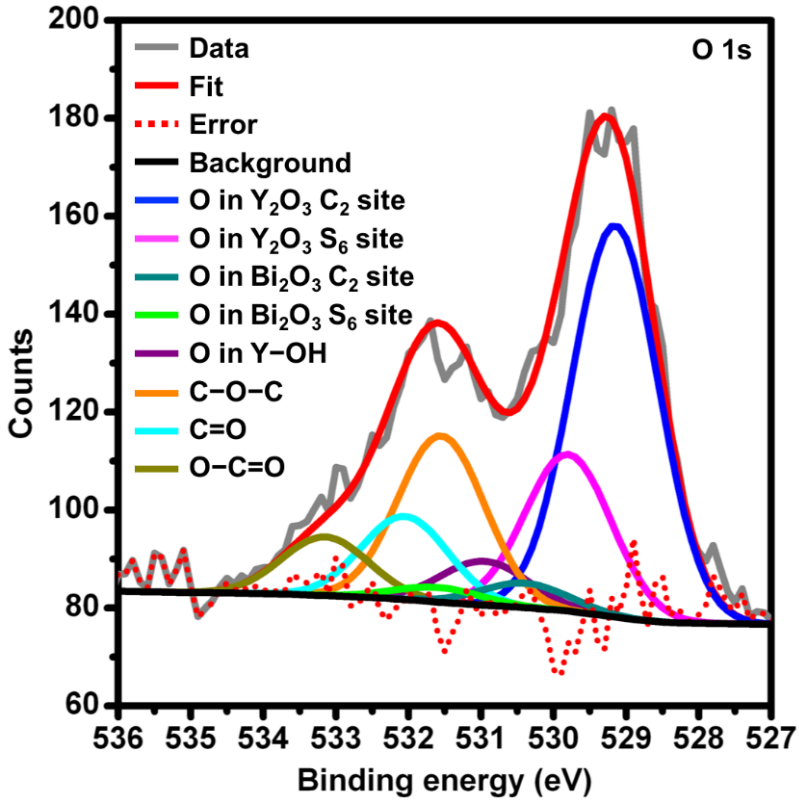

Figure 4.7: High resolution XPS peak deconvolution of O 1s peak for Y_2O_3:$Bi_{2.0\ mol\%}$ synthesised at pH 10.

The EDS spectra shown in Figure 4.8 depicts the elemental analysis of Y_2O_3:$Bi_{2.0\ mol\%}$ phosphor powder synthesised at pH 10. EDS spectrum confirmed that Y, O, Bi were present in the analysis area shown by the SEM micrograph insert within the sample as expected. An elemental map showing the distribution of the elements is also presented in Figure 4.8. From the elemental map, it can be seen that Bi^{3+} ions were very well distributed within the Y_2O_3 host material as a result of the co-precipitation synthesis technique.

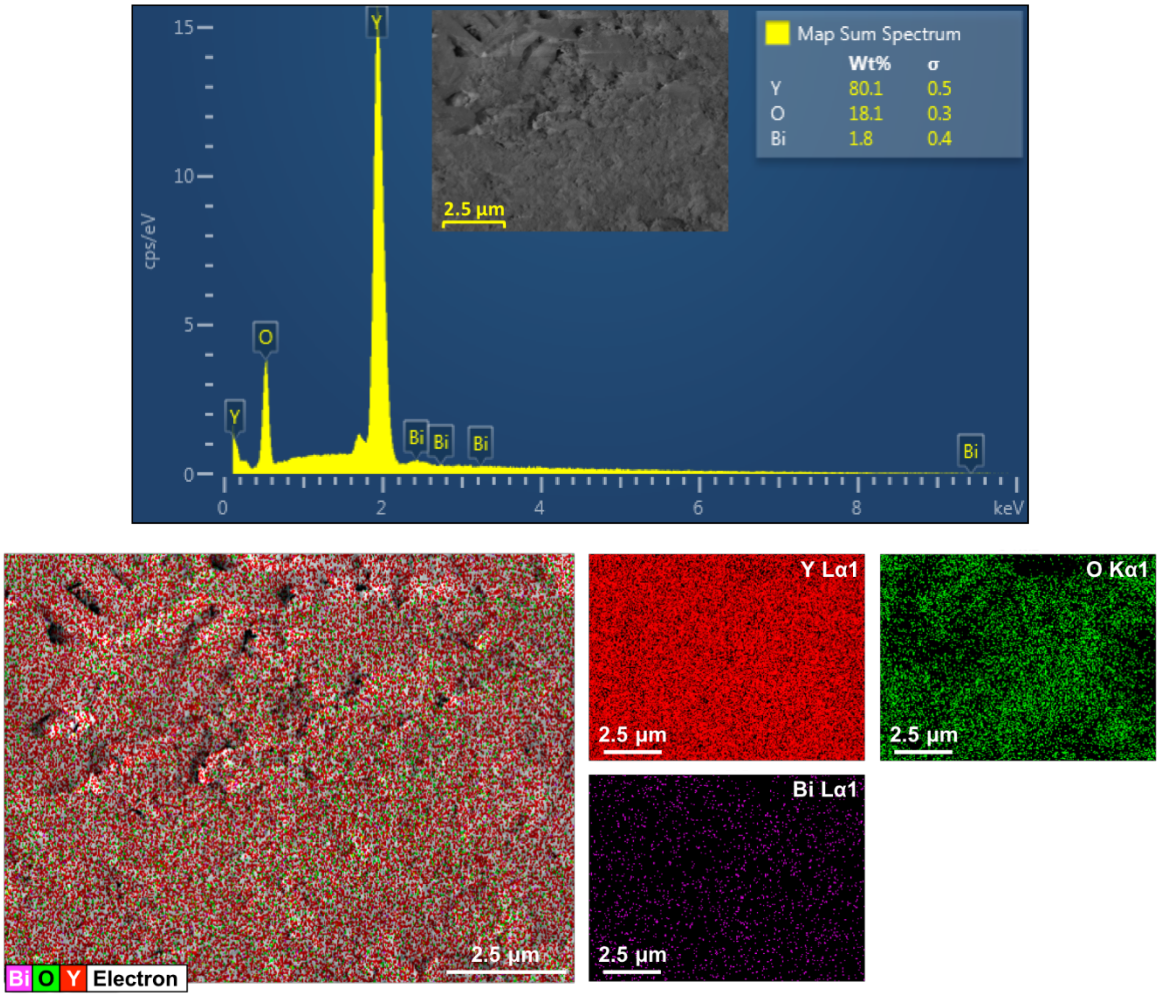

Figure 4.8: EDS spectra and elemental mapping of Y_2O_3:$Bi_{2.0\ mol\%}$ powder phosphor synthesised at pH 10.

4.3.3. Luminescence properties

Figure 4.9a shows the PL excitation and emission spectra of Y_2O_3:$Bi_{2.0\ mol\%}$ synthesised at pH 10, measured at room temperature. The spectrum consists of a combination of two excitation and emission spectra which were produced by the two sites, namely the C_2 and S_6, that the Bi^{3+} ions occupy within the Y_2O_3 host lattice. Firstly, the emission centred at 409 nm (S_6 site) holds two excitation bands in the UV region, a weaker band centred at 330 nm and a stronger band centred at 371 nm. Similarly, for the second emission centred at 490 nm (C_2 site) two excitation bands were observed, the first centred at 330 nm and the other at 345 nm. Under an excitation wavelength of 330 nm a weaker emission with maxima at 409 nm was observed in addition to the board emission centred at 490 nm. Under 371 nm excitation a single narrow emission band with maximum at 409 nm was observed. The effect of pH on the luminescence intensity of the

phosphor material is shown in Figure 4.9b. With an increase in pH, an increase in both the C_2 and S_6 site emission intensity was observed. As the concentration of the Bi^{3+} was kept constant the cause for the changes in the emission intensity may be caused by charges in the morphology of the material such as changes in the crystallite size [20].

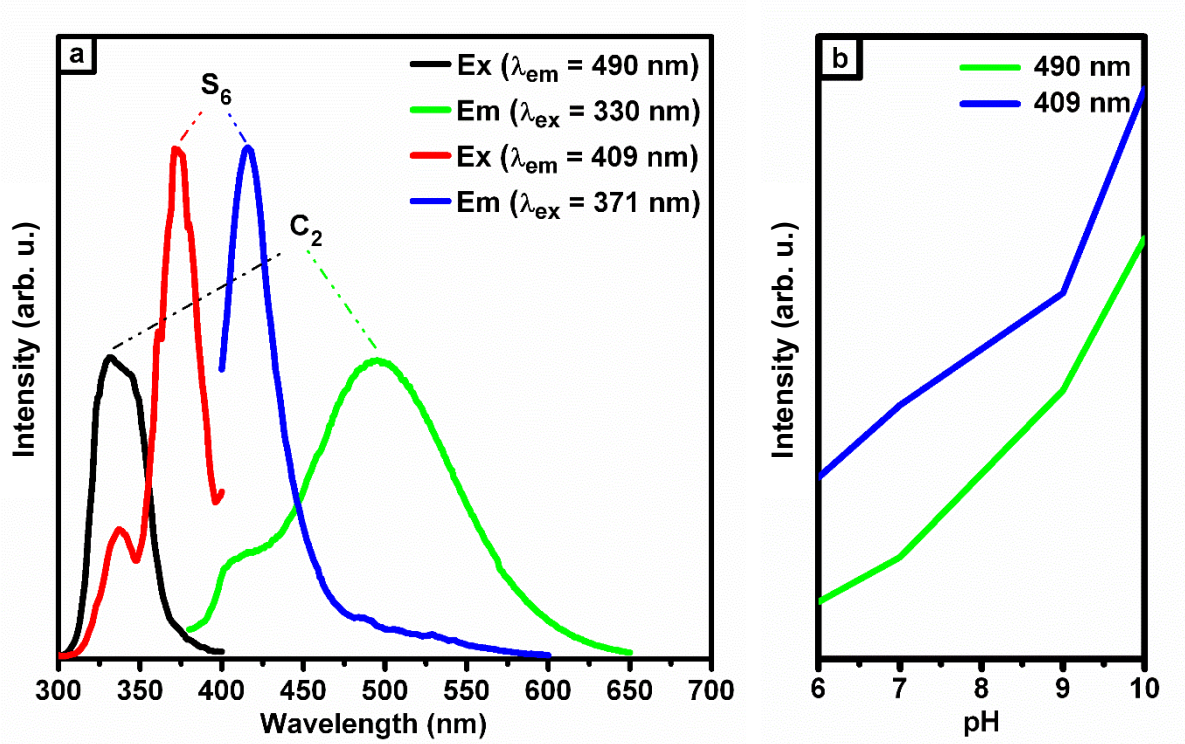

Figure 4.9: (a) Excitation and emission spectra of Y_2O_3:$Bi_{2.0\ mol\%}$ synthesised at pH 10. (b) C_2 and S_6 site emission intensity for Y_2O_3:$Bi_{2.0\ mol\%}$ prepared at different pH levels.

The Bi^{3+} ion emissions are due to the $^3P_1$ to $^1S_0$ transition shown Figure 4.10. The allowed $^3P_1$ level is split into three sub levels (^3A, ^3B, and ^3B) for the C_2 site and two sub levels (^3A_u and ^3E_u) for the S_6 [8]. This splitting is due to the crystal field effect where the Bi^{3+} cations experiences a static electric field caused by the surrounding oxygen anions, which splits the former distinct energy level into multiple sub levels [8,21]. Figure 4.11 shows the chromaticity coordinates for Y_2O_3:$Bi_{2.0\ mol\%}$ phosphor, which was calculated using a CIE coordinated calculator software. The CIE coordinates for the two Bi^{3+} sites were calculated separately and found to be (0.130, 0.290) for the C_2 site and (0.160, 0.029) for the S_6 site.

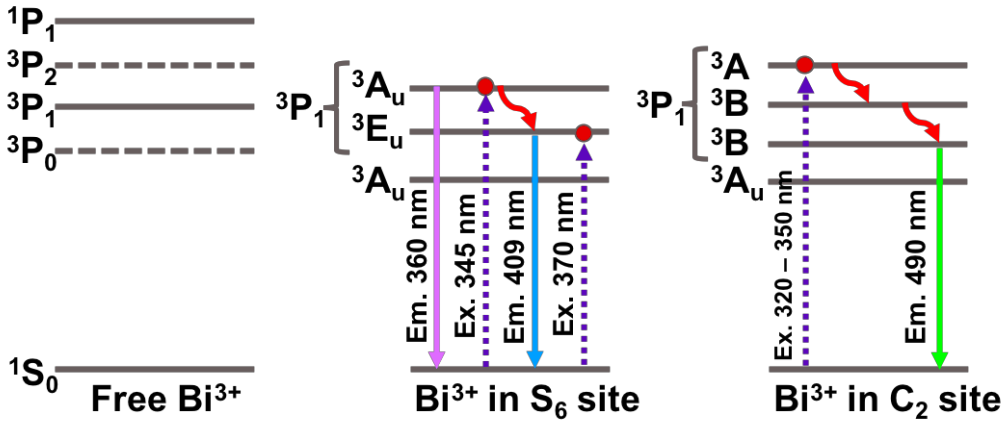

Figure 4.10: Illustration of the energy levels present in Bi^{3+} ion [21].

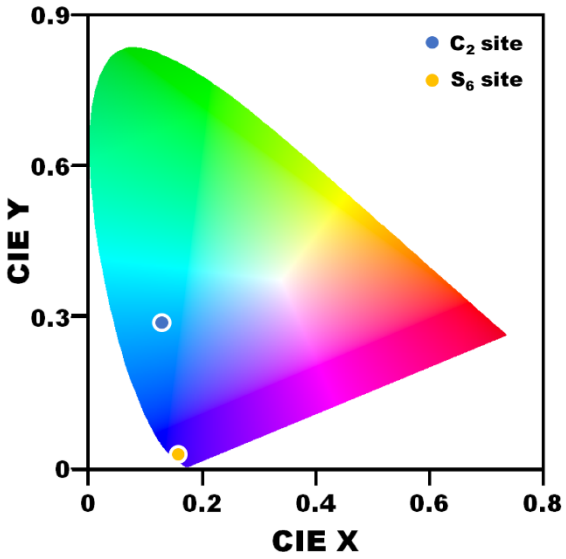

Figure 4.11: Chromaticity coordinates for Bi^{3+} ion present within the C_2 and S_6 sites of the host matrix.

4.4 Conclusion

Using the co-precipitation technique, the Y_2O_3:$Bi_{2.0\ mol\%}$ phosphor powder was successfully synthesised at pH 6, 7, 9 and 10. The XRD pattern revealed that the phosphor material crystallised into a single phase cubic structure with crystallite sizes that varies from 29 nm to 49 nm. Using the XPS and EDS techniques the elements along with its elemental states were acquired and found to be very well distributed within the obtained materials. The PL results showed that two different sites (S_6 and C_2) yields two different visible emissions. Under 371 nm excitation a narrow blue emission was observed corresponding to the S_6 site while a 330

nm excitation yielded a broad green emission originating from the C_2 site. The PL results also showed an increase in the emission intensity of both the 409 nm and 490 nm emission with an increase in the synthesis pH.

4.5 References

[1] C. Feldmann, T. Jüstel, C. R. Ronda, P. J. Schmidt, "Inorganic Luminescent Materials : 100 Years of Research and Application", *Adv. Funct. Mater.*, 511–516 (2003)

[2] B. S. Richards, "Luminescent layers for enhanced silicon solar cell performance: Down-conversion", *Sol. Energy Mater. Sol. Cells*, **90,** 1189–1207 (2006)

[3] T. Trupke, M. A. Green, P. Würfel, "Improving solar cell efficiencies by down-conversion of high-energy photons", *J. Appl. Phys.*, **92,** 1668–1674 (2002)

[4] Q. Y. Zhang, X. Y. Huang, "Progress in Materials Science Recent progress in quantum cutting phosphors", *Prog. Mater. Sci.*, **55,** 353–427 (2010)

[5] U. Rambabu, S. Do Han, "Broad band down conversion from ultra violet light to near infrared emission in $YVO_4:Bi^{3+}$, Yb^{3+} as spectral conversion phosphor for c-Si solar cells", *Ceram. Int.*, **39,** 1603–1612 (2013)

[6] X. Y. Huang, X. H. Ji, Q. Y. Zhang, "Broadband downconversion of ultraviolet light to near-infrared emission in Bi^{3+}-Yb^{3+}-codoped Y_2O_3 phosphors", *J. Am. Ceram. Soc.*, **94,** 833–837 (2011)

[7] L. G. Jacobsohn, M. W. Blair, S. C. Tornga, L. O. Brown, B. L. Bennett, R. E. Muenchausen, "Y_2O_3:Bi nanophosphor: Solution combustion synthesis, structure, and luminescence", *J. Appl. Phys.*, **104,** 124303–7 (2008)

[8] J. Schamps, J. P. Flament, F. Real, I. Noiret, "Ab initio simulation of photoluminescence: Bi^{3+} in Y_2O_3 (S6 site)", *Opt. Mater. (Amst).*, **24,** 221–230 (2003)

[9] V. Kumar, "Effect of swift heavy ion irradiation on nanocrystalline CaS:Bi phosphors : Structural , optical and luminescence studies", *Nucl. Instr. and Meth. in Phys. Res. B*, **262,** 194–200 (2007)

[10] R. M. Jafer, "Luminescence properties of $Y_2O_3:Bi^{3+}$ as powder and thin film phosphor for solar cell application", Msc dissertation, *University of the Free State*, *South Africa*, (2015)

[11] G. Ju, Y. Hu, L. Chen, X. Wang, Z. Mu, H. Wu, F. Kang, "Luminescence properties of $Y_2O_3:Bi^{3+}$, Ln^{3+} (Ln=Sm, Eu, Dy, Er, Ho) and the sensitization of Ln^{3+} by Bi^{3+}", *J. Lumin.*, **132,** 1853–1859 (2012)

[12] A. Huignard, A. Aron, P. Aschehoug, B. Viana, J. Théry, A. Laurent, J. Perrière, "Growth by laser ablation of Y_2O_3 and Tm : Y_2O_3 thin films for optical appications", *J. Mater. Chem.*, **10,** 549–554 (2000)

[13] R. D. Shannon, "Revised effective ionic radii and systematic studies of interatomic distances in halides and chalcogenides", *Acta Crystallogr. Sect. A*, **32,** 751–767 (1976)

[14] M. J. Chithra, M. S. K. Pushpanathan, "Effect of pH on Crystal Size and Photoluminescence Property of ZnO Nanoparticles Prepared by Chemical Precipitation Method", *Acta Metall. Sin. English Lett.*, **28,** 394–404 (2015)

[15] J. F. Watts, J. Wolstenholme, "An Introduction to Surface Analysis by XPS and AES", *John Wiley & Sons, Ltd, Chichester, UK*, (2003)

[16] J. F. Moulder, W. F. Stickle, P. E. Sobol, K. D. Bomben, "Handbook of X-ray Photoelectron Spectroscopy", *Perkin-Elmer Corporation, Minnesota, USA*, (1992)

[17] J. F. Moulder, W. F. Stickle, P. E. Sobol, K. D. Bomben, "Handbook of X-ray Photoelectron spectroscopy", *ULVAC-PHI, Inc. Japan and Physical Electronics USA, Inc. USA*, (1992)

[18] Y. Uwamino, T. Ishizuka, H. Yamatera, "X-ray photoelectron spectroscopy of rare-earth compounds", *J. Electron Spectros. Relat. Phenomena*, **34,** 67–78 (1948)

[19] A. H. Chen, L. Y. Liang, H. Z. Zhang, Z. M. Liu, Y. X. Juan, Z. Yu, C. H. Tao, "Enhancement of a-IZO TTFT Performance by Using Y_2O_3/Al_2O_3 Bilayer Dielectrics", *Electrochem. Solid-State Lett*, **14,** H88–H92 (2011)

[20] W. N. Wang, W. Widiyastuti, T. Ogi, I. W. Lenggoro, K. Okuyama, "Correlations between crystallite/particle size and photoluminescence properties of submicrometer phosphors", *Chem. Mater.*, **19,** 1723–1730 (2007)

[21] F. Ŕeal, B. Ordejón, V. Vallet, J. P. Flament, J. Schamps, "Improvement of the ab initio embedded cluster method for luminescence properties of doped materials by taking into account impurity induced distortions: The example of Y_2O_3:Bi^{3+}", *J. Chem. Phys.*, **131,** 4502 1-17 (2009)

Chapter 5: Effect of Bi concentration on the luminescence properties of $Y_2O_3:Bi^{3+}$ phosphor

This chapter focuses on the optimising of the Bi^{3+} ion concentration that is present within the $Y_2O_3:Bi^{3+}$ phosphor material in order to obtain the strong luminescence intensity. The PL spectra showed that at a high Bi^{3+} ion concentrations (> 2.0 mol%) the luminescence intensity decreased significantly, which was attributed to concentration quenching. In addition to the luminescence properties, the effect of Bi^{3+} ion concentration on both the structural and compositional properties of the $Y_2O_3:Bi^{3+}$ were also studied using the various research techniques mentioned in Chapter 3.

5.1 Introduction

The luminescence properties of Bi^{3+} has gained much attention in recent years for its wide range of possible emission wavelengths from the UV to red region, which depends on the host material used. A free Bi^{3+} ion in its ground state consists of 80 electrons, 78 of which are situated in a closed shell state and are thus inactive from the point of view for UV-visible spectroscopy, while the remaining 2 electrons are situated in the outer $6s^2$ orbital [1]. The $6s^2$ orbital splits into a singular ground state ($^1S_0$) and four possible excitation states ($^3P_0$, $^3P_1$, $^3P_2$, $^1P_0$) [2–4].

In Chapter 5 only the allowed $^1S_0 \rightarrow {}^3P_1$ transition of Bi^{3+} was studied due to the absorption, which occurs between 300 – 400 nm. It was seen that the $^3P_1$ level splits into several sublevels due to the crystal field effect and was dependent on the position of the Bi^{3+} ion in the Y_2O_3 host matrix. In the C_2 symmetry site the $^3P_1$ level splits into three sublevels (^3A, ^3B and ^3B) while the S_6 splits into two sublevels (^3A_u and ^3E_u) [5]

Typically, one would expect an increase in the concentration of the activator ions present within the host material would lead to an increase in the luminescence intensity. However, many experiments show that this is not the case: the luminescence intensity of a phosphor material will increase with an increase in activator ion concentration up to a certain concentration, where after any further increase in the concentration leads to a decrease in the

luminescence intensity [6]. This process is known as concentration quenching where energy from an excitation source is lost due to the cross-relaxation between 2 or more activator ions [7]. The optimum activator concentration differs for various phosphor materials as the type of activator and host material used will dictate the interaction between the host material and activator ions [8].

In this chapter, the effect of Bi^{3+} ion concentration on the luminescence intensity of the phosphor material, while keeping the pH during synthesis constant at pH = 10, was studied. The phosphor material was characterised using different surface, compositional and optical techniques.

5.2 Experimental procedure

The $Y_{2-x}O_3:Bi^{3+}$ phosphor powders were prepared using the co-precipitation method discussed in Section 3.2.1 at varying Bi^{3+} ion concentrations (0.5, 1.0, 2.0, 4.0 and 5.0 mol%) while keeping the pH during synthesis constant at 10.

The phase structure was characterised from the XRD spectrum using a Bruker D8 Advance diffractometer with KαCu X-ray (1.54Å). The excitation and emission properties were measured using a Varian Cary Eclipse fluorescence spectrometer equipped with a xenon lamp. The particle morphology, chemical composition and luminescence were captured and measured using a Jeol JSM-7800F Field Emission SEM equipped with an Oxford Artic EDS and a Gatan Mono CL4. X-ray photoelectron spectroscopy measurements were carried out using a PHI 5000 Versaprobe.

5.3 Results and discussion

5.3.1. Structural analysis

Figure 5.1 presents the XRD patterns for the $Y_{2-x}O_3:Bi_x$ phosphor powder prepared at varying Bi^{3+} concentrations and at a constant pH. The results of the prepared phosphor match well to

the JCPDS file number 01-83-0927 referenced data, indicating that the phosphor material crystallised as a single phase cubic structure with a Ia-3 space group.

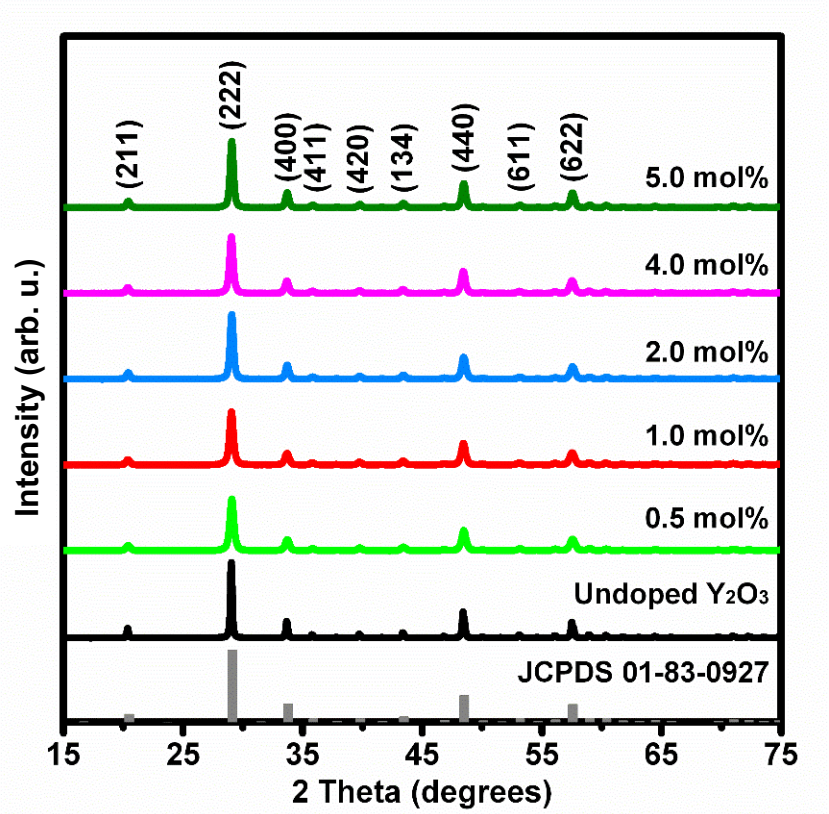

Figure 5.1: XRD pattern for $Y_{2-x}O_3:Bi_x$ synthesised at vary Bi^{3+} concentrations under constant pH 10.

Similar to varying the pH a shift to lower Bragg angles were observed with an increase in the Bi^{3+} ion concentration. This shift, shown in Figure 5.2 was a result of lattice distortions caused by the difference in the ionic radius of Bi^{3+} (0.103 nm) dopant ions and the Y^{3+} (0.090 nm) ions of the Y_2O_3 host lattice [9]. Using all the reflections indicated by a Miller index in Figure 5.1 the lattice parameter of both the undoped and doped materials were determined using the Bragg expression (eq. 4.1 and 4.2) and are tabulated in Table 5.1.

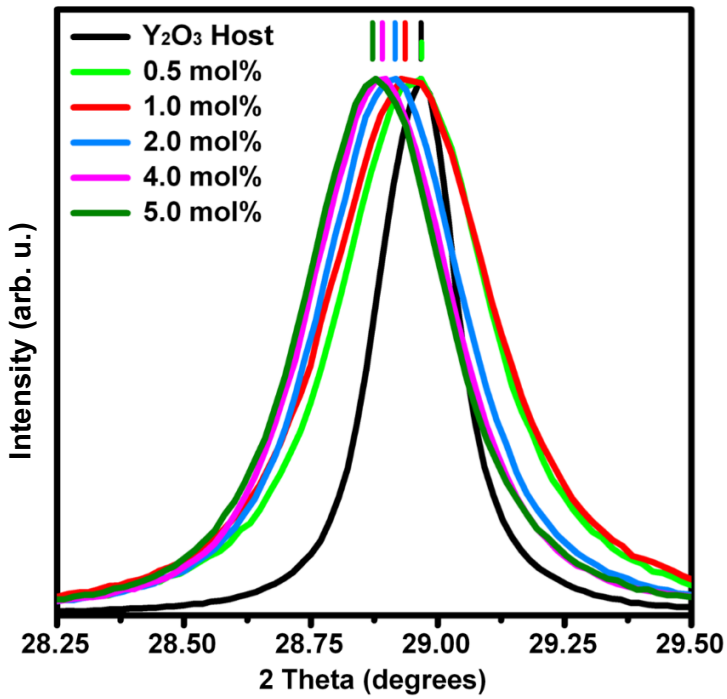

Figure 5.2: (222) peak of $Y_{2-x}O_3:Bi_x$ synthesised with varying Bi^{3+} concentration under constant pH 10.

With an increase in Bi^{3+} concentration a slight variation in the peak width was also observed. As the samples were analysed using the same system parameters under the same environmental conditions any changes in their FWHM were attributed to changes in their crystallite size as well as the strain present in the lattice. Using the Williamson-Hall plot equation (equation 5.1), the plots shown in Figure 5.3 were used to determine the crystallite sizes and strain of the prepared samples and the results are tabulated in Table 5.1.

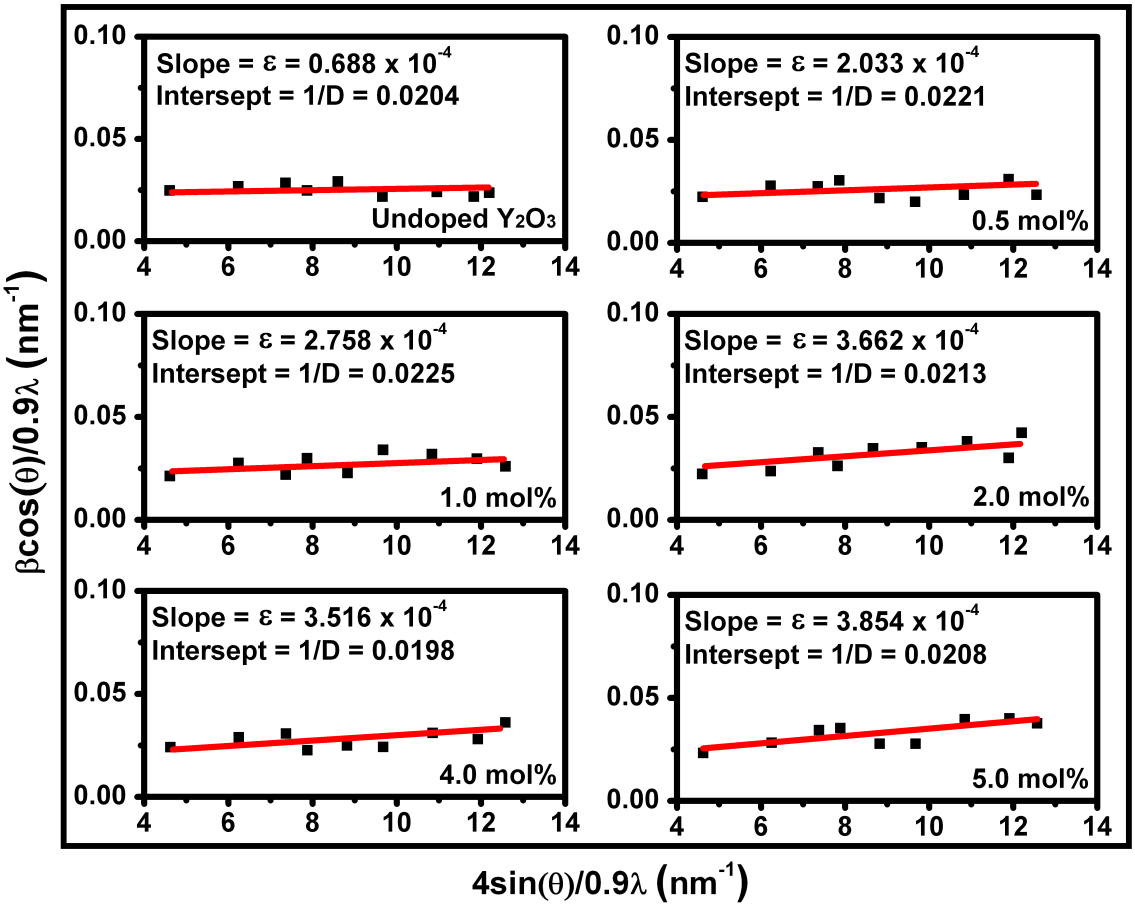

Figure 5.3: Williamson-Hall plot of undoped Y_2O_3 and $Y_{2-x}O_3$:Bi_x synthesised with different Bi^{3+} concentration.

Table 5.1: The structural parameters for both undoped Y_2O_3 and $Y_{2-x}O_3$:Bi_x phosphor synthesised with different Bi^{3+} ion concentrations (JCPDS lattice parameter a = 10.60 Å).

Sample	Lattice parameter a (Å)	Crystallite size D (nm)	Micro-strain ε (x 10^{-4})
Undoped Y_2O_3	10.62	49 ± 5	0.688
0.5 mol%	10.62	46 ± 6	2.033
1.0 mol%	10.62	44 ± 7	2.758
2.0 mol%	10.63	46 ± 8	3.662
4.0 mol%	10.63	50 ± 6	3.516
5.0 mol%	10.64	48 ± 7	3.854

With an increase in Bi^{3+} concentration it was observed that the lattice parameter increased, which was expected as the ionic radius of Bi^{3+} ion is slightly larger than the Y^{3+} ion. The

crystallite size of the prepared samples remained fairly consistent with an increase in Bi concentration, this result shows that the crystallite size was more dependent on the pH than on the concentration on dopants present within the samples.

5.3.2. Compositional analysis

The XPS technique was used to obtain the chemical composition of the elements present in Bi doped Y_2O_3. The survey scan on the surface of Y_2O_3:$Bi_{0.5\ mol\%}$ and Y_2O_3:$Bi_{5.0\ mol\%}$ is shown in Figure 5.4. The peaks centred at 155, 283, 298, 310, 392, 439, 461 and 528 eV were assigned to the Y 3d (superimposed with Bi 4f), C 1s, Y $3p_{3/2}$, Y $3p_{1/2}$, Y 3s, Bi $4d_{5/2}$, Bi $4d_{3/2}$ and O 1s peaks, respectively [10–12].

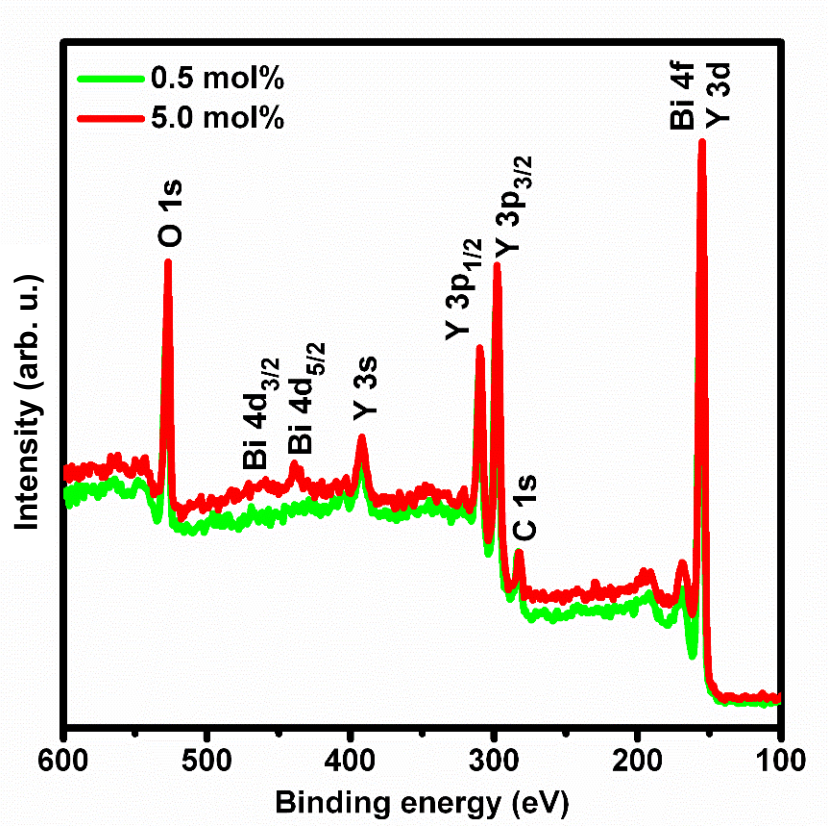

Figure 5.4: XPS survey scan of Y_2O_3:$Bi_{0.5\ mol\%}$ and Y_2O_3:$Bi_{5.0\ mol\%}$.

A high resolution scan of the C 1s spectrum in Y_2O_3:$Bi_{5.0\ mol\%}$ is shown in Figure 5.5. The C 1s peak was used as a reference in order to correct the XPS spectrum due to the effect of charging on the sample material. A closer look at the C 1s peak showed that it was asymmetric which indicates that various carbon chemical bond components were present. To resolve the

various carbon components a deconvolution of the C 1s peak was performed. The results showed that the binding energy of the C-C bond was located at 282.7 eV. The known binding energy for the C-C bond was 284.8 eV, the reference value was 2.1 eV more than the measured value [10]. Thus, all measured spectrums were shifted by 2.1 eV when processing the data to account for charging of the sample material.

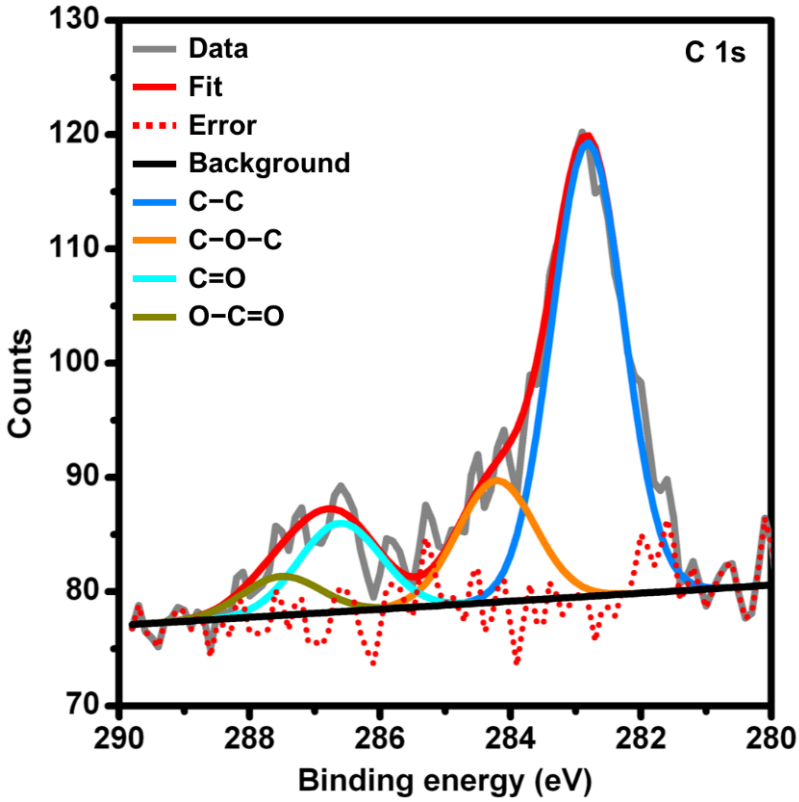

Figure 5.5: XPS peak deconvolution of C 1s peak for Y_2O_3:$Bi_{5.0\ mol\%}$ powder sample synthesised at pH 10.

Similar to the C 1s peak both the O 1s and Y 3d peaks were asymmetric, which were caused by the two possible coordination sites that Bi^{3+}, Y^{3+} and O^{2-} ions may reside within the host matrix. Through deconvolution of the O 1s peak it was revealed that eight sub peaks were combined to form the final O1s peak as shown in Figure 5.6. The peak position for the O 1s in Y_2O_3 was referenced by Uwamino et al and is located at 530 eV [12]. The binding energy peak positions located at 529.2 eV and 530.1 eV were therefore assigned to the O^{2-} found in the two symmetry sites present in the Y_2O_3 host matrix. The two peaks positioned at 530.5 eV and 531.6 eV were assigned to the O^{2-} ions located in the two different sites of Bi_2O_3. The peak located at 531.1 eV was assigned to the Y-OH bond which was referenced by Gougousi et al

to be positioned at 531.7 eV [11]. The final three peaks associated to the C–O–C bond, C=O bond and O–C=O bond were located at 531.7 eV, 532.2 eV and 533.3 eV respectively [10].

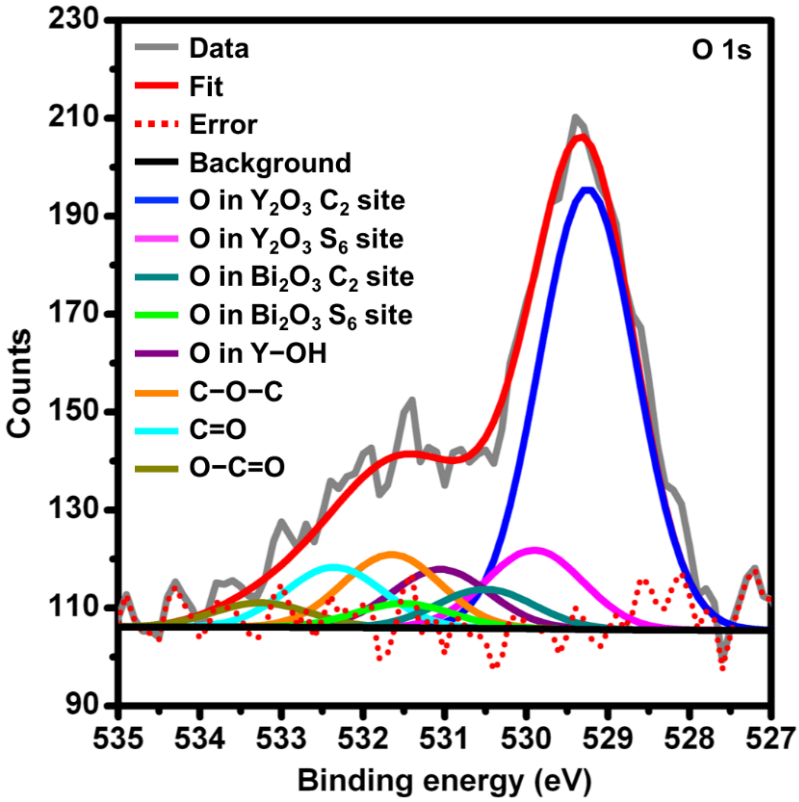

Figure 5.6: XPS peak deconvolution of O 1s peak for Y_2O_3:$Bi_{5.0\ mol\%}$ powder sample synthesised at pH 10.

Through deconvolution ten sub peaks were found to have produced the main Y 3d peak as shown in Figure 5.7. Due to the effect of spin orbital coupling the Y 3d and Bi 4f photoemission peaks were split into the Y $3d_{3/2}$, Y $3d_{5/2}$ and Bi $4f_{5/2}$, Bi $4f_{7/2}$ peaks [13]. The referenced binding energy for the Y $3d_{3/2}$ in Y_2O_3 was 156.8 eV [10]. The peaks with a binding energy of 156.6 eV and 158.7 eV were therefore assigned to the Y^{3+} $3d_{3/2}$ and $3d_{5/2}$ ions found in the C_2 symmetry site while the peaks at 157.4 eV and 159.5 eV were for the Y^{3+} ions located in the S_6 symmetry site. The peaks positioned at 158.6 eV and 163.8 eV were attributed to the Bi^{3+} $4f_{7/2}$ and $4f_{5/2}$ ions found in the C_2 symmetry while the peaks found at 160.0 eV and 165.2 eV were assigned to the Bi^{3+} $4f_{7/2}$ and $4f_{5/2}$ ions found in the S_6 site. Finally, the peaks assigned to Y^{3+} $3d_{3/2}$ and Y^{3+} $3d_{5/2}$ bound to OH were located at 157.6 eV and 159.7 eV respectively [14]. The broad peak centred at around 170 eV is known as the Shake-Up peak discussed in the previous chapter (section 5.3.2) [15].

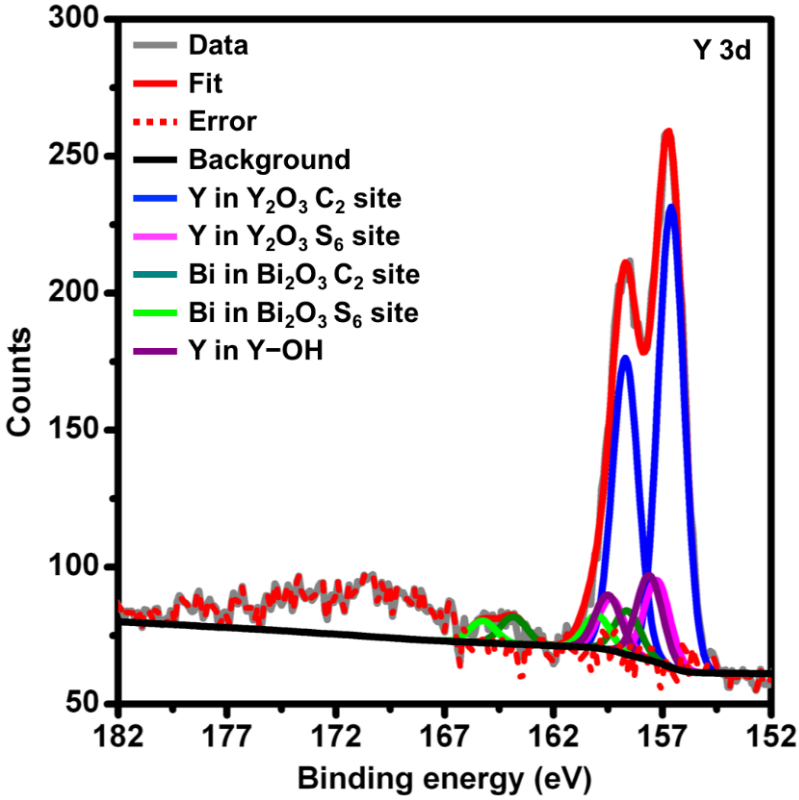

Figure 5.7: Deconvolution of Y 3d XPS peak for Y_2O_3:$Bi_{5.0\ mol\%}$ powder sample synthesised at pH 10.

Figure 5.8 shows the EDS spectrum depicting the elemental analysis of Y_2O_3:$Bi_{5.0\ mol\%}$ phosphor synthesised at pH 10. The analysis confirmed that Y, O and Bi were present in the area shown by the SEM image insert. The elemental mapping showing the distribution of the elements was also represented in Figure 5.8. The elemental map showed that the Bi^{3+} dopant ions were very well distributed within the Y_2O_3 host matrix due to the co-precipitation synthesis technique.

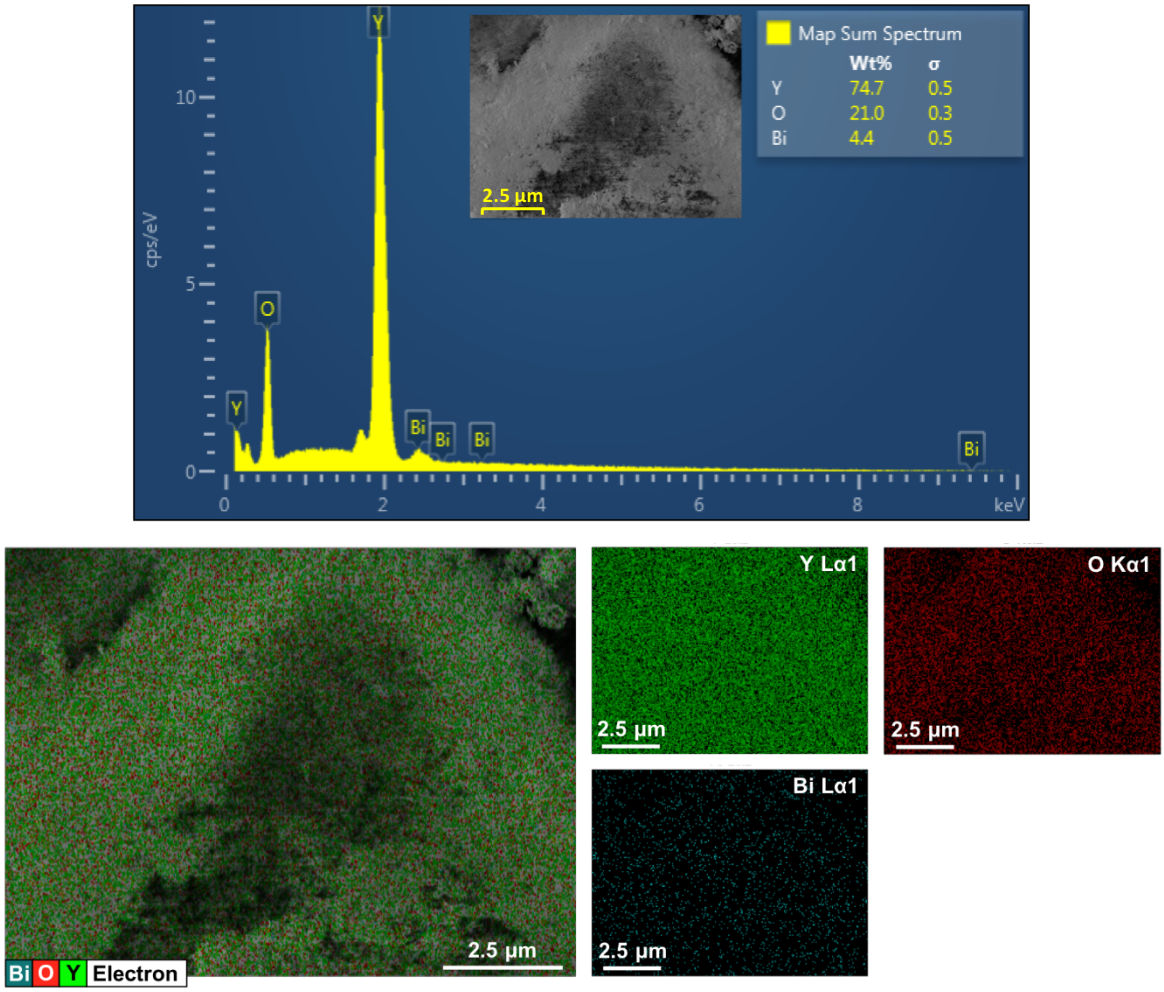

Figure 5.8: EDS spectrum and elemental mapping of Y_2O_3:$Bi_{5.0\ mol\%}$ powder phosphor synthesised at pH 10.

5.3.3. Luminescence properties

Figure 5.9a shows the excitation and emission spectra of Bi^{3+} (5 mol%) doped Y_2O_3, which was obtained by exciting the sample with a xenon lamp at room temperature. The two emission bands, corresponding to the C_2 and S_6 symmetry sites that Bi^{3+} ions may occupy within the Y_2O_3 host material were obtained by monitoring the excitation centred at 330 nm and 390 nm, respectively. The excitation spectrum for Bi^{3+} ions occupying the S_6 and C_2 symmetry site were obtained by monitoring the emission band centred at 409 nm and 490 nm, respectively. All four spectrums occurred due to the $^1S_0 \rightarrow {}^3P_1$ and $^3P_1 \rightarrow {}^1S_0$ transition of Bi^{3+}. Figure 5.9b shows the 490 nm emission intensity as function of Bi^{3+} concentration. With an increase in Bi^{3+} ion concentration an increase in the emission intensity was observed until a maximum and

decreased thereafter. The decrease in intensity was due to concentration quenching where energy was lost due to cross-relaxation between the Bi^{3+} ions (section 2.4.2).

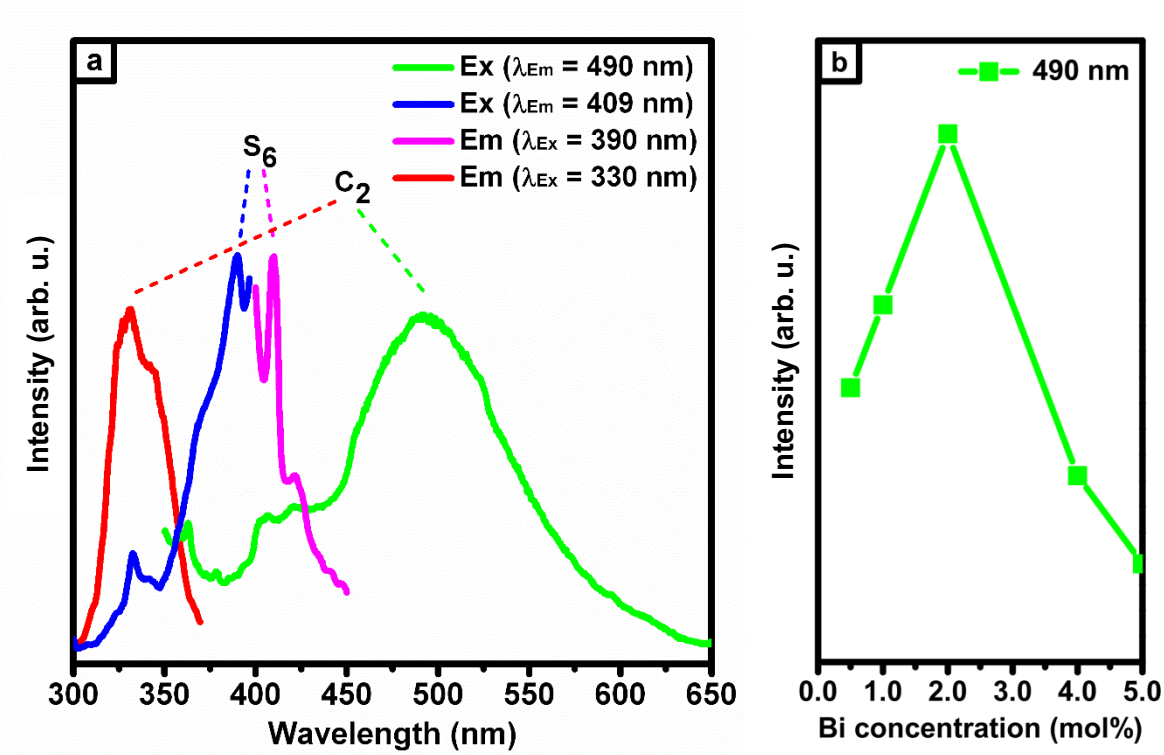

Figure 5.9: (a) Excitation and emission spectra of Y_2O_3:$Bi_{5.0\ mol\%}$ synthesised at pH 10. (b) C_2 site emission intensity for Y_2O_3:$Bi_{5.0\ mol\%}$ prepared at different Bi concentration.

In addition to quenching of the Bi emission, changes in the PL intensity ratio between the S_6 and C_2 sites were also observed and shown in Figure 5.10. From the results a change in the relative emission intensities between the 409 nm and 490 nm Bi emission was observed with an increase in Bi concentration. When the Bi concentration was increased to 2.0 mol% an increase in the intensity ratio between the 409 and 490 nm emission was seen. This observation suggests that the Bi^{3+} ions would preferably occupy the S_6 as the distance separation between the anion and cation is overall larger in the S_6 site than in the C_2 site (section 2.5.1). With a further increase in the Bi concentration the intensity ratio between the 409 nm and 490 nm suddenly decreased. The process can be caused by several factors such as (1) at high Bi concentrations the number of S_6 sites for Bi ions to occupy decreased forcing the ions to occupy the C_2 site, and/or (2) the S_6 site is much more susceptible to quenching therefore quenched more rapidly than the C_2 site emission.

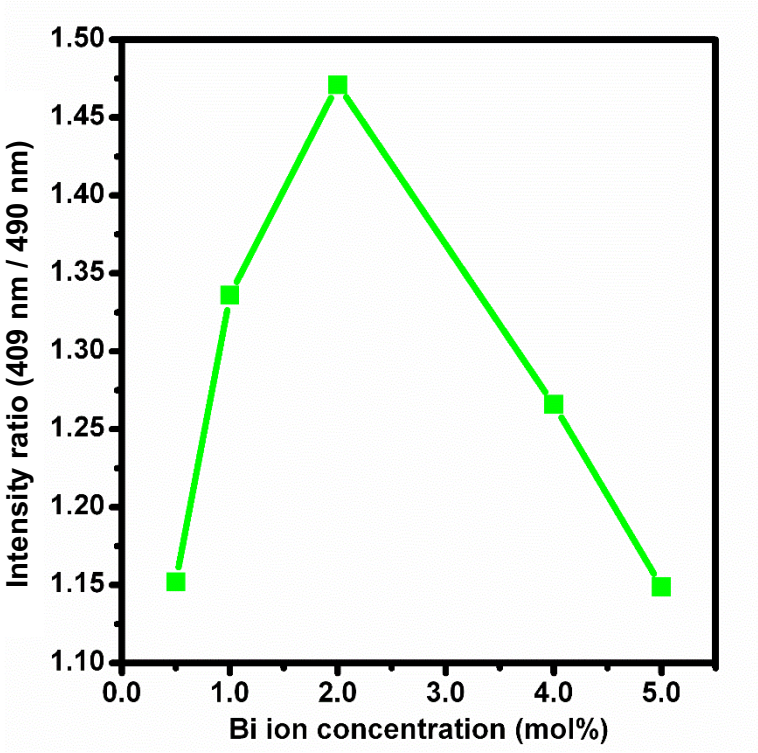

Figure 5.10: Calculated intensity ratio between the 409 nm emission compared to the 490 nm emission with increasing Bi ion concentration.

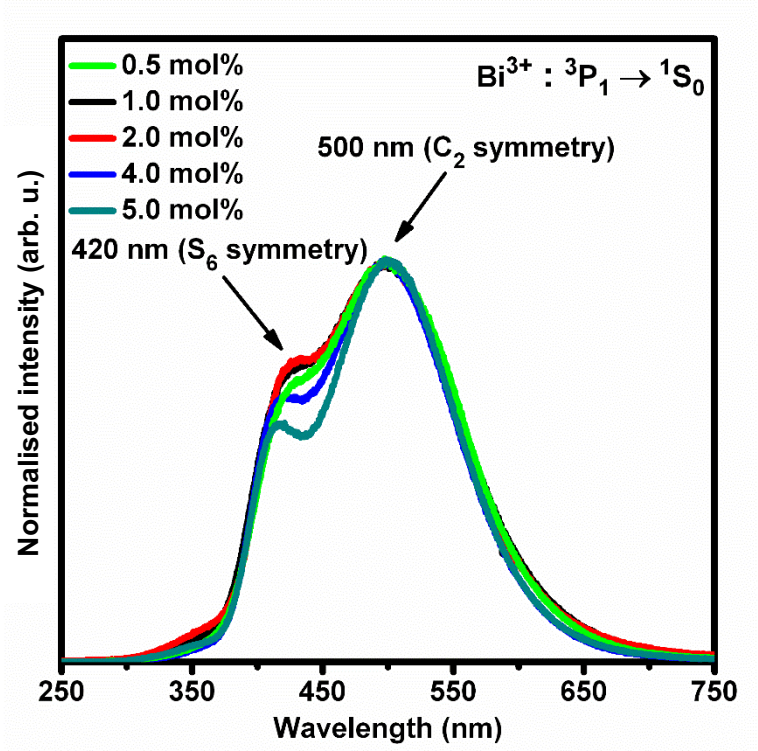

Figure 5.11: Normalised CL spectrum of $Y_{2-x}O_3:Bi_x$ (x = 0.5, 1.0, 2.0, 4.0, 5.0 mol%) phosphor powder.

Figure 5.11 shows the CL spectra of the Y_2O_3:Bi_x (x = 0.5, 1.0, 2.0, 4.0, 5.0 mol%) normalised at 500 nm. With an increase in Bi^{3+} concentration an increase in the emission intensity originating from the S_6 site was observed until a maximum at 2.0 mol% and decreased with a further increase in the Bi^{3+} concentration. The results obtained from the CL spectra showed a similar trend and correlated well with the results shown in Figure 5.10.

5.4 Conclusion

By varying the molar concentration of Bi^{3+} (x = 0.5, 1.0, 2.0, 4.0 and 5.0 mol%) in the Y_2O_3 host matrix, the phosphors were successfully synthesised using the co-precipitation method at a constant pH 10. The XRD patterns confirmed that the phosphor material crystallised as a single phase cubic structure and that the crystallite size remained fairly consistent ranging between 44 nm to 50 nm. Using XPS and EDS characterisation techniques the elemental composition and states were acquired and found to be well distributed within the sample. The PL results showed that the emission intensity was maximised at Y_2O_3:$Bi_{2.0\ mol\%}$ and further increase in the Bi^{3+} concentration lead to luminescence quenching.

5.5 References

[1] R. J. D. Tilley, "Understanding Solids The Science of Materials", *John Wiley & Sons Ltd, The Atrium, Southern Gate, Chichester, West Sussex, England*, (2004)

[2] U. Rambabu, S. Do Han, "Broad band down conversion from ultra violet light to near infrared emission in YVO_4:Bi^{3+},Yb^{3+} as spectral conversion phosphor for c-Si solar cells", *Ceram. Int.*, **39,** 1603–1612 (2013)

[3] L. G. Jacobsohn, M. W. Blair, S. C. Tornga, L. O. Brown, B. L. Bennett, R. E. Muenchausen, "Y_2O_3:Bi nanophosphor: Solution combustion synthesis, structure, and luminescence", *J. Appl. Phys.*, **104,** 124303–7 (2008)

[4] X. Y. Huang, X. H. Ji, Q. Y. Zhang, "Broadband downconversion of ultraviolet light to near-infrared emission in Bi^{3+}-Yb^{3+}-codoped Y_2O_3 phosphors", *J. Am. Ceram. Soc.*, **94,** 833–837 (2011)

[5] F. Réal, B. Ordejón, V. Vallet, J. P. Flament, J. Schamps, "Improvement of the ab initio embedded cluster method for luminescence properties of doped materials by taking into account impurity induced distortions: The example of Y_2O_3:Bi^{3+}", *J. Chem. Phys.*, **131,** 194501 1-17 (2009)

[6] E. Nakazawa, "Fundamentals of luminescence", *in Fundamentals of Phosphors* (eds. Yen, W. M., Shionoya, S. & Yamamoto, H.) , Chapt. 1 Sec. 1, 1–9 *CRC Press, Taylor and Francis Group, Boca Raton, Florida*, (2007)

[7] E. Nakazawa, "Fundamentals of luminescence", *in Fundamentals of Phosphors* (eds. Yen, W. M., Shionoya, S. & Yamamoto, H.) , Chapt. 1 Sec. 8, 89–96 *CRC Press, Taylor and Francis Group, Boca Raton, Florida*, (2007)

[8] R. C. Ropp, "Design of Phosphors", *in Luminescence and the Solid State vol. 21* , Chapt. 6 447–614 *Elsevier B.V., Amsterdam, The Netherlands*, (2004)

[9] R. D. Shannon, "Revised effective ionic radii and systematic studies of interatomic distances in halides and chalcogenides", *Acta Crystallogr. Sect. A*, **32,** 751–767 (1976).

[10] J. F. Moulder, W. F. Stickle, P. E. Sobol, K. D. Bomben, "Handbook of X-ray Photoelectron spectroscopy", *ULVAC-PHI, Inc. Japan and Physical Electronics USA, Inc. USA*, (1992)

[11] T. Gougousi, Z. Chen, "Deposition of yttrium oxide thin films in supercritical carbon dioxide", *Thin Solid Films*, **516,** 6197–6204 (2008)

[12] Y. Uwamino, T. Ishizuka, H. Yamatera, "X-ray photoelectron spectroscopy of rare-earth compounds", *J. Electron Spectros. Relat. Phenomena*, **34,** 67–78 (1948)

[13] J. F. Watts, J. Wolstenholme, "An Introduction to Surface Analysis by XPS and AES", *John Wiley & Sons, Ltd, Chichester, UK*, (2003)

[14] Z. I. Mitrovic, M. Althobaiti, A. D. Weerakkody, V. R. Dhanak, W. M. Linhart, T. D. Veal, N. Sedghi, S. Hall, P. R. Chalker, D. Tsoutsou, A. Dimoulas, "Ge interface engineering using ultra-thin La_2O_3 and Y_2O_3 films : A study into the effect of deposition temperature", *J. Appl. Phys.*, **115,** 114102 1-16 (2014)

[15] J. F. Moulder, W. F. Stickle, P. E. Sobol, K. D. Bomben, "Handbook of X-ray Photoelectron spectroscopy", *ULVAC-PHI, Inc. Japan and Physical Electronics USA, Inc. USA*, (1992)

Chapter 6: The luminescence properties of Y_2O_3 co-doped Bi^{3+} and Yb^{3+} phosphor

This chapter focuses on the addition of a second dopant Yb^{3+}, that was introduced to the Y_2O_3:Bi^{3+} phosphor material. The visible PL spectra showed a decrease in the luminescence emission intensity with an increase in the Yb^{3+} ion concentration suggesting possible energy transfer between the Bi^{3+} and Yb^{3+} ion. The infrared PL spectra revealed that the infrared emission intensity began to decrease with a Yb^{3+} ion concentration greater than 10 mol%.

6.1 Introduction

Inorganic phosphor materials doped with rare-earth ions have gained much attention especially by the lighting industry due to their numerous possible emission wavelengths [1]. In recent years, phosphor materials have been used in conjunction with silicon based solar cells to improve its efficiency [2,3]. The main factor limiting the efficiency of solar cells is due to the spectral mismatch between the solar spectrum and the absorption spectrum of the solar cell [4]. When a solar cell absorbs a photon with an energy higher than its band gap, thermalisation of charge carriers are induced (see section 2.4.1). A method to reduce the thermalisation process is to use a phosphor material that can convert a high energy photon into two low energy photons which can be more efficiently absorbed by the solar cell [5,6]. The process of generating two low energy photons from one high energy photon is called down-conversion [2]. Ytterbium in its +3 oxidation state has shown great potential in enhancing the efficiency of crystalline silicon solar cells. Yb^{3+} consists of only two energy states: a $^2F_{7/2}$ ground state and an excited $^2F_{5/2}$ state. The two states are separated by a wavenumber of approximately 10 000 cm^{-1} resulting in an emission wavelength of roughly 1000 nm which correlates well with the maximum absorption spectra of crystalline silicon [7,8].

Wei et al. studied the effect of Bi^{3+} and Yb^{3+}concentration on the luminescence properties and quantum efficiency in Y_2O_3 [9]. Their experiment showed that concentration quenching of Yb^{3+} posed a serious problem and were able to obtain a quantum efficiency of only 18.9% for a sample containing 12 % Yb^{3+} ions. They did, however, demonstrate that a Bi^{3+} ion was capable of transferring its energy to two neighbouring Yb^{3+} ions through the cooperative energy transfer (CET) process. Huang et al. showed that the maximum theoretical quantum efficiency

of Yb^{3+} can be calculated by observing the visible luminescence decay curve of Bi^{3+} [10]. The upper limit of the total quantum efficiency was found to be 173.8 % for a sample containing 20 % Yb^{3+}, by ignoring any non-radiative effects. The actual quantum efficiency for the near-infrared emission would be, however, much lower due to the effects of concentration quenching.

In this chapter, we will investigate the transition of Yb^{3+} under UV excitation. The effect of Yb^{3+} ion concentration on both the visible Bi^{3+} emission and infrared Yb^{3+} emission intensity will be studied. The structural characterisation will be achieved using XRD, the chemical composition will be obtained using EDS and finally the luminescence properties will be gathered using PL and CL spectroscopy.

6.2 Experimental procedure

The $Y_2O_3:Bi^{3+},Yb^{3+}$ phosphor powders were prepared using the co-precipitation method discussed in Section 3.2.1. Both the pH and Bi^{3+} concentration was kept constant at 10 and 2.0 mol%, respectively, while the Yb^{3+} concentration was varied (x = 2.0, 4.0, 6.0, 10.0, 20.0 and 40.0 mol%), to study its effect on the visible and infrared emission on the phosphor material.

The phase structure was characterised from the XRD spectrum using a Bruker D8 Advance diffractometer with KαCu X-ray (1.54Å). The particle morphology, chemical composition and luminescence were captured and measured using a Jeol JSM-7800F Field Emission SEM equipped with an Oxford Artic EDS and a Gatan Mono CL4. The excitation and emission properties were measured using a Varian Cary Eclipse fluorescence spectrometer equipped with a xenon lamp. The quantum efficiency measurements were measured using a Edinburgh Instruments FLS980 spectrometer equipped with a xenon lamp and an integrating sphere.

6.3 Results and discussion

6.3.1. Structural analysis

The XRD pattern for $Y_{2-x}O_3$:$Bi_{2.0\ mol\%}$,Yb_x phosphor powder prepared at varying Yb^{3+} ion concentrations while keeping the pH and Bi concentration during synthesis constant at pH =10 and Bi^{3+} = 2.0 mol% is shown in Figure 6.1. The XRD pattern for the prepared phosphor materials were a good match to the reference JCPDS 01-083-0927 data. This indicated that the phosphor materials formed in a single phase cubic crystal structure belonging to the Ia-3 space group.

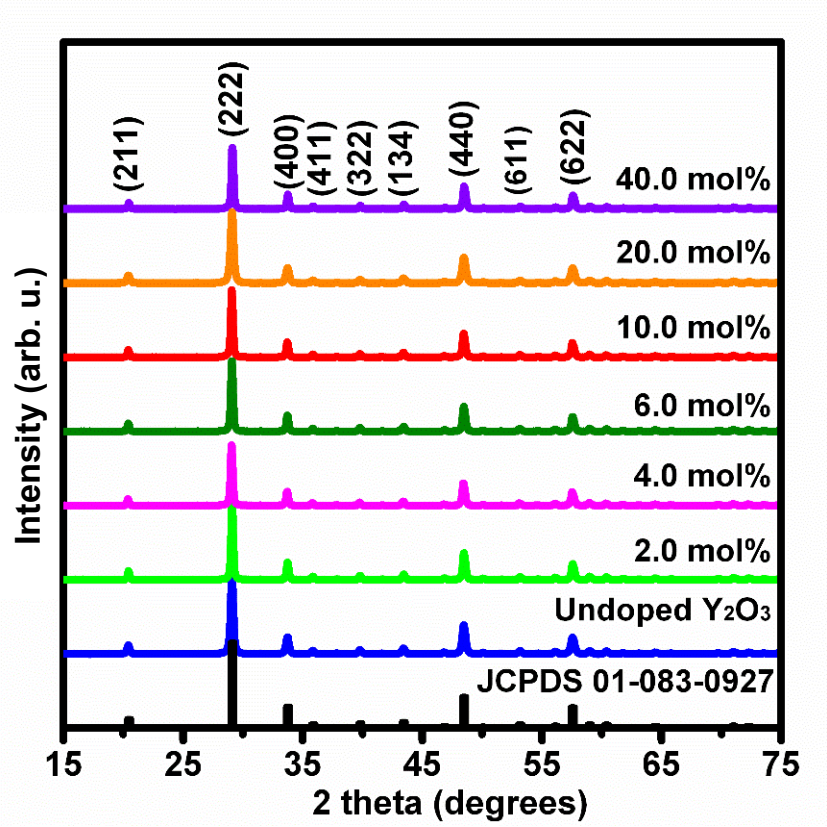

Figure 6.1: XRD pattern for $Y_{2-x}O_3$:$Bi_{2.0\ mol\%}$,$Yb_{x\ mol\%}$ phosphor synthesised at varying Yb^{3+} concentration while keeping the pH and Bi^{3+} concentration constant.

With an increase in the Yb^{3+} ion concentration a slight shift in the XRD reflections to higher Bragg angles were observed. These shifts were due to lattice distortions caused by the difference in the ionic radius of Y^{3+} (0.090 nm) host ion and the Yb^{3+} (0.087 nm) dopant ion [11]. By using all the Miller indexes indicated in Figure 6.1, the lattice parameter of both the

undoped and doped materials were calculated using the Bragg expression (equation 4.1 and 4.2) and were tabulated in

Table 6.1. Aside from peak shifting, slight variations in the peak widths were observed with an increase in Yb^{3+} concentration. Because all the samples were analysed under the same environmental conditions and using the same system parameters, changes in their FWHM were due to changes in their crystallite size as well as the strain present in the lattice. The crystallite size and lattice strain were obtained using the Williamson-Hall plot (equation 5.1), shown in Figure 6.2 and the results were tabulated in

Table 6.1.

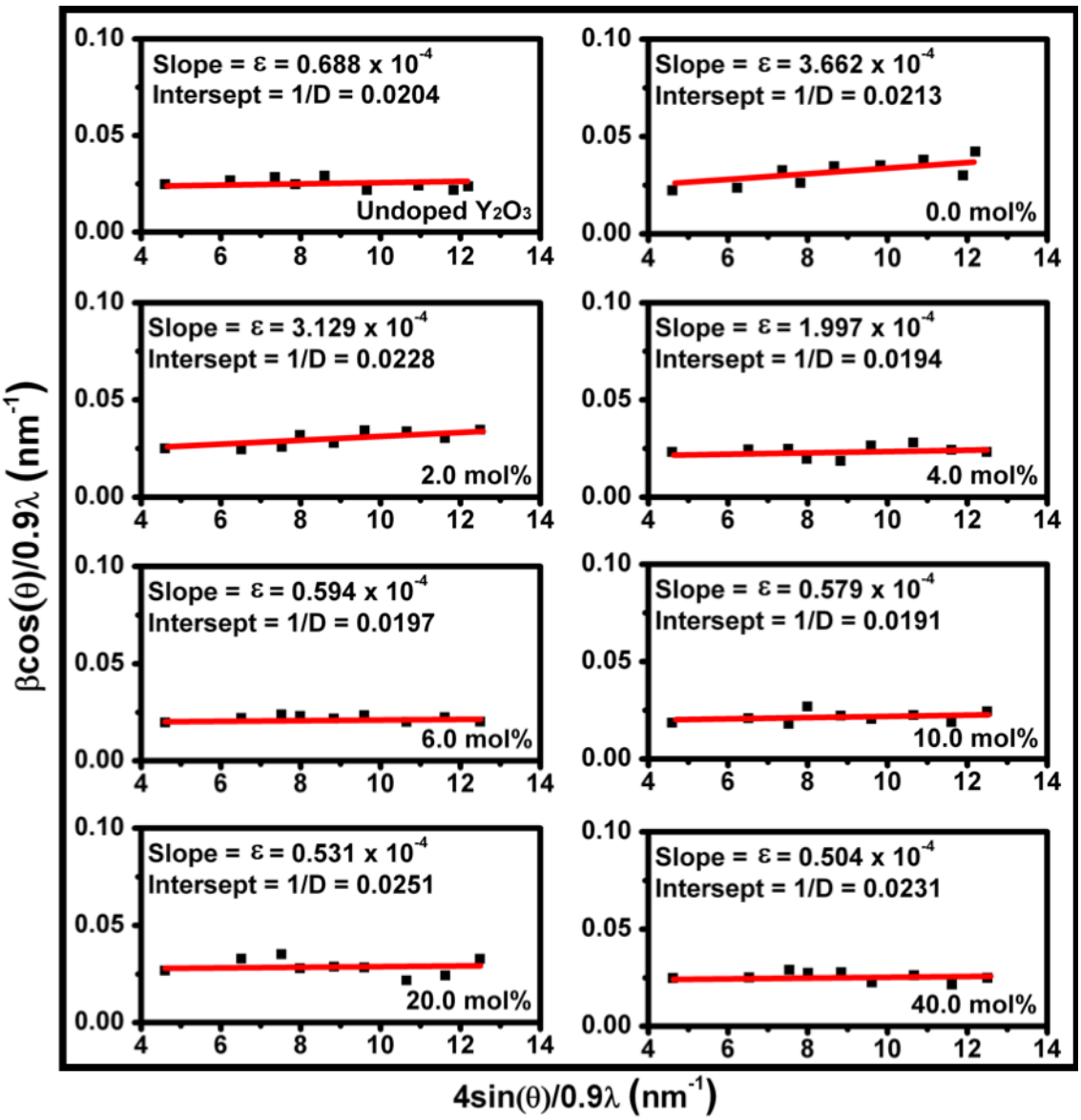

Figure 6.2: Williamson-Hall plot of undoped Y_2O_3 and $Y_{2-x}O_3$:$Bi_{2.0\ mol\%}$,$Yb_{x\ mol\%}$ synthesised at different Yb^{3+} concentrations.

Table 6.1: Structural parameters both undoped Y_2O_3, Y_2O_3:$Bi_{2.0\ mol\%}$ and Y_2O_3:$Bi_{2.0\ mol\%}$,$Yb_{x\ mol\%}$ synthesised at varying Yb^{3+} ion concentration (JCPDS lattice parameter a = 10.60 Å).

Sample	Lattice parameter a (Å)	Crystallite size D (nm)	Micro-strain ε (x 10^{-4})
Undoped Y_2O_3	10.61	49 ± 5	0.688
Y_2O_3:$Bi_{2.0\ mol\%}$,$Yb_{0.0\ mol\%}$	10.63	47 ± 6	3.662
Y_2O_3:$Bi_{2.0\ mol\%}$,$Yb_{2.0\ mol\%}$	10.64	44 ± 8	3.129
Y_2O_3:$Bi_{2.0\ mol\%}$,$Yb_{4.0\ mol\%}$	10.63	51 ± 9	1.997
Y_2O_3:$Bi_{2.0\ mol\%}$,$Yb_{6.0\ mol\%}$	10.62	50 ± 6	0.594
Y_2O_3:$Bi_{2.0\ mol\%}$,$Yb_{10.0\ mol\%}$	10.62	48 ± 5	0.579
Y_2O_3:$Bi_{2.0\ mol\%}$,$Yb_{20.0\ mol\%}$	10.61	49 ± 8	0.531
Y_2O_3:$Bi_{2.0\ mol\%}$,$Yb_{40.0\ mol\%}$	10.60	46 ± 6	0.504

With an increase in Yb^{3+} concentration a small decrease in the lattice parameter was observed which was expected due to the ionic radius of the Yb^{3+} ion being smaller than that of the Y^{3+} ion. The crystallite size, however, remained fairly constant with an increase in Yb^{3+} concentration due to the crystallite size being more sensitive to the changes in pH (section 5.3.1) rather than changes in dopant concentration.

6.3.2. Compositional analysis

EDS was used in order to investigate the elemental composition of Y_2O_3:$Bi_{2.0\ mol\%}$,Yb_x (x = 4.0, 10.0, and 20.0 mol%) phosphor powders shown in Figure 6.3 – 6.5. The spectrum confirmed the Y, O, Bi and Yb were present in the sample as expected. The presence of carbon was also detected which probably came from the carbon tape on which the samples were mounted or from atmospheric hydrocarbons that were introduced to the sample during synthesis and due to atmospheric handling. In addition to the EDS spectrum, an elemental map showing the distribution of the elements were also collected. From the map, it can be seen that all the elements present within the phosphor material were evenly distributed over the sample.

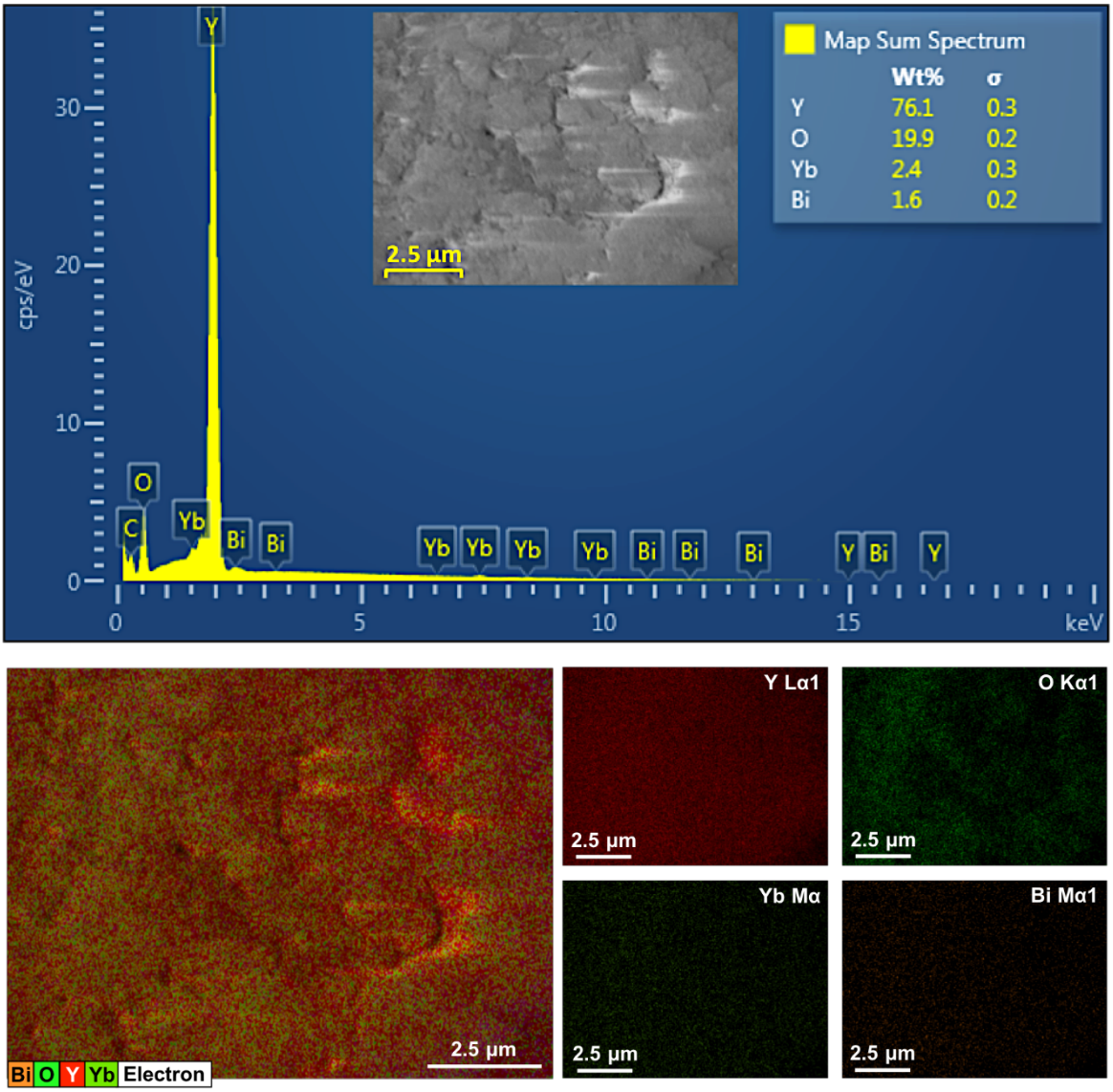

Figure 6.3: EDS spectrum and elemental mapping of Y_2O_3:$Bi_{2.0\ mol\%}$,$Yb_{4.0\ mol\%}$ powder phosphor.

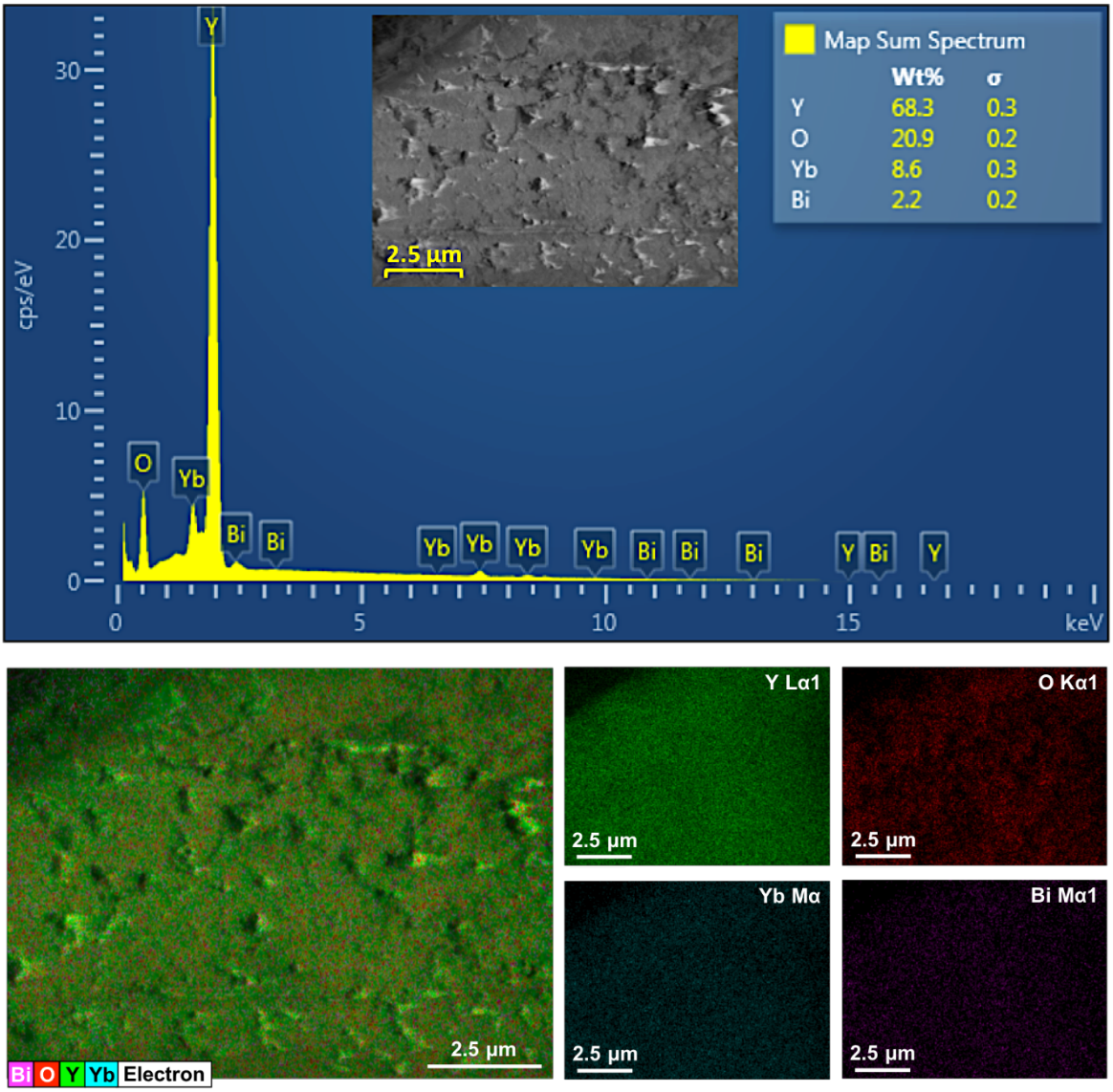

Figure 6.4: EDS spectrum and elemental mapping of Y_2O_3:$Bi_{2.0\ mol\%}$,$Yb_{10.0\ mol\%}$ powder phosphor.

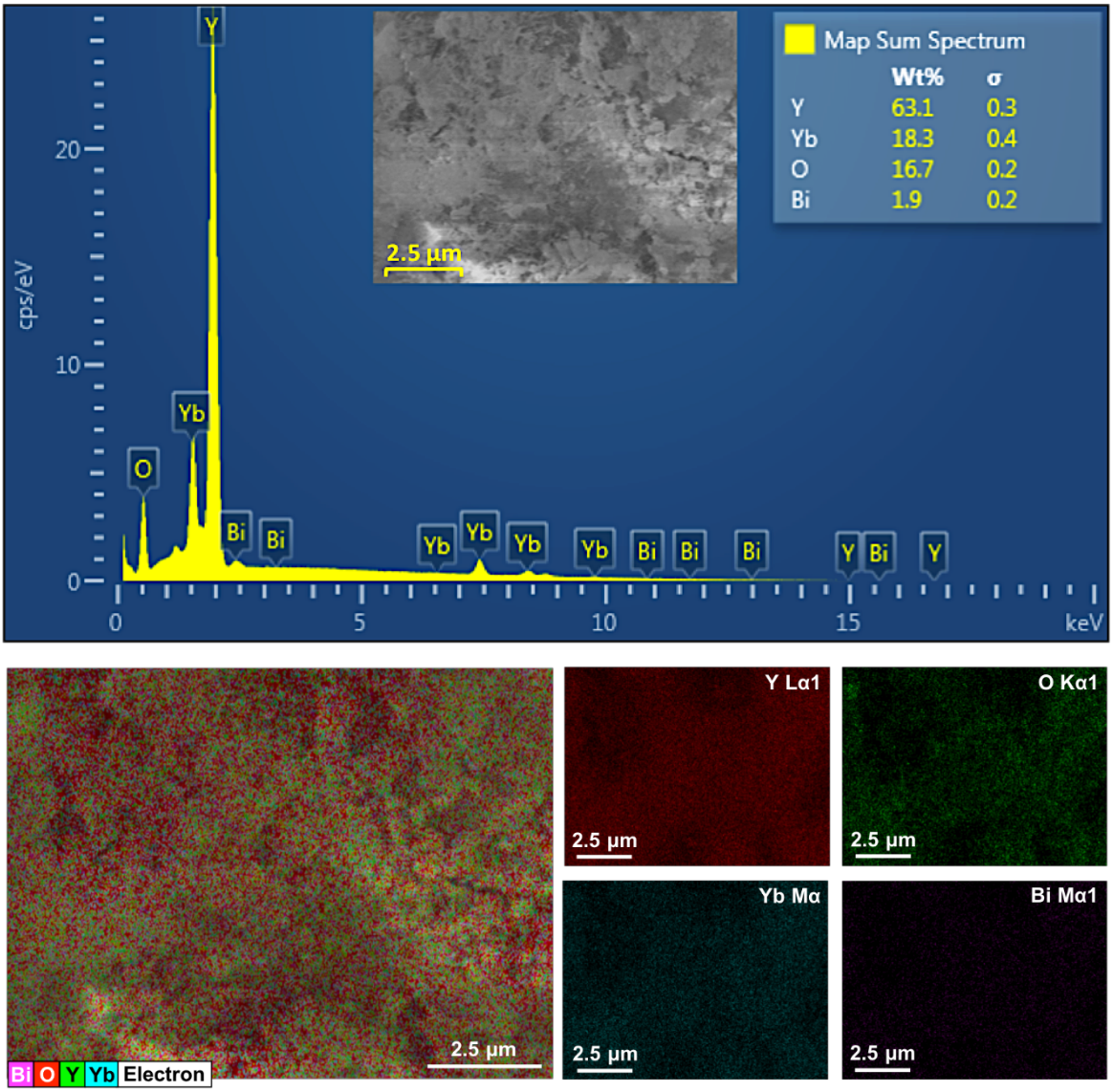

Figure 6.5: EDS spectrum and elemental mapping of Y_2O_3:$Bi_{2.0\ mol\%}$,$Yb_{20.0\ mol\%}$ powder phosphor synthesised at pH 10.

6.3.3. Luminescence properties

The visible emission spectrum of Y_2O_3:$Bi_{2.0\ mol\%}$,$Yb_{2.0\ mol\%}$ under 325 nm excitation is shown in Figure 6.6. The emission spectrum consists of a broad predominant peak centred at 495 nm which was assigned to the $^1S_0 \rightarrow {}^3P_1$ Bi^{3+} transition [12,13]. Figure 6.6 depicts the effect of Yb^{3+} concentration on the luminescence intensity of the Y_2O_3:$Bi_{2.0\ mol\%}$,Yb_x (x= 2.0, 4.0, 6.0, 10.0, 20.0 and 40.0 mol%) under the same 325 nm excitation. With an increase Yb^{3+} concentration a decrease in the visible Bi^{3+} emission intensity was observed. The quenching of

the Bi^{3+} emission was attributed to the possible energy transfer from the Bi^{3+} ions to the Yb^{3+} ions.

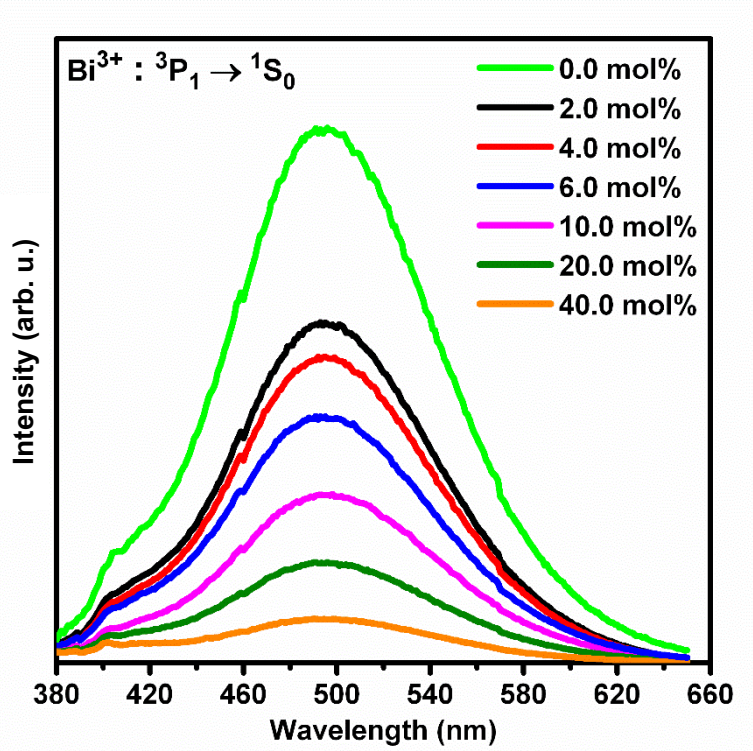

Figure 6.6: Visible emission spectra of Y_2O_3:$Bi_{2.0\ mol\%}$;Yb_x (x = 0.0, 2.0, 4.0, 6.0, 10.0, 20.0, 40.0 mol%) excited at 325 nm.

Figure 6.7 shows the visible luminescence lifetime of the C_2 and S_6 site that Bi^{3+} ions occupy within the Y_2O_3 host. The results show that the S_6 site has a significantly lower lifetime with $\tau(S_6) = 0.785$ µs than the C_2 site where the lifetime is $\tau(C_2) = 1.241$ µs which was also reported by Scarangella et al [14]. By looking at the decay between 0.0 and 1.0 µs, a slight increase in the intensity of the S_6 site was observed. The increase in intensity is due to the slight overlap between the C_2 site emission spectrum and the S_6 site excitation (shown in Figure 5.9). Thus, a small amount of energy emitted the C_2 site during its decay is transferred to the S_6 site leading to a slight increase in its intensity before the S_6 site finally decays.

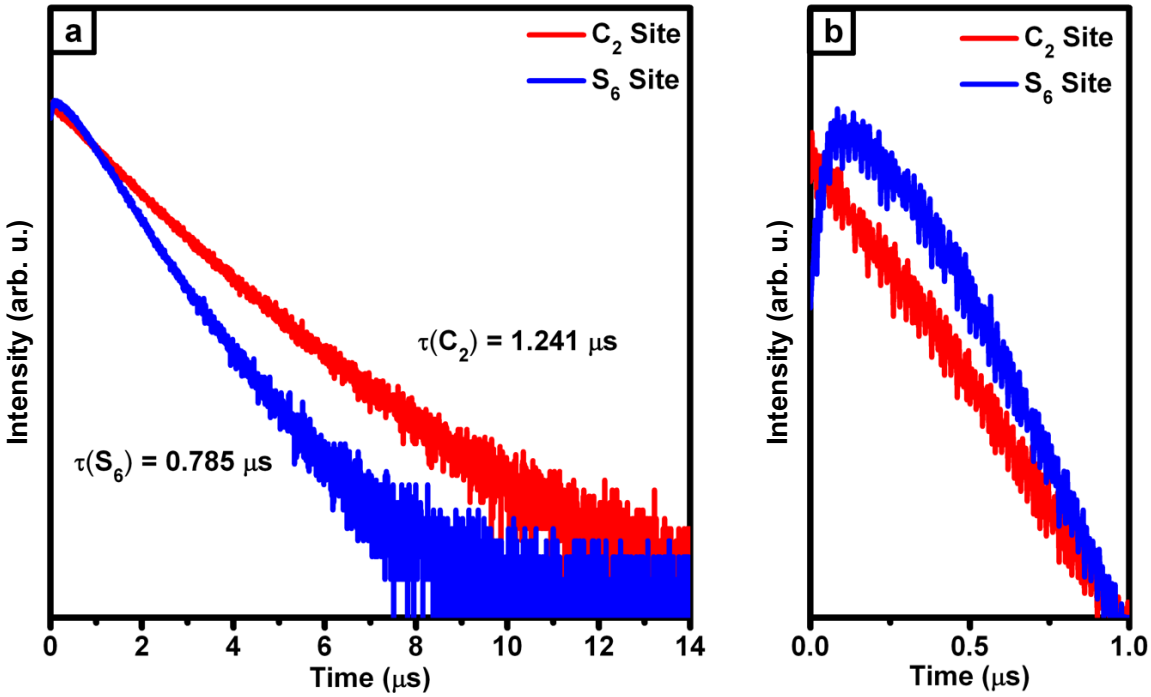

Figure 6.7: (a) Decay lifetime (under 355 nm YAG laser excitation) for the C_2 and S_6 site that Bi^{3+} ions occupy in the Y_2O_3:$Bi_{2.0\ mol\%}$,$Yb_{10.0\ mol\%}$ phosphor powder. (b) Zoomed image showing the first 1.0 μs of decay.

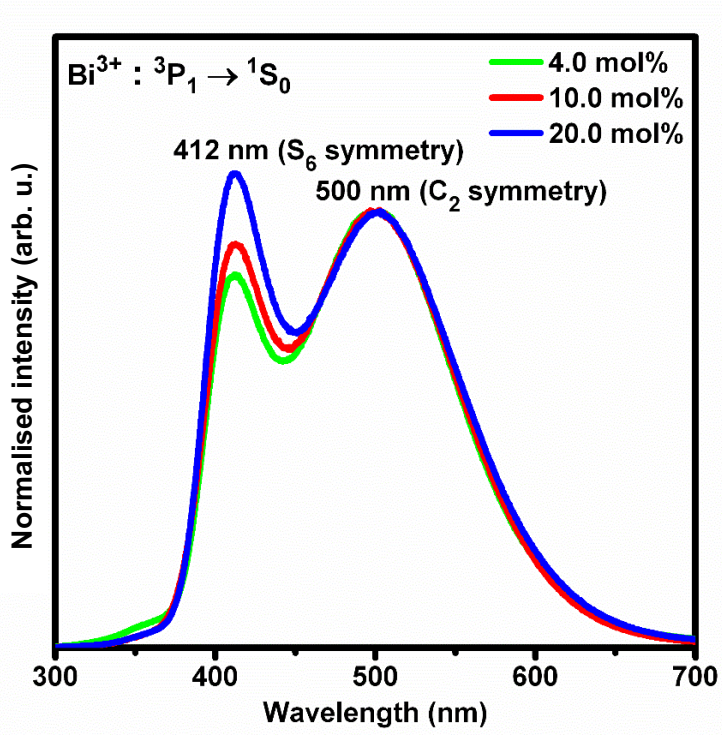

Figure 6.8: Normalised CL spectrum of Y_2O_3:$Bi_{2.0\ mol\%}$,Yb_x (x = 4.0, 10.0 and 20.0 mol%) phosphor powder

Figure 6.8 shows the CL of Y_2O_3:$Bi_{2.0\ mol\%}$,Yb_x (x = 4.0, 10.0 and 20.0 mol%) normalised at 500 nm. With an increase in the Yb^{3+} concentration an increase in the 410 nm (S_6 symmetry) emission of Bi^{3+} was observed. This result can be attributed to different factors: (1) an increase in Yb^{3+} concentration forces the Bi^{3+} ions to occupy the S_6 symmetry of the host lattice therefore decreasing the 500 nm emission intensity while increasing the 412 nm emission of Bi^{3+}, and/or (2) the 500 nm (C_2 symmetry) emission of Bi^{3+} was better utilised by the Yb^{3+} ions causing its intensity to decrease.

In order to determine whether Bi^{3+} helps in enhancing the infrared emission of Yb^{3+} two samples were prepared one with and another without the presence of bismuth. Figure 6.9 shows the infrared emission of Y_2O_3:$Yb_{2.0\ mol\%}$ and Y_2O_3:$Bi_{2.0\ mol\%}$,$Yb_{2.0\ mol\%}$ which were both prepared and measured under the same conditions.

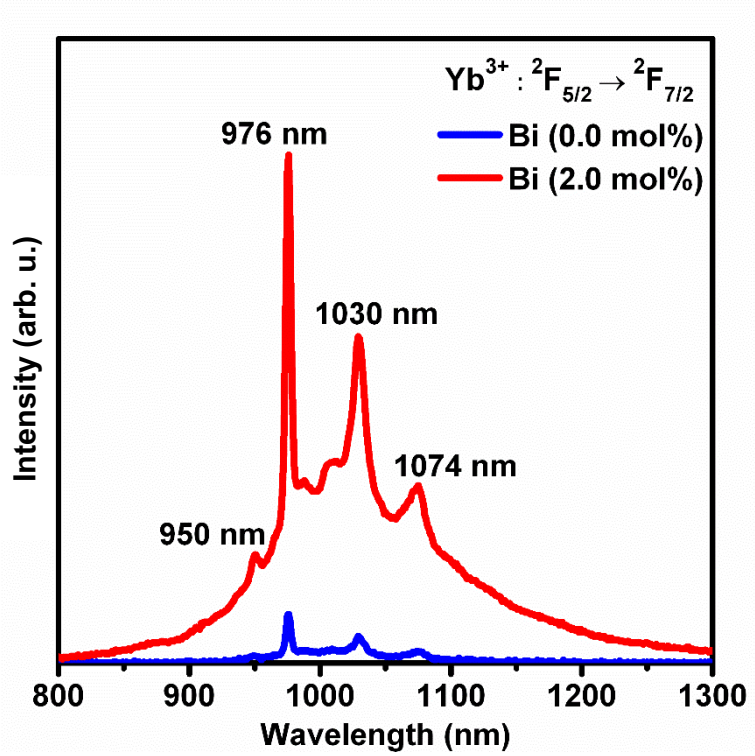

Figure 6.9: Infrared emission of Y_2O_3:$Yb_{2.0\ mol\%}$ and Y_2O_3:$Bi_{2.0\ mol\%}$,$Yb_{2.0\ mol\%}$ excited using a 325 nm He-Cd laser.

The spectrum shows a broad infrared emission band originating from the $^2F_{5/2} \rightarrow {}^2F_{7/2}$ transition of Yb^{3+} [12,15]. The Yb^{3+} emission consists of a sharp maximum centred at 976 nm accompanied by several weaker peaks centred at 950 nm, 1030 nm and 1074 nm caused by the

crystal field Stark splitting of the $^2F_{5/2}$ and $^2F_{7/2}$ energy levels [16]. With the addition of Bi^{3+} a strong increase in the infrared emission was observed, which indicates that Bi^{3+} plays a significant role in assisting Yb^{3+} to better utilise the 325 nm UV radiation. Figure 6.10 shows the effect of Yb^{3+} concentration on the infrared emission intensity of $Y_2O_3:Bi_{2.0\ mol\%},Yb_x$ (x= 2.0, 4.0, 6.0, 10.0, 20.0 and 40.0 mol%) phosphor material.

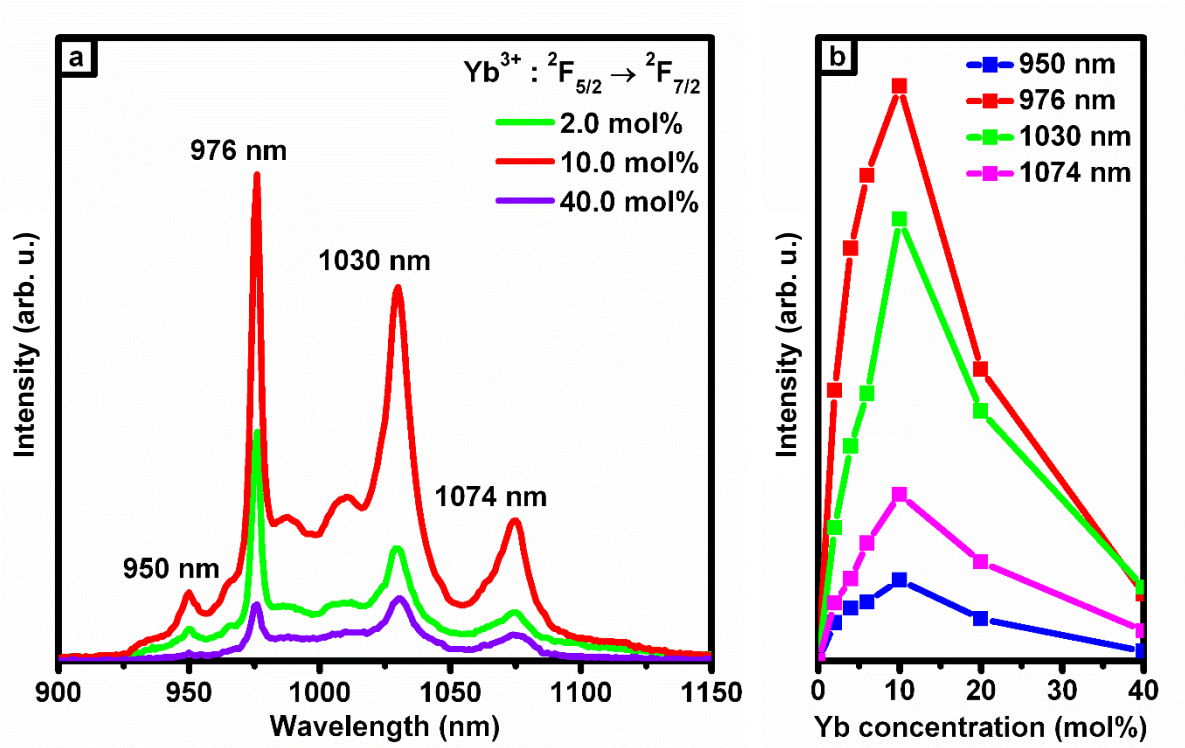

Figure 6.10: (a) Infrared emission of $Y_2O_3:Bi_{2.0\ mol\%},Yb_x$ (x = 2.0, 10.0, and 40.0 mol%) under 325 nm excitation. (b) Infrared luminescence intensity as a function of Yb concentration of the 950 nm, 976 nm, 1030 nm, and 1074 nm emission.

With an increase in Yb^{3+} concentration an increase in the infrared emission intensity was observed. At 10 mol% of Yb^{3+} the maximum infrared emission intensity was observed, thereafter the emission intensity decreased due to the effect of concentration quenching where cross relaxation between the Yb^{3+} ions decreased the luminescence yield [17]. Additionally, changes in the relative intensities of the four predominant peaks (950, 976, 1030 and 1074 nm peaks) were observed and shown in Table 6.2.

Table 6.2: Calculated intensity ratio between the 950 nm , 1030 nm and 1074 nm compared to the 976 nm emission as a function of Yb concentration.

Yb^{3+} concentration (mol%)	Intensity ratio (950 nm/ 976 nm)	Intensity ratio (1030 nm/ 976 nm)	Intensity ratio (1074 nm/ 976 nm)
2.0	0.141	0.491	0.241
4.0	0.128	0.521	0.199
6.0	0.116	0.592	0.185
10.0	0.142	0.772	0.291
20.0	0.144	0.856	0.341
40.0	0.145	1.110	0.452

From the results shown in Table 6.2 it was observed that the relative intensities of the Yb^{3+} emission peaks did not remain constant but rather changed with an increase in Yb^{3+} concentration. When the Yb^{3+} concentration was increased an increase in the intensity ratio between the 1030 and 976 nm emission was seen, while for the 950 nm and 1074 nm emissions their intensity ratio with respect to the 976 nm emission initially decreased with an increase in Yb^{3+} concentration and then increased with a further increase in the ion concentration.

The quantum efficiency of the Y_2O_3:$Bi_{2.0\ mol\%}$,$Yb_{10.0\ mol\%}$ phosphor material was determined using an integrating sphere (section 4.3). Because two detectors (visible and infrared detector) were required to determine the quantum efficiency of the phosphor material a correction factor was needed in order to correct the sensitivity factor of the two detectors. To obtain the correction factor the first procedure was to find a wavelength region where both detectors were able to detect. The visible detector had a maximum detection limit of 900 nm while the infrared detector was able to detect emissions above 800 nm thus both detectors were set to measure a $BaSO_4$ reference sample between 800 to 900 nm, shown in Figure 6.11.

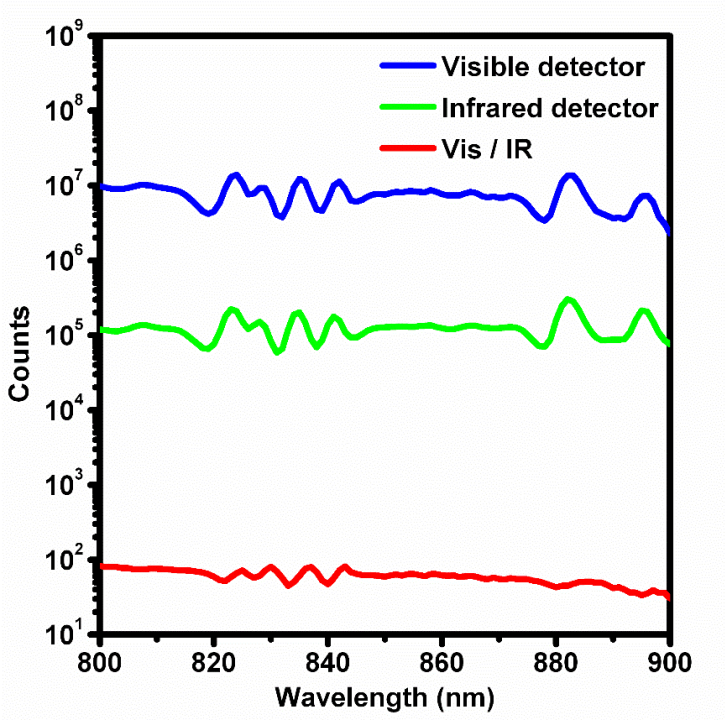

Figure 6.11: Emission spectra of $BaSO_4$ obtained using the visible detector and infrared detector.

The results showed that the visible detector had a signal that was two orders of magnitude stronger than the infrared detector. Thus, by dividing the spectrum obtained from the visible detector by the spectrum acquired from the infrared detector and then taking the average the correction factor for the infrared detector was obtained.

By using the integrating sphere a combined reflectance and emission spectra of a $BaSO_4$ reference material along with the Y_2O_3:$Bi_{2.0\ mol\%}$,$Yb_{10.0\ mol\%}$ phosphor material that was used to determine the quantum efficiency of the phosphor material were obtained and are shown in Figure 6.12.

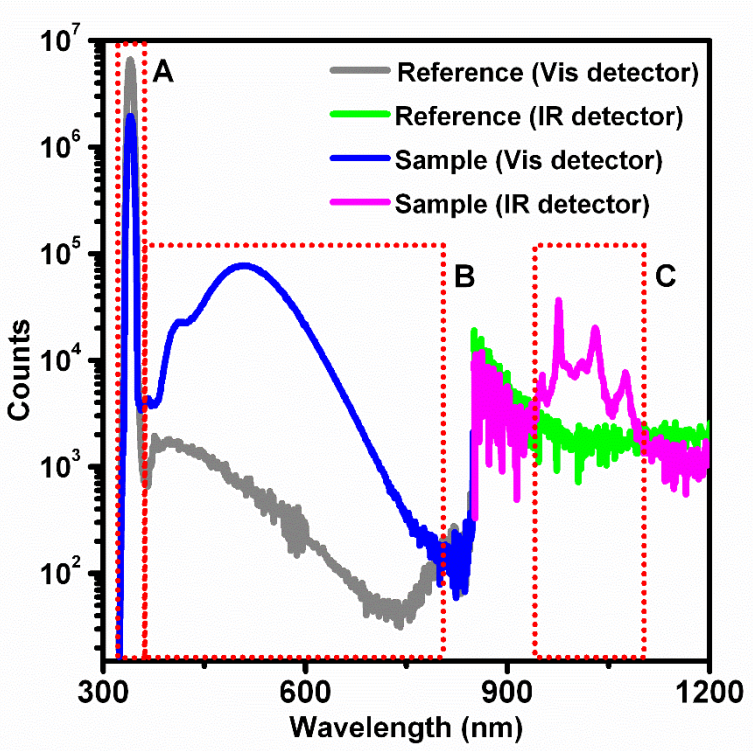

Figure 6.12: Quantum efficiency spectrum of Y_2O_3:$Bi_{2.0\ mol\%}$,$Yb_{10.0\ mol\%}$ phosphor material measured using a 325 nm excitation source.

The quantum efficiency of the Y_2O_3:$Bi_{2.0\ mol\%}$,$Yb_{10.0\ mol\%}$ phosphor material was determined using the following equations,

$$\eta_{Bi} = \frac{S_B - R_B}{R_A - S_A} \tag{7.1}$$

$$\eta_{Yb} = \frac{S_C - R_C}{R_A - S_A} \tag{7.2}$$

where η_{Bi} and η_{Yb} are the quantum efficiencies of the Bi and Yb respectively, *S* represents the area beneath the emission spectrum of the prepared sample material and *R* represents the area beneath the emission spectrum of the reference sample. In order to determine the quantum efficiency of the Bi^{3+} and Yb^{3+} emissions separately the spectrum in Figure 6.12 was divided into three parts. Block A which encloses the reflected spectrum, block B the visible emission of Bi^{3+} and finally block C the infrared emission of Yb^{3+}. The quantum efficiency of the visible Bi^{3+} emission was found to be 24 % while the infrared Yb^{3+} emission was only 2 %.

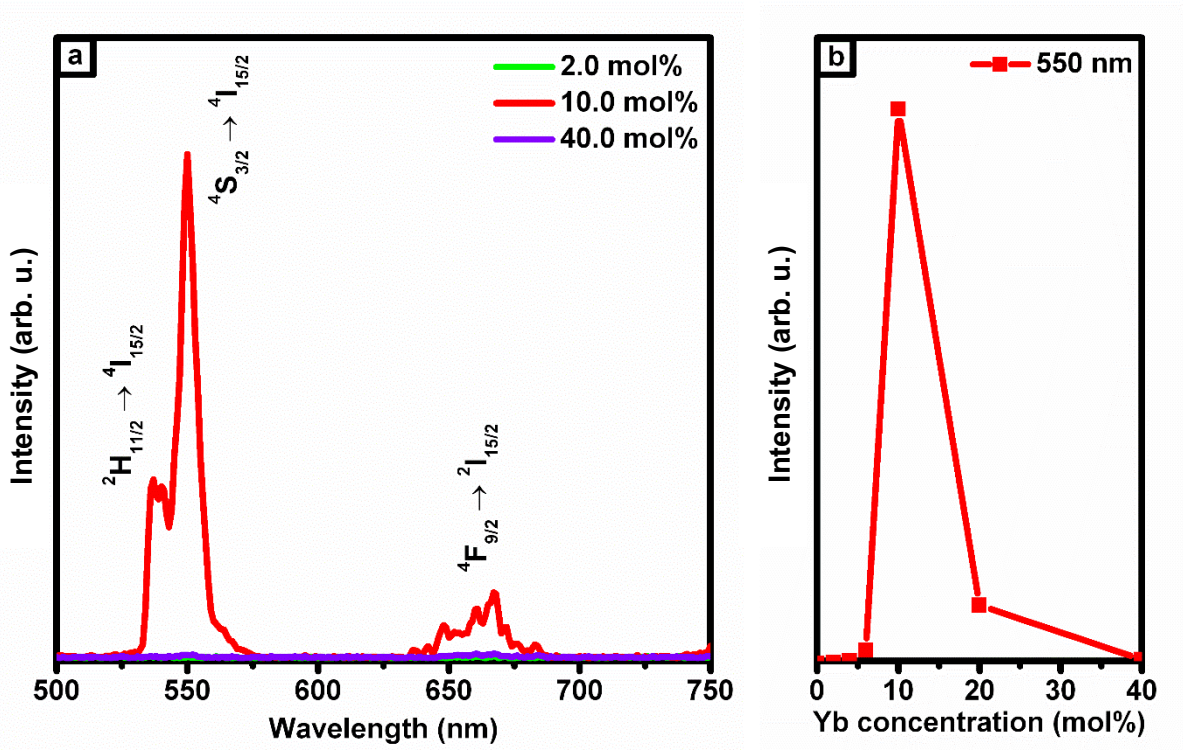

Figure 6.13: (a) Visible emission of Y_2O_3:$Bi_{2.0\ mol\%}$,$Yb_{x\ mol\%}$ under 980 nm infrared excitation. (b) 550 nm emission intensity as a function of Yb concentration.

In order to study whether the Y_2O_3:$Bi_{2.0\ mol\%}$,$Yb_{x\ mol\%}$ had up-conversion properties, the phosphor materials were excited at 980 nm. Under 980 nm excitation a strong green emission centred at around 550 nm was observed for the 10 mol% Yb sample. The luminescence spectrum, shown in Figure 6.12, was, however, not related to the Bi^{3+} emission as it has an emission centred at 500 nm but rather an emission related to the Er^{3+} ion [18]. The Er^{3+} impurities were introduced through the Yb_2O_3 starting material as it is chemically difficult to separate rare-earth elements from each other in order to produce a pure substance [18,19].

6.4 Conclusion

The XRD results showed that the Y_2O_3:$Bi_{2.0\ mol\%}$,Yb_x (x = 2.0, 4.0, 6.0, 10.0, 20.0, 40.0 mol%) phosphor material was successfully synthesised using the co-precipitation method. All the prepared samples crystallised as a single phase cubic structure with a Ia-3 space group. The crystallite was calculated using the XRD peaks and found to vary from 44 nm to 51 nm. With an increase in Yb^{3+} concentration the visible emission intensity of Bi^{3+} decreased suggesting possible energy transfer between the two ions. The lifetime measurements show that the S_6 site has a significantly lower lifetime than the C_2 site. The energy transfer process was confirmed

when the Y_2O_3:$Bi_{2.0\ mol\%}$,$Yb_{2.0\ mol\%}$ sample had significantly stronger IR emission in comparison with that of the Y_2O_3:$Yb_{2.0\ mol\%}$ sample, which contained no Bi. The strongest infrared luminescence intensity was achieved from the Y_2O_3:$Bi_{2.0\ mol\%}$,$Yb_{10.0\ mol\%}$ sample. The quantum efficiency was, however, only 26 %. Thus, further optimisation of the phosphor material is required in order to improve on its efficiency. Using a 980 nm excitation source a green emission was detected which was related to the Er^{3+} impurities, which were present in the Yb_2O_3 starting material.

6.5 References

[1] R. M. Jafer, "Luminescence properties of Y_2O_3:Bi^{3+} as powder and thin film phosphor for solar cell application", MSc dissertation, *University of the Free State*, *South Africa*, (2015)

[2] T. Trupke, M. A. Green, P. Würfel, "Improving solar cell efficiencies by down-conversion of high-energy photons", *J. Appl. Phys.*, **92,** 1668–1674 (2002)

[3] T. Trupke, M. A. Green, P. Würfel, "Improving solar cell efficiencies by up-conversion of sub-band-gap light", *J. Appl. Phys.*, **92,** 4117–4122 (2002)

[4] B. S. Richards, "Luminescent layers for enhanced silicon solar cell performance: Down-conversion", *Sol. Energy Mater. Sol. Cells*, **90,** 1189–1207 (2006)

[5] U. Rambabu, S. Do Han, "Broad band down conversion from ultra violet light to near infrared emission in YVO_4:Bi^{3+}, Yb^{3+} as spectral conversion phosphor for c-Si solar cells", *Ceram. Int.*, **39,** 1603–1612 (2013)

[6] Q. Y. Zhang, X. Y. Huang, "Recent progress in quantum cutting phosphors", *Prog. Mater. Sci.*, **55,** 353–427 (2010)

[7] L. D. Deloach, S. A. Payne, L. L. Chase, L. K. Smith, W. L. Kway, W. F. Krupke, "Evaluation of Absorption and Emission Properties of Yb^{3+} Doped Crystals for Laser Applications", *IEEE J. Quantum Electron*, **29,** 1179–1191 (1993)

[8] L. Zhang, H. Hu, "Evaluation of spectroscopic properties of Yb^{3+} in tetraphosphate glass", *J. Non Cryst. Solids*, **292,** 108–114 (2001)

[9] X. Wei, S. Huang, Y. Chen, C. Guo, M. Yin, W. Xu, "Energy transfer mechanisms in Yb^{3+} doped YVO_4 near-infrared downconversion phosphor", *J. Appl. Phys.*, **107,** 2–7 (2010)

[10] X. Y. Huang, X. H. Ji, Q. Y. Zhang, "Broadband downconversion of ultraviolet light to near-infrared emission in Bi^{3+}-Yb^{3+}-codoped Y_2O_3 phosphors", *J. Am. Ceram. Soc.*, **94,** 833–837 (2011)

[11] R. D. Shannon, "Revised effective ionic radii and systematic studies of interatomic distances in halides and chalcogenides", *Acta Crystallogr. Sect. A*, **32,** 751–767 (1976)

[12] X. Y. Huang, Q. Y. Zhang, "Near-infrared quantum cutting via cooperative energy transfer in Gd_2O_3 : Bi^{3+} , Yb^{3+} phosphors", *Chin. Phys. B*, **19,** 3–6 (2010)

[13] L. G. Jacobsohn, M. W. Blair, S. C. Tornga, L. O. Brown, B. L. Bennett, R. E. Muenchausen, "Y_2O_3:Bi nanophosphor: Solution combustion synthesis, structure, and luminescence", *J. Appl. Phys.*, **104,** 124303–7 (2008)

[14] A. Scarangella, R. Reitano, G. Franzò, F. Priolo, "Efficient energy transfer from Bi to Er ions in Y_2O_3 thin films", *J. Lumin.*, **191,** 92–96 (2017)

[15] Z. Fang, R. Cao, F. Zhang, Z. Ma, G. Dong, J. Qiu, "Efficient spectral conversion from visible to near-infrared in transparent glass ceramics containing Ce^{3+} –Yb^{3+} codoped $Y_3Al_5O_{12}$ nanocrystals", *J. Mater. Chem. C*, **2,** 2204–2211 (2014)

[16] R. Simura, A. Jouini, J. H. Mun, A. Brenier, A. Yoshikawa, G. Boulon, T. Fukuda, "Growth and spectroscopic properties of Yb^{3+}-doped Sc_2O_3 crystals grown by the micro-pulling-down method", *Opt. Mater. (Amst).*, **30,** 18–21 (2007)

[17] O. Meza, L. A. Diaz-Torres, P. Salas, E. De la Rosa, C. Angeles-Chavez, D. Solis, "Cooperative Pair Driven Quenching of Yb^{3+} Emission in Nanocrystalline ZrO_2:Yb^{3+}.", *J. Nano Res.*, **5,** 121–134 (2009)

[18] Y. Jiang, X. Jiang, C. Chen, Y. Chen, X. Jiang, N. Tu, "Photoluminescence and electrical properties of Er^{3+}-doped $Na_{0.5}Bi_{4.5}Ti_4O_{15}$—$Bi_4Ti_3O_{12}$ inter-growth ferroelectric ceramics", *Front. Mater. Sci.*, **11,** 51–58 (2017)

[19] H. Royen, U. Fortkamp, "Rare Earth Elements-Purification, Separation and Recycling", *IVL Swedish Environment Research Institute*, *Stockholm*, *Sweden*, (2016)

Chapter 7: Analysis and comparison of $Y_2O_3:Bi^{3+},Yb^{3+}$ thin films synthesised by pulsed laser deposition and spin coating.

This chapter focuses on preparing $Y_2O_3:Bi_{2.0\ mol\%},Yb_{10.0\ mol\%}$ thin films using the PLD and spin coating techniques. In the PLD technique the films were grown in the presence of O_2 gas at various substrate temperatures. For the spin coating technique the number of coats and molarity of the $Y_2O_3:Bi_{2.0\ mol\%},Yb_{10.0\ mol\%}$ solution deposited onto the substrate were varied. The SEM images of the PLD prepared films showed that both the substrate temperature and deposition time played a major role in the surface morphology of the thin film. SEM images of the spin coating prepared thin films showed an overall smoother thin film as compared to the PLD films but, similar to the PLD technique, it is also dependant on several parameters such as the molarity and the number of coats that was applied to the substrate.

7.1 Introduction

One of the major factor influencing the low conversion efficiency of Si solar cells is due to the energy loss caused by thermalisation (section 2.4) after absorbing high energy photons. Researchers have been investigating the possibility of using luminescent materials to enhance the energy efficiency of Si solar cells [1]. These materials will act as spectral manipulators, shifting the wavelengths of the solar spectrum towards energies which can be better utilised by the solar cell. Many researchers have proposed the use of Yb^{3+} in combination with other rare earth or metal ions to produce phosphor materials with down-conversion or up-conversion properties. In the case of down-conversion Yb^{3+} ions paired with rare earth donor ions exhibit low and narrow UV absorption efficiencies due to its parity forbidden 4f-4f transitions resulting in a weak infrared emission from the Yb^{3+} ion [2,3]. Metal ions such as Bi^{3+} have shown to be an effective sensitiser for enhancing the infrared emission from the Yb^{3+} ion due to its broad absorption capabilities in the UV region as discussed in the previous chapters [2,4].

Aside from the luminescence properties of bulk powder phosphor materials, it is also important to study the luminescence properties of thin films as they are more practical, for use in luminescence devices such as, light sources, solar cells and in optical applications [5]. Thin

films are generally fabricated using two main deposition techniques namely, chemical and/or physical [6]. Chemical deposition techniques such as, spin coating and plating, involves a fluid precursor which undergoes a chemical reaction forming a thin solid layer on the surface of a substrate [7]. In physical deposition techniques, solid thin films are fabricated using a mechanical or thermodynamic process to ablate the material onto a given substrate using the PLD technique or by using electron beam evaporation [8]. Each of these techniques have their own set of advantages and disadvantages which greatly depends on the chemical and crystallinity of the phosphor material and also application of the film.

In this chapter, we fabricated the Y_2O_3:$Bi_{2.0\ mol\%}$,$Yb_{10.0\ mol\%}$ thin films using the PLD and spin coating deposition techniques. We also investigated how viscosity of the Y_2O_3:$Bi_{2.0\ mol\%}$,$Yb_{10.0\ mol\%}$ precursor solution, number of thin film layers, substrate temperature and deposition time influences the luminescence properties of the prepared thin films. Characterisation of the thin films were preformed using techniques such as XRD, AFM, SEM, EDS, TOF-SIMS and PL.

7.2 Experimental procedure

The Y_2O_3:$Bi_{2.0\ mol\%}$,$Yb_{10.0\ mol\%}$ thin films were prepared using the spin coating and PLD. In the spin coating technique Y_2O_3:$Bi_{2.0\ mol\%}$,$Yb_{10.0\ mol\%}$ phosphor powder was converted into a gel form using the sol-gel method discussed in section 3.2.2. The gel was diluted with ethanol in order to prepare a 0.2 M, 0.4 M and 0.7 M solution. The films were then prepared using the spin coating technique discussed at the end of section 3.3.1. In addition to varying the molarity of the sample solution, the number of coats were also increased to study its effect on the luminescence of the thin film while keeping the Y_2O_3:$Bi_{2.0\ mol\%}$,$Yb_{10.0\ mol\%}$ solution constant at 0.2 M.

For the PLD technique the target was prepared by mixing Y_2O_3:$Bi_{2.0\ mol\%}$,$Yb_{10.0\ mol\%}$ (10 g) phosphor powder with ethanol (100 µL, 99.9 %) and compressing it at 50 tons for 4 h to produce a pellet. The ethanol was used as a wetting agent which helps to compact the powder more evenly. The pellet was then annealed at 500 °C for 4 h to ensure that all the ethanol has been removed from the pellet. The distance separation between the target and substrate within the deposition chamber was set to 4 cm. The deposition chamber was evacuated until a base pressure of 1.9×10^{-5} mbar was reached. The chamber was then back filled with O_2 to a

background pressure of 2.7×10^{-2} mbar. The Nd:YAG laser frequency, wavelength and energy were set to 10 Hz, 266 nm and 40 mJ, respectively. The substrate temperature was set to 100 ^{o}C and 500 ^{o}C to study its effect on the morphology of the film. Additionally, a deposition time of 1 h and 2 h were used to investigate its effect on the luminescence properties of the thin film.

In addition to the above mentioned PLD prepared Y_2O_3:$Bi_{2.0\ mol\%}$,$Yb_{10.0\ mol\%}$ thin films, another set of thin films was prepared at the National Institute for Laser, Plasma and Radiation Physics in Bucharest, Romania. These films were deposited using a KrF laser with a pulse frequency, wavelength and energy parameter of 10 Hz, 248 nm and 200 mJ respectively. The distance between the target and substrate was also set to 4 cm. The substrate temperature was kept constant at 300 ^{o}C while the O_2 background pressure was 10^{-2}, 5×10^{-3}, 2.5×10^{-3} and 10^{-3} mbar, respectively in order to study the effect of background pressure on the morphology and luminescence of the films.

The phase structure was characterised from the XRD pattern which was obtained using a Bruker D8 Advance diffractometer with KαCu X-ray (1.54Å). The morphology and chemical composition were captured and measured using a Jeol-7800F Field Emission SEM equipped with an Oxford Artic EDS. A Shimadzu SPM-9600 AFM in contact mode was used to confirm the topography on the surface of the thin films. The elemental distribution of the thin film both on the surface and in the bulk, were obtained using a iontof ToF-SIMS^5 in the positive polarity mode, with the pulsed primary Bi^{3+} ion source set to 10 kHz with an accelerating potential of 30 kV and a current of 10 pA. The sputtering using a iontof ToF-SIMS^5 was carried out using a Ce sputter gun set to 1 kV and 75 nA. The emission properties were generated using a Kimmon IK Series He-Cd laser (325 nm) as the excitation source, while the emission was dispersed by a Horiba iHR 320 monochromator. The visible emission was detected using a PMT and the infrared emission was detected by an InGaAs solid state DSS-IGA020T detector.

The phase structure for the thin films prepared using the KrF laser PLD was characterised using grazing incidence X-ray diffraction (GIXRD) with a Panalytical Empyrean (The Netherlands) diffractometer. The diffractometer worked using KαCu X-ray (1.54Å) in a parallel beam geometry by means of a mirror in the incident beam and a beam collimator of 0.27° in front of the detector.

7.3 Results and discussion

7.3.1. Structural analysis

Figure 7.1 shows the XRD patterns of Y_2O_3:$Bi_{2.0\ mol\%}$,$Yb_{10.0\ mol\%}$ thin films prepared using the PLD technique with different substrate temperatures and deposition times. The pattern revealed that a mixture of crystal phases was present in the thin film that was synthesised at 100 °C for 2 h. The peak found at 28.9° was attributed to the cubic phase structure with a crystal orientation of (222) similar to the bulk material. The peak situated at 30.6° was due the monoclinic phase of Y_2O_3 with an orientation of (003) [9]. The cubic phase of Y_2O_3 consists of two symmetry sites, a S_6 symmetry which has an inversion centre (symmetric) and a C_2 symmetry that does not have an inversion centre (asymmetric). For the monoclinic phase, all the sites present within Y_2O_3 have a C_s symmetry with no inversion centres.

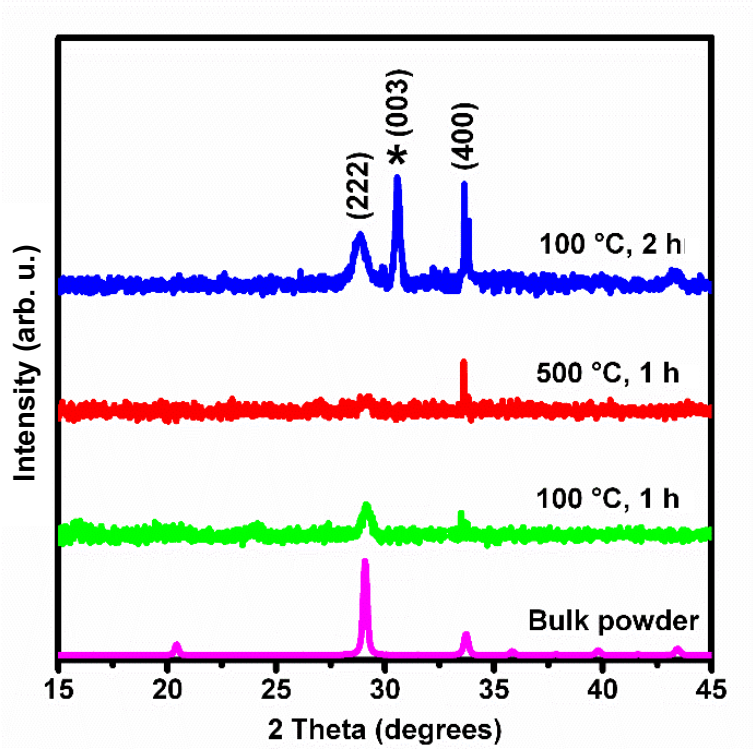

Figure 7.1: XRD spectrum of Y_2O_3:$Bi_{2.0\ mol\%}$,$Yb_{10.0\ mol\%}$ thin films synthesised using the Nd:YAG PLD at 100 °C and 500 °C substrate temperature and at 1 h and 2 h deposition time.

Figure 7.2 shows the XRD pattern for the Y_2O_3:$Bi_{2.0\ mol\%}$,$Yb_{10.0\ mol\%}$ thin films prepared using the KrF laser. With an increase in the O_2 background pressure a decrease in the crystallinity and formation of a more amorphous thin film was observed. Similar to the sample prepared at 100 °C for 2h using the Nd:YAG laser the (003) monoclinic phase of Y_2O_3 was also detected in all four samples.

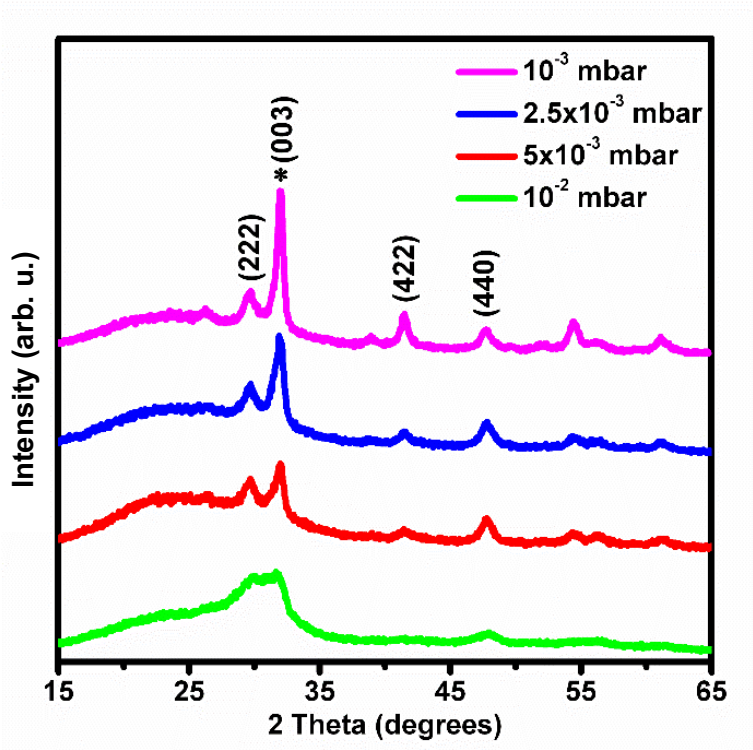

Figure 7.2: XRD spectrum of Y_2O_3:$Bi_{2.0\ mol\%}$,$Yb_{10.0\ mol\%}$ thin films prepared using the KrF PLD at O_2 background pressure of 10^{-3}, 2.5×10^{-3}, 5×10^{-3} and 10^{-2} mbar.

The XRD patterns for Y_2O_3:$Bi_{2.0\ mol\%}$,$Yb_{10.0\ mol\%}$ thin films synthesised at different molarities and an increasing number of coats using spin coating are shown in Figure 7.3a and Figure 7.3b, respectively. The crystallinity of the films matches well to the Y_2O_3:$Bi_{2.0\ mol\%}$,$Yb_{10.0\ mol\%}$ phosphor powder which indicates that the film formed as a single phase cubic structure. The broadness of the reflection peaks indicates that the particles are either very small or that they are semi-crystalline [10]. With an increase in both molarity and number of coats more defined peaks and an improved signal to noise ratio was observed, which was attributed to an overall thicker thin film being formed.

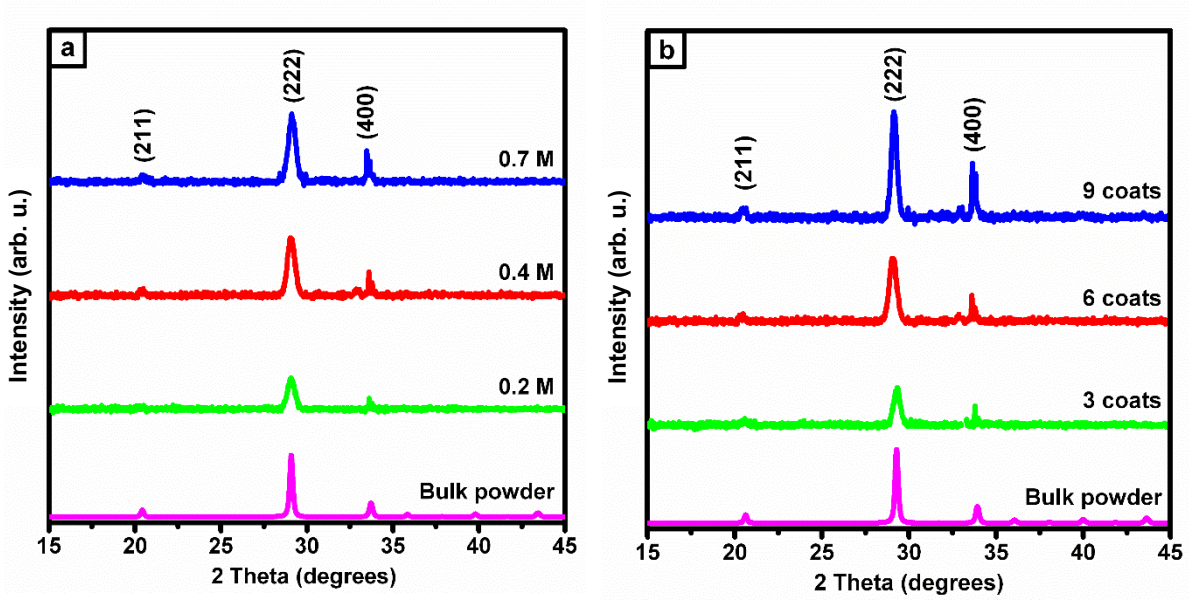

Figure 7.3: XRD spectrum of Y_2O_3:$Bi_{2.0\ mol\%}$,$Yb_{10.0\ mol\%}$ thin films prepared using (a) 0.2, 0.4 and 0.7 M Y_2O_3:$Bi_{2.0\ mol\%}$,$Yb_{10.0\ mol\%}$ solutions and (b) 3, 6 and 9 coats.

7.3.2. Morphological analysis

The SEM micrographs of Y_2O_3:$Bi_{2.0\ mol\%}$,$Yb_{10.0\ mol\%}$ thin films synthesised using the PLD technique with a deposition time of 1 h and 2 h under a constant substrate temperature of 100 °C are displayed in Figure 7.4.

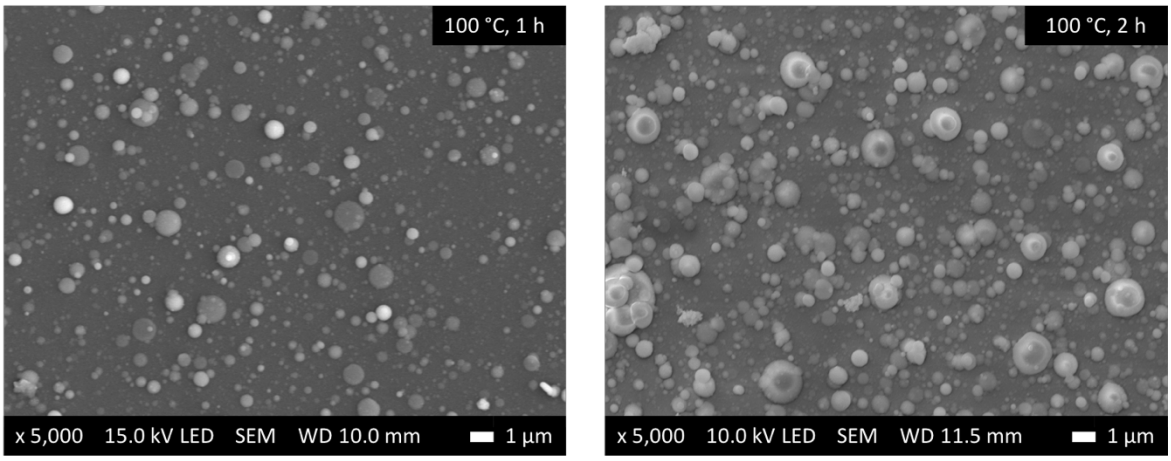

Figure 7.4: SEM micrographs for thin films prepared using the Nd:YAG PLD technique with a deposition time of 1 h and 2 h at a constant 100 °C substrate temperature.

The results show that the surfaces of the thin films were rough and consisted of round particles with varying sizes. The roughness and size of the particles were much more pronounced for the 2 h sample. There particles were present due to the laser ablation process which have an explosive-like nature producing particulates that travel alongside the ablation plume and collecting on the substrate. A SEM micrograph showing the effect of deposition time on the thickness on the thin film is shown in Figure 7.5. By doubling the deposition time, the cross-section SEM image showed that the thickness of the thin film has also approximately doubled as expected. Aside from the thickness of the thin film, the cross-sectional image also revealed that the particulates and agglomeration vary greatly in both their size and height which may influence the luminescence of the film at different areas.

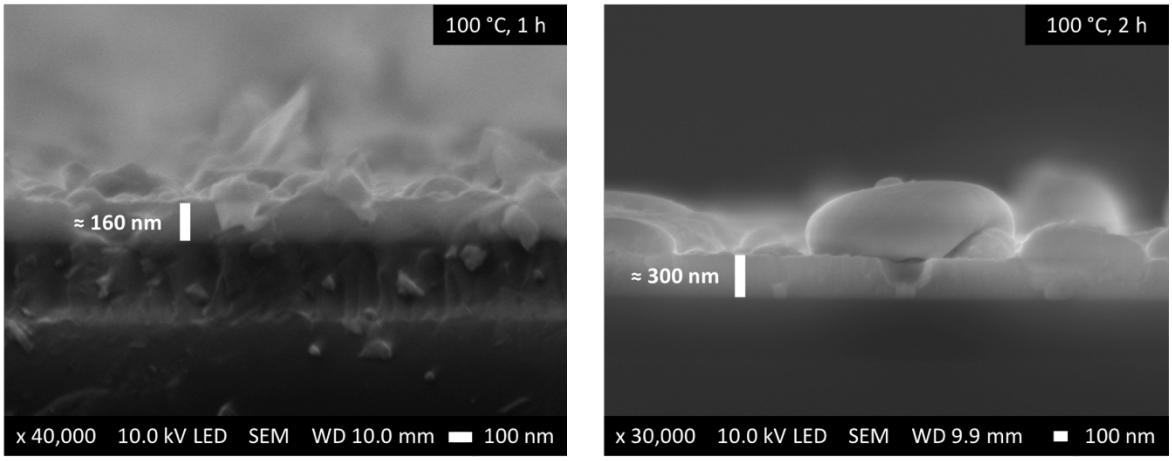

Figure 7.5: SEM micrographs for the thin film cross-section deposited by the Nd:YAG PLD under a constant substrate temperature with a deposition time of 1 h and 2 h.

The AFM analysis was preformed to study the effect of substrate temperature and deposition time on the topography of the thin films prepared using PLD. Figure 7.6 shows the AFM images of the surface of the thin film synthesised with a substrate temperature of 100 °C with a deposition time of 1 h and 2 h and the other film was prepared at 500 °C for 1 h. The images revealed that the substrates were covered with particles of varying shapes and sizes. With an increase in deposition time the substrate had a longer exposure to the ablation plume and particulates originating from the target, leading to an increase in both the size and amount agglomerations present on the substrate.

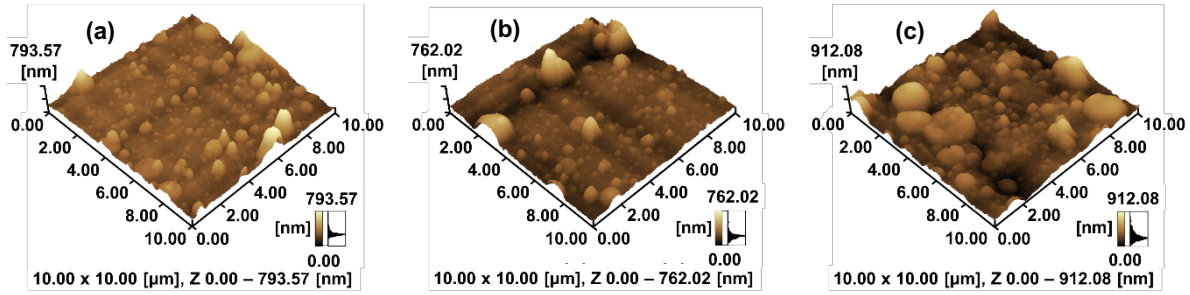

Figure 7.6: AFM image of Y_2O_3:$Bi_{2.0\ mol\%}$,$Yb_{10.0\ mol\%}$ thin films synthesised using the Nd:YAG PLD with a substrate temperature and deposition time of (a) 100 °C for 1 h, (b) 500 °C for 1 h and (c) 100 °C for 2 h.

Figure 7.7 shows the SEM images of the Y_2O_3:$Bi_{2.0\ mol\%}$,$Yb_{10.0\ mol\%}$ thin films prepared with a background O_2 pressure of 10^{-3} and 10^{-2} mbar using the KrF PLD system. From both SEM images, it can be seen that small particles similar to the ones shown in Figure 7.4 were also observed. This again was caused by the explosive-like nature associated with the laser ablation process. However, the number of particles present on the film was significantly less as compared to the films synthesised using the Nd:YAG laser and thus a significantly smoother PLD thin film was obtained using the KrF laser.

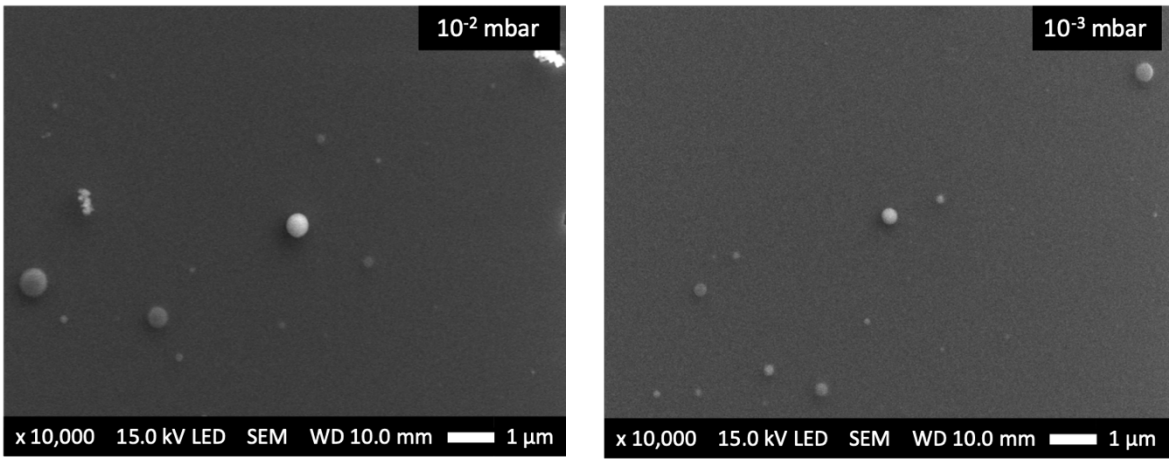

Figure 7.7: SEM micrographs of Y_2O_3:$Bi_{2.0\ mol\%}$,$Yb_{10.0\ mol\%}$ thin films synthesised using the KrF PLD with a background pressure of 10^{-3} mbar and 10^{-2} mbar.

SEM micrograph of thin films prepared at 0.2 M, 0.4 M and 0.7 M are shown in Figure 7.8. The SEM images shows that films prepared at a low molarity was much smoother that films prepared at higher molarities which were rough and dispersed with large agglomerations in the order of 100 µm.

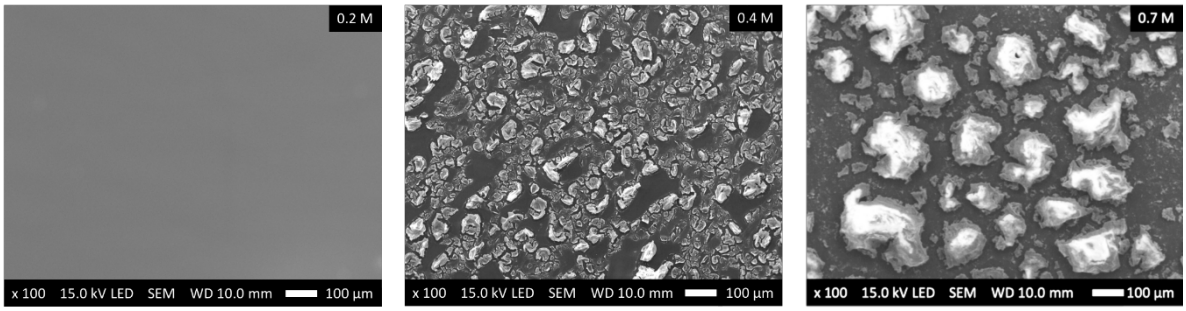

Figure 7.8: SEM micrographs for thin films prepared using the spin coating technique at 0.2 M, 0.4 M and 0.7 M.

Using the 0.2 M solution the number of coats applied on the silicon substrate was increased to study whether an increase in the thickness of the thin film would influence the morphology on the surface. Figure 7.9 shows the SEM micrographs of thin films prepared using the 0.2 M solution with an increase in the number of coats. The SEM micrographs show that at 3 coats the surface of the thin film was smooth with no agglomerations present. By increasing the number of coats cracks in the films started forming, increasing the number of coats even further lead to more cracking and peeling of the thin film. One major factor that may promote cracking and peeling is poor adhesion between the film and substrate, which are generally influenced by thermal, chemical processes and the misfit between the substrate and epilayer [11].

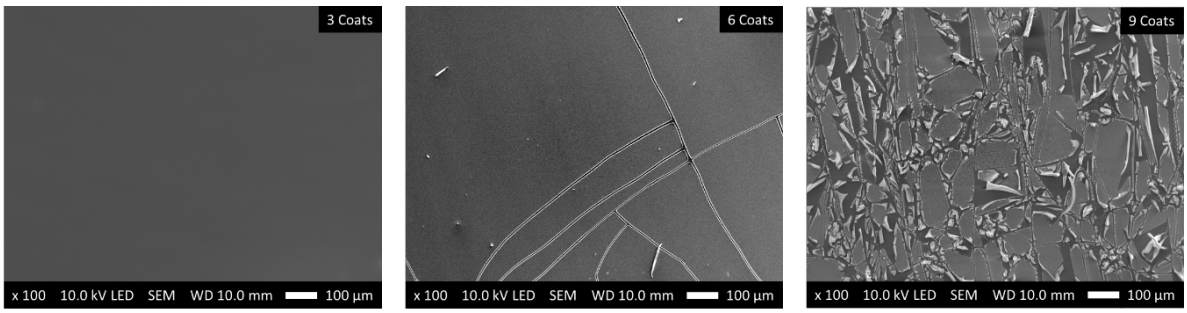

Figure 7.9: SEM micrographs for thin films synthesised using the spin coating technique at a constant 0.2 M with 3, 6, and 9 coats.

Figure 7.10 shows the AFM micrograph of Y_2O_3:$Bi_{2.0\ mol\%}$,$Yb_{10.0\ mol\%}$ thin films synthesised with 3, 6 and 9 coats. The region that was evaluated showed that the substrate containing 3 and 6 coats was well covered and the film was uniformly spread. The film prepared with 9 coats had regions where the films was fairly evenly formed but it also contained regions where the film was slightly rougher, which was related to the peeling effect seen in the SEM images. One

possible solution to eliminate the peeling and cracking of the films is by addition of a seed layer. The seed layer would be introduced on the surface of the substrate before the spin coating process to aid in adhesion [11].

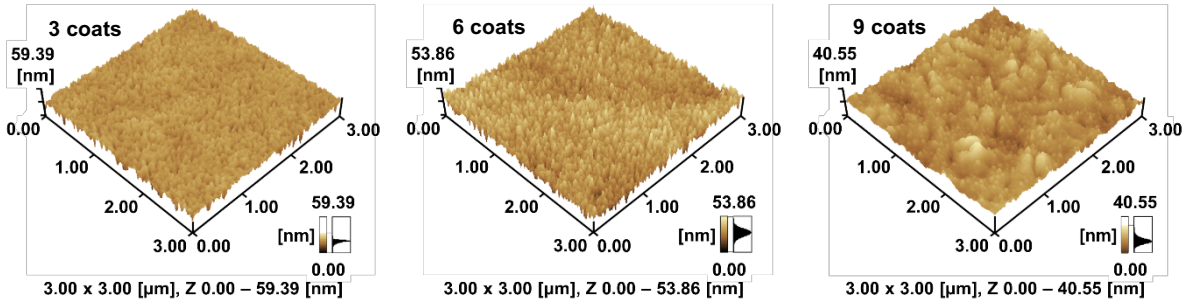

Figure 7.10: AFM image of spin coating thin films prepared with 3, 6 and 9 coats.

7.3.3. Compositional analysis

The EDS analysis technique was used to obtain the elemental composition of Y_2O_3:$Bi_{2.0\ mol\%}$; $Yb_{10.0\ mol\%}$ thin films synthesised using the PLD and spin coating and the results are displayed in Figure 7.11 – 7.13. The spectrums confirmed that Y, O, Bi, Yb and Si were all present as expected. From the elemental map it can be seen that all the dopants present within the host material are evenly distributed over the film when taking the distribution of the thin film into account.

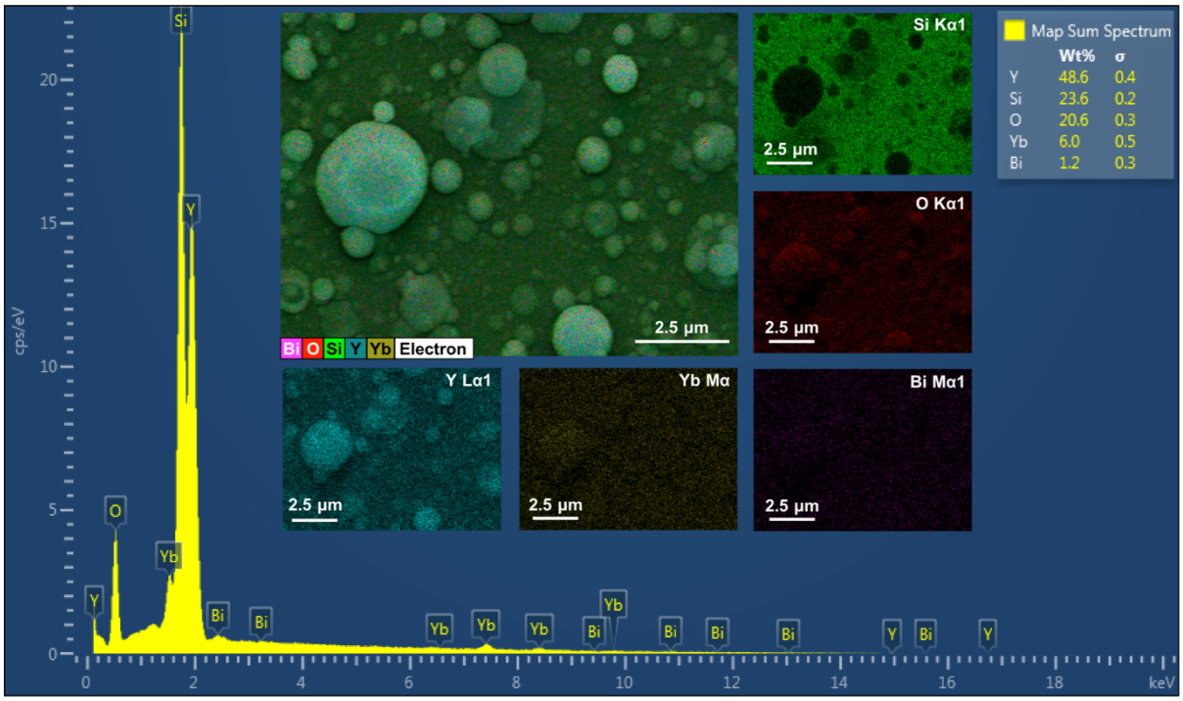

Figure 7.11: EDS spectrum and elemental mapping of Y_2O_3:$Bi_{2.0\ mol\%}$; $Yb_{10.0\ mol\%}$ thin films prepared using PLD under 2 h of deposition and at 100 °C substrate temperature.

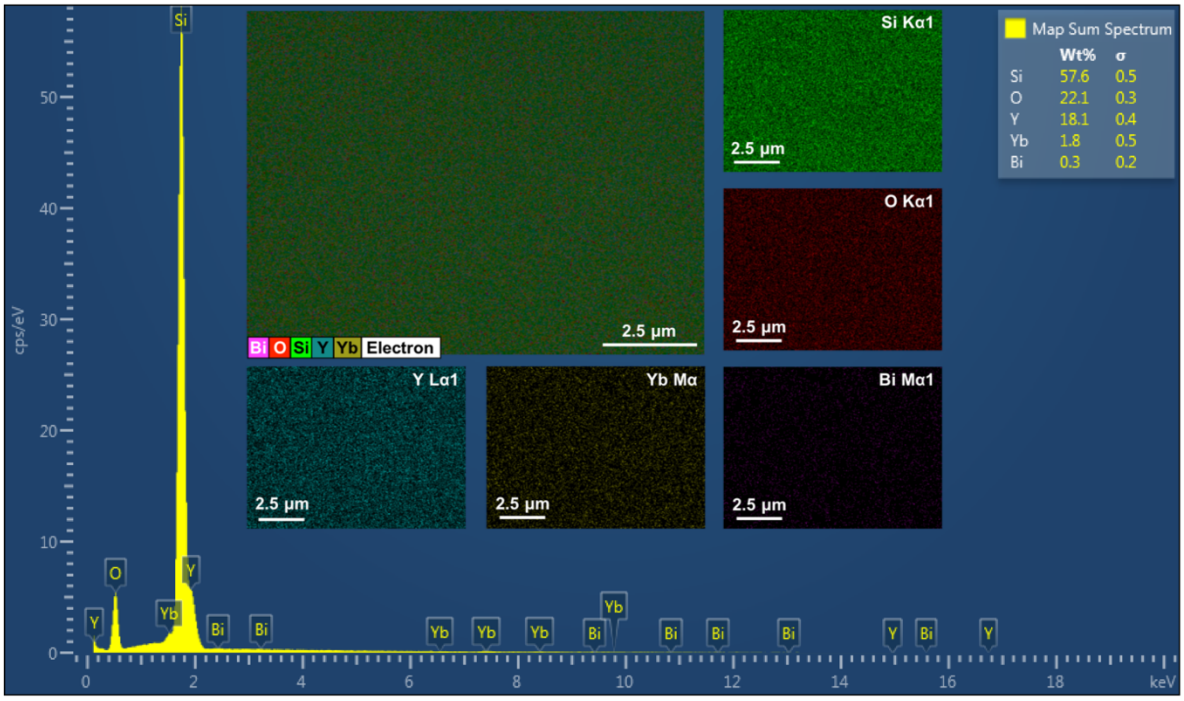

Figure 7.12: EDS spectrum and elemental mapping of Y_2O_3:$Bi_{2.0\ mol\%}$; $Yb_{10.0\ mol\%}$ thin film synthesised using spin coating with at a concentration of 0.2 M.

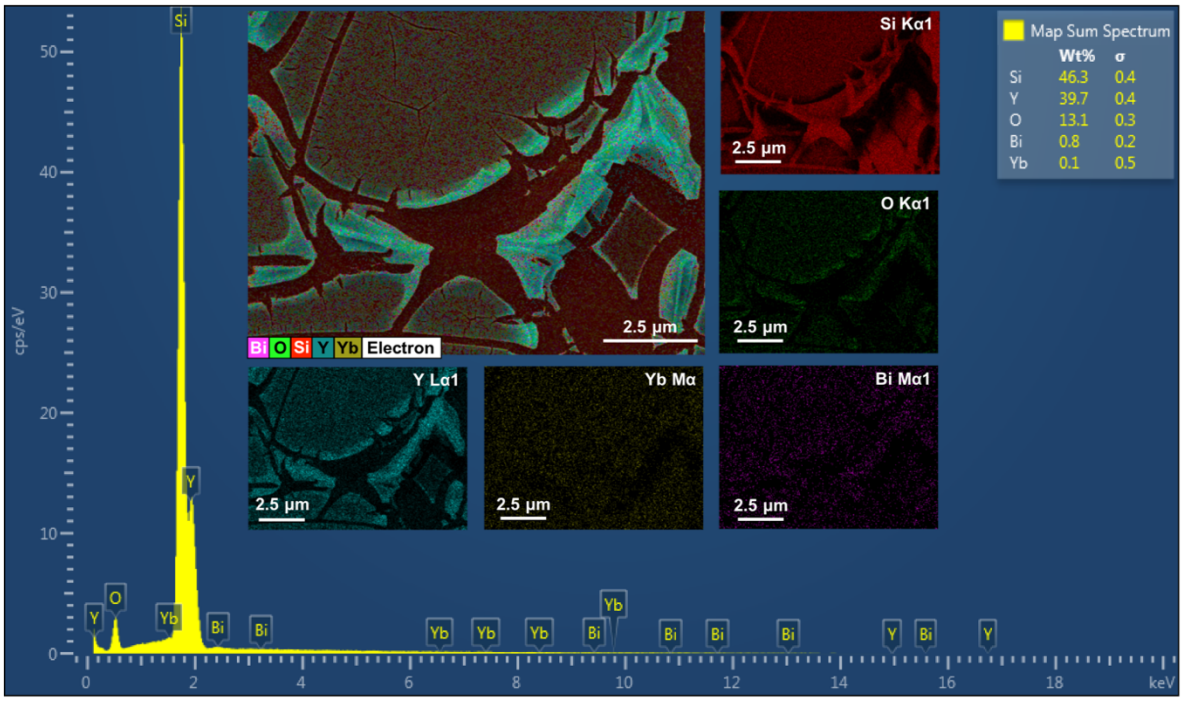

Figure 7.13: EDS spectrum and elemental mapping of Y_2O_3:$Bi_{2.0\ mol\%}$; $Yb_{10.0\ mol\%}$ thin film synthesised using spin coating with 9 coats and a solution concentration of 0.2 M.

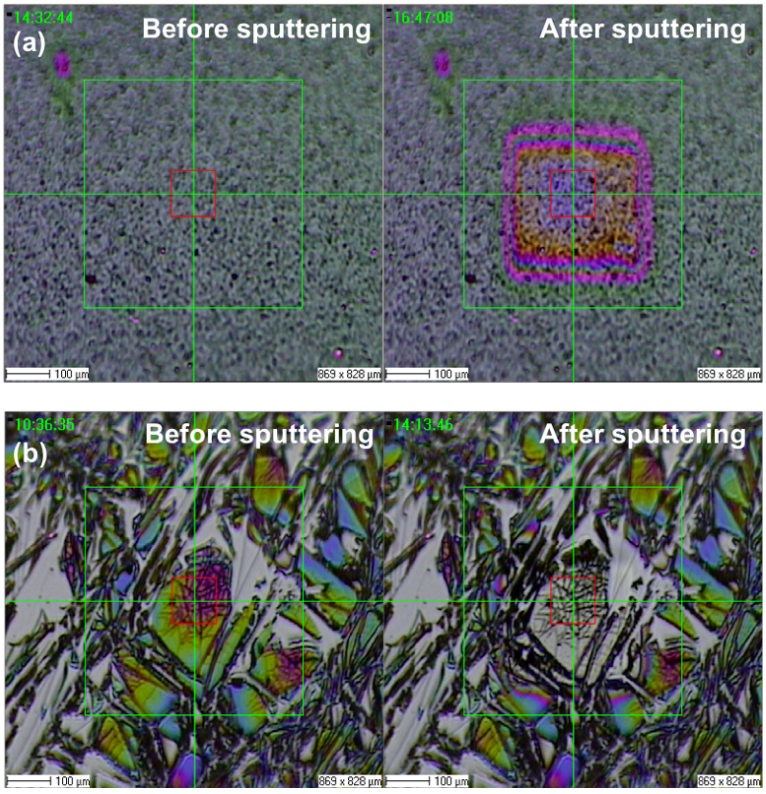

Figure 7.14: The optical image of Y_2O_3:$Bi_{2.0\ mol\%}$; $Yb_{10.0\ mol\%}$ thin films before and after sputtering. (a) PLD thin film prepared at 100 °C for 2 hrs and (b) spin coating thin film prepared using 9 coats with a 0.2 M solution.

In addition to the EDS, the TOF-SIMS analysis technique was also used to obtain the elemental distribution of the Y_2O_3:$Bi_{2.0\ mol\%}$,$Yb_{10.0\ mol\%}$ thin films. Figure 7.14 shows the optical image of the Y_2O_3:$Bi_{2.0\ mol\%}$,$Yb_{10.0\ mol\%}$ thin films prepared using PLD at 100 °C substrate temperature and 2 h deposition time and using spin coating where 9 coats of a 0.2 M solution was applied.

The analysis area is represented by the red block which has an area of 100 x 100 μm^2, while the area rastered by Bi was 300 x 300 μm^2 which can be seen in the after sputtering image where the thin film was sputtered away. The 3D false colour overlay showing the distribution of Y, Bi and Yb ion over a Si substrate is displayed in Figure 7.15. The result matches well to that already obtained from the EDS mapping results and showed that all the elements are well distributed both on the surface and in the bulk of the thin film. In Figure 7.15b some of the Y_2O_3:$Bi_{2.0\ mol\%}$,$Yb_{10.0\ mol\%}$ thin film appeared to have diffused into the Si substrate and also that some of the Si has penetrated the thin film. This effect is however not real and is caused by the topography of the thin film layer [12].

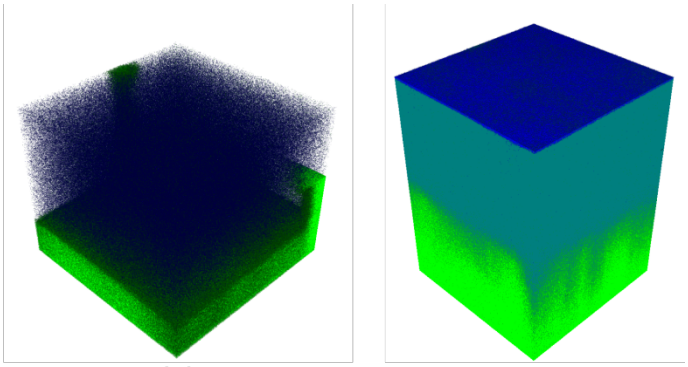

Figure 7.15: 3D overlay of Y^+, Bi^+, Yb^+ (blue) and Si^+ (green) showing the distribution of elements through the Y_2O_3:$Bi_{2.0\ mol\%}$,$Yb_{10.0\ mol\%}$ thin film prepared (a) using PLD at 100 °C for 2 h and (b) using spin coating where 9 coats were applied using 0.2 M solution.

7.3.4. Luminescence properties

Figure 7.16 shows the visible and infrared emission of PLD synthesised Y_2O_3:$Bi_{2.0\ mol\%}$,$Yb_{10.0\ mol\%}$ thin films. Under 325 nm excitation a broad visible emission centred at 495 nm originating from the $^1S_0 \rightarrow {}^3P_1$ transition of Bi^{3+} shown in Figure 7.16a [2,4]. With an increase in the

deposition time a thicker thin film was produced leading to an increase in the emission intensity. However, the cross-sectional SEM image showed that doubling the deposition time approximately doubles the thickness of the film, thus an emission with approximately double the intensity should have been observed. The main cause for the significantly greater intensity in the thin film deposited at 100 °C for 2 h was due to the presence of large particles that were present on the surface of the films. The SEM image showed with an increase in deposition an increase in the number of particulates present on the surface of the film also increased, thus increasing the emission intensity. A broad infrared emission related to the $^2F_{5/2} \rightarrow {}^2F_{7/2}$ transition of Yb^{3+} shown in Figure 7.16b was also observed under 325 nm excitation. The Yb^{3+} emission consists of a main sharp peak centred at 976 nm with several weaker peaks centred at 950 nm, 1030 nm and 1074 nm which originate due to the crystal field Stark splitting of the $^2F_{5/2} \rightarrow {}^2F_{7/2}$ transition [13].

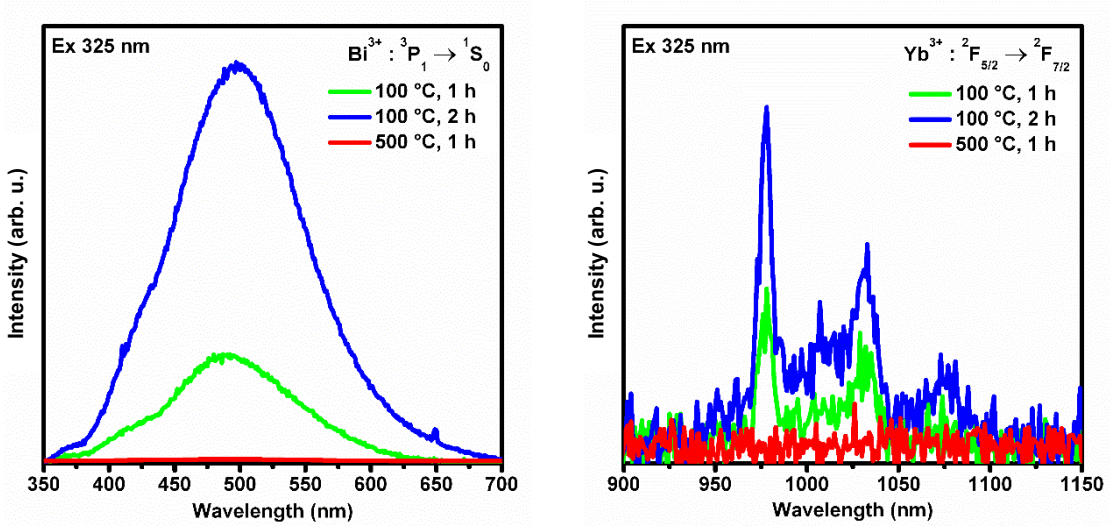

Figure 7.16: (a) Visible and (b) infrared emission of Y_2O_3:$Bi_{2.0\ mol\%}$,$Yb_{10.0\ mol\%}$ thin films synthesised using the PLD at substrate temperatures and deposition time of 100 °C for 1 h, 100 °C for 2 h and 500 °C for 1 h.

Figure 7.17 shows the visible emission spectra of Y_2O_3:$Bi_{2.0\ mol\%}$,$Yb_{10.0\ mol\%}$ thin films that were deposited on a glass substrate using a 248 nm KrF laser PLD system. Under 325 nm excitation a broad emission can be seen for all four thin film samples. The broad emission was not only originating from the film but rather a combination of the film and the glass substrate. In order to determine emission originating from the thin film the emission originating from the substrate was removed. This was done by obtaining an emission spectrum of a clean glass substrate,

shown by the red spectrum. The emission of the substrate was then normalised with respect to the 735 nm peak, as this peak does not originate from the thin film. The normalised spectrum (blue spectrum) was then subtracted from the initial emission spectrum (black spectrum), which yielded an emission (green spectrum) originating from the thin film.

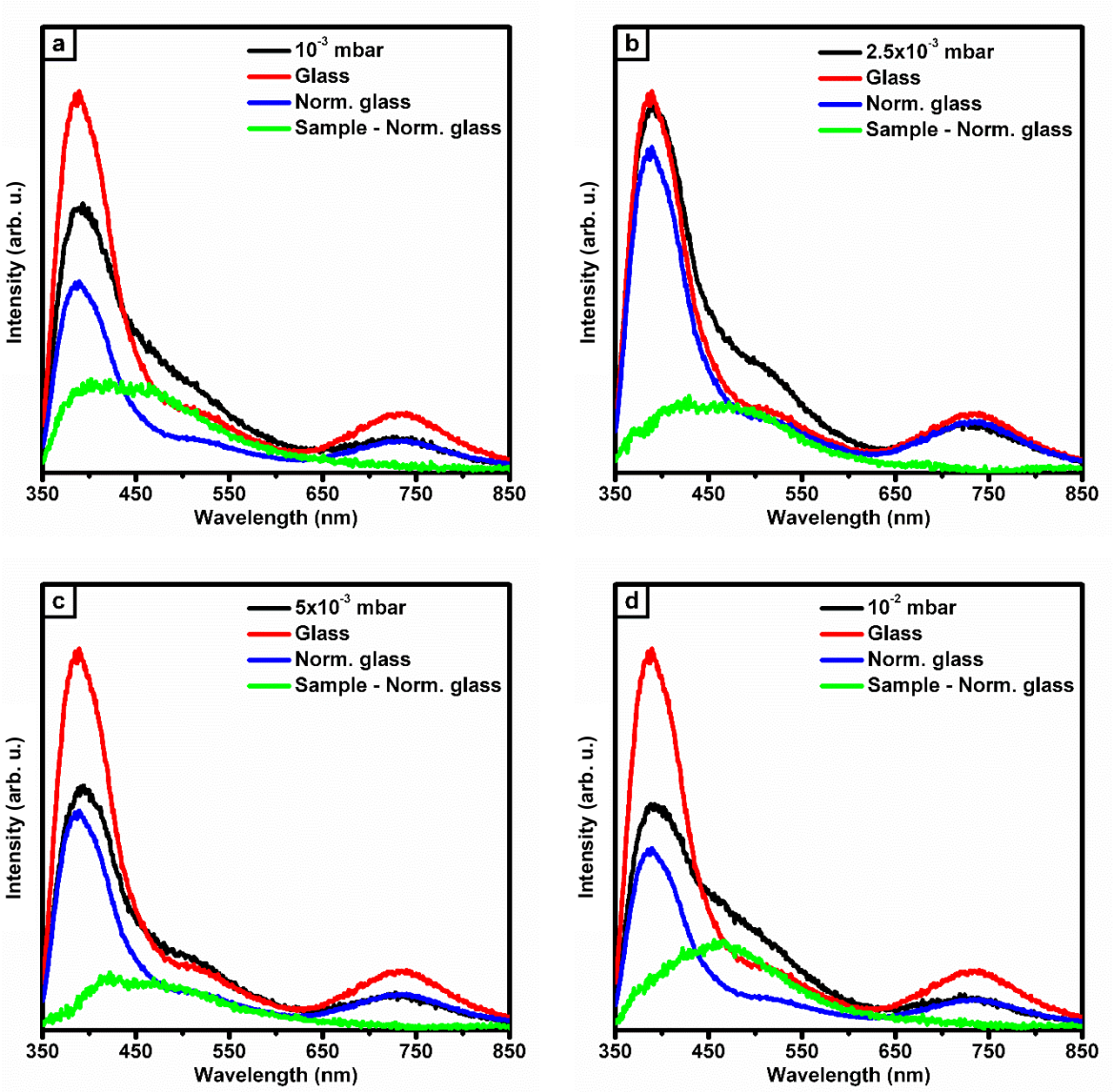

Figure 7.17: Visible emission (325 nm excitation) of Y_2O_3:$Bi_{2.0\ mol\%}$,$Yb_{10.0\ mol\%}$ thin films prepared using a KrF laser with an O_2 background pressure of (a) 10^{-3} mbar, (b) 2.5×10^{-3} mbar, (c) 5×10^{-3} mbar and (d) 10^{-2} mbar.

With an increase in the O_2 background pressure a shift in the emission of the film was observed, Figure 7.18. At low background pressures, the S_6 site emission (approximately 408 nm) of Bi^{3+} was more prominent. As the background pressure increased a shift towards the C_2 site emission

(approximately 495 nm) of Bi^{3+} was observed. This process may be related to the change in the crystallinity of the thin film as shown in Figure 7.3 where a decrease in crystallinity favours the C_2 emission rather than the S_6 site emission.

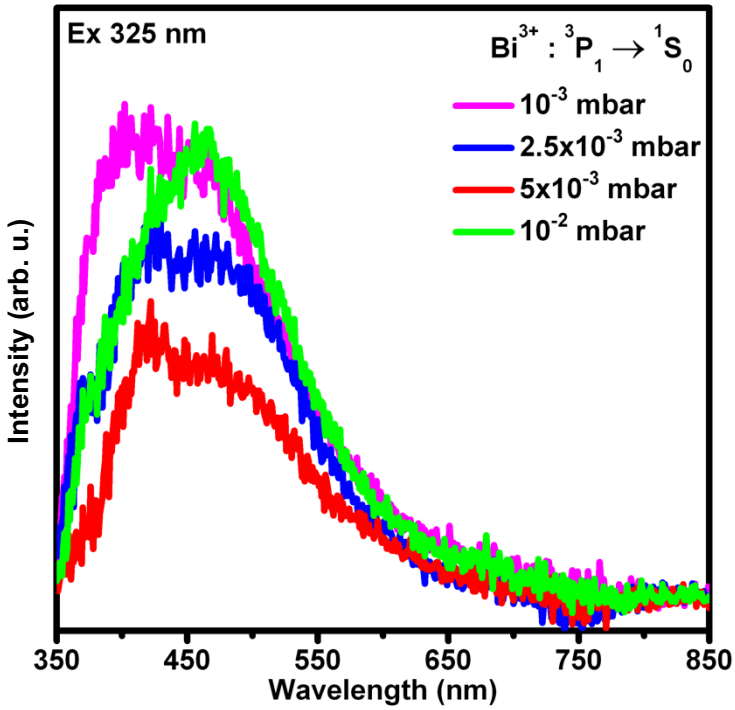

Figure 7.18: Visble emission after the subtraction of the substrate emission of Y_2O_3:$Bi_{2.0\ mol\%}$,$Yb_{10.0\ mol\%}$ thin films prepared at varying O_2 background pressures using the KrF laser PLD.

The visible emission spectrum of Y_2O_3:$Bi_{2.0\ mol\%}$,$Yb_{10.0\ mol\%}$ thin films prepared with varying molarities and increasing number of coats is shown in Figure 7.19. In both spectrums, a broad peak centred at 495 nm, related to the $^1S_0 \rightarrow {}^3P_1$ Bi^{3+} transition was observed. In Figure 7.19a an increase in molarity leads to a strong increase in the emission intensity of the thin films. A larger molarity means more of the phosphor material is present in the solution, thus more of the phosphor material is deposited onto the substrate during the spin coating process increasing the luminescence of the film. In Figure 7.19b an increase in the number of coats also leads to an increase in the emission intensity, however a linear relation between the emission intensity and the number of coats was expected. When doubling the coats from 3 to 6 coats a doubling in the emission intensity was observed but at 9 coats the emission intensity significantly increased. The main cause for the drastic increase in the emission intensity was the due to the

peeling of the thin film, this effect caused the films in some regions to fold over itself which increase the amount of material in that region and thus dramatically increasing the emission intensity. In the case of smooth layer, the effect of internal refection also plays a significant role in the emission intensity of the thin film as was pointed out by Coetsee et al [14,15]. Thin films which have a uniform layer, shown in Figure 7.20a, generally exhibits a large fraction of internal reflection due to the fairly small critical angle for transmission of photons, thus producing a lower emission intensity [15]. In less uniform thin films, shown in Figure 7.20b, photons are less internally reflected due to the shape of the particles and will therefore produce a higher emission intensity as compared to a uniformly smooth thin film [15].

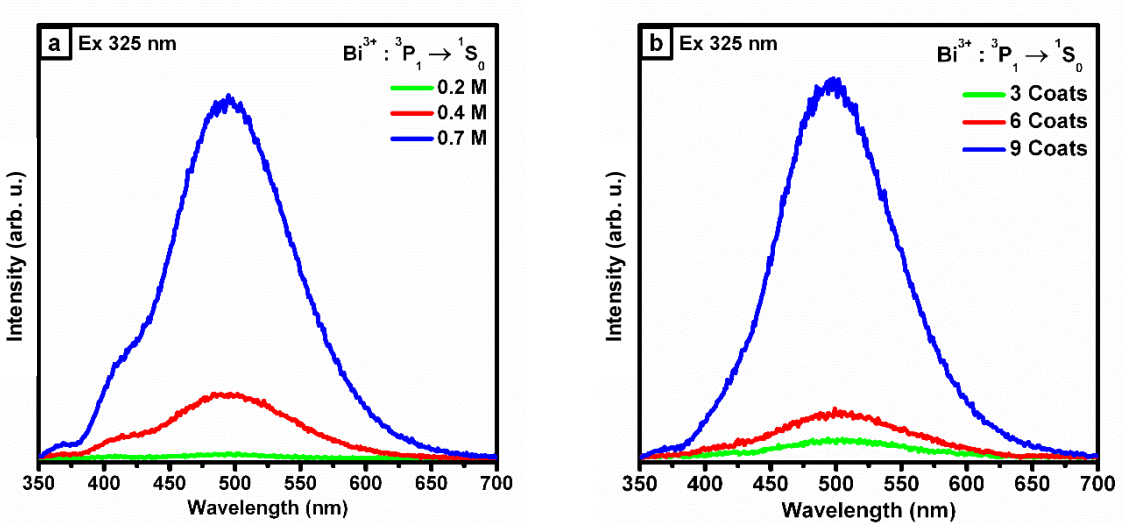

Figure 7.19: Visible emission (325 nm excitation) of Y_2O_3:$Bi_{2.0\ mol\%}$,$Yb_{10.0\ mol\%}$ thin films synthesised using the spin coating with (a) varying molarity and (b) increasing number of coats with a constant molarity.

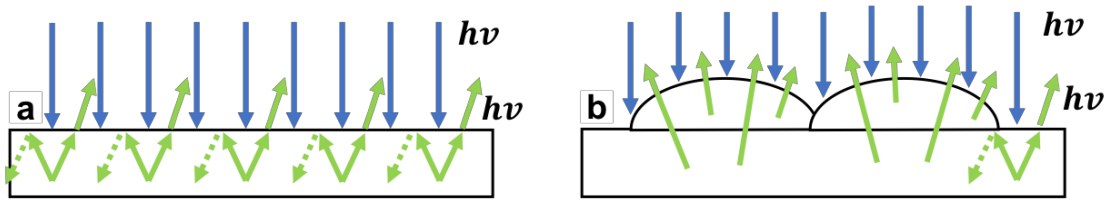

Figure 7.20: Schematic diagram of photons emitted from (a) a uniform thin film and (b) a thin film containing agglomerations.

Figure 7.21 shows the infrared emission of thin films prepared with varying molarities and increasing number of coats. The infrared emission intensities correlate well with the results obtained from the visible emission. In Figure 7.21a an increase in the molarity lead to an

increase in the emission intensity. By increasing the molarity, the amount of phosphor material present per volume of solution also increase thus more material is deposited onto the substrate during the spin coating procedure. Figure 7.21b shows the effect of increasing number of coats on the infrared emission intensity. By increasing the number of coats, the infrared emission greatly increases, due to the increasing thickness of the film, the peeling effect at higher number of coats and also the decrease in the internal reflection of the film.

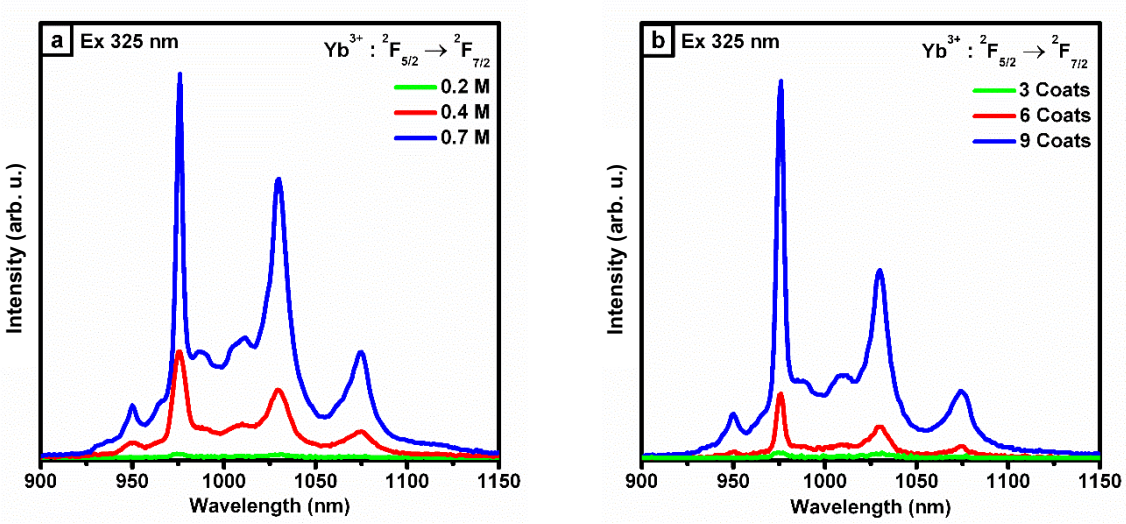

Figure 7.21: Infrared emission of Y_2O_3:$Bi_{2.0\ mol\%}$,$Yb_{10.0\ mol\%}$ thin films synthesised using the spin coating at (a) varying molarity and (b) increasing number of coats.

Finally Figure 7.22 shows visible emission spectrum for thin films the spin coating and the two PLD techniques which were normalised with respect to the maximum emission intensity of the KrF PLD sample. The results show that the emission obtained from the KrF laser prepared thin film was significantly weaker than the other preparation methods as can be seen from the signal to noise ratio. This low emission intensity could be attributed to the effect of internal reflection as the films prepared using the KrF laser were significantly smoother than the Nd:YAG laser prepared films. Both the Nd:YAG laser and spin coating prepared films provided strong emission intensities shown by the much high signal to noise ratio. Unfortunately, films prepared using these two methods were rough due to the presence of agglomerations. However smoother films were successfully prepared using the spin coating but had significantly lower emission intensities which was again due to internal reflection.

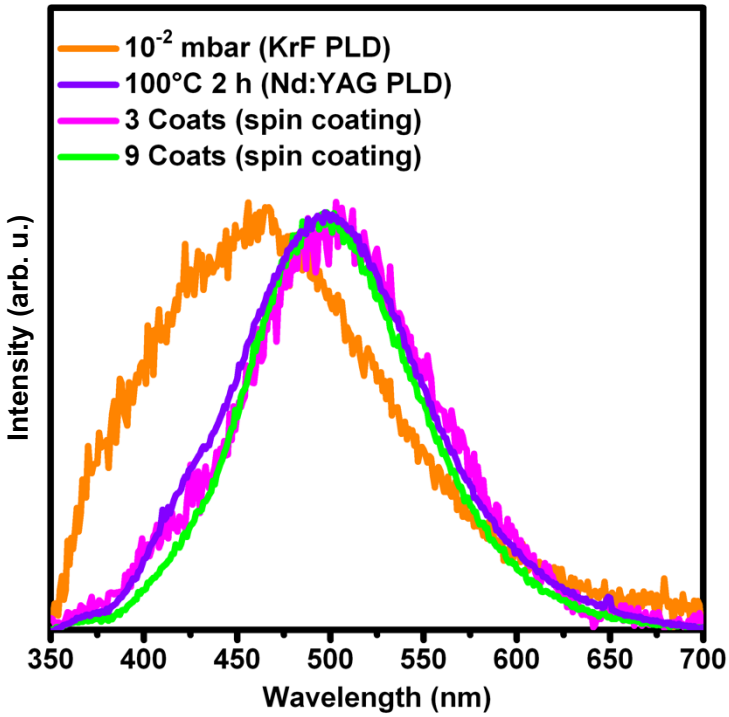

Figure 7.22: Normalised visible emission for thin films prepared using the spin coating and the two PLD techniques.

7.4 Conclusion

Y_2O_3:$Bi_{2.0\ mol\%}$,$Yb_{10.0\ mol\%}$ thin films were successfully synthesised using both the PLD and spin coating methods. With an increase in deposition time the XRD patterns revealed the formation of a monoclinic phase of Y_2O_3 with a (003) orientation. The SEM results showed that the Nd:YAG PLD system yielded a rough thin film scattered with small to large particles and that an increase in deposition time caused more and bigger particles to form while the KrF PLD system yielded a much smoother thin film. For the films deposited using the spin coating method an increase in the molarity of the spin coating solution also resulted in a rougher film where the phosphor material agglomerated over the surface of the substrate. By increasing the number of coats applied to the substrate while keeping the molarity of the spin coating solution fairly low, a smoother film was achieved. However, when more coats were applied, cracking and peeling of the films were observed caused by poor adhesion to the substrate. With an increase in deposition time, molarity and number of coats an increase in the luminescence emission intensities was observed. This is due to an increase in both the thickness and the amount of material deposited on the substrate as well as a decrease in total internal reflection

present due to rougher thin films. Varying of the O_2 background pressure, the PL emission showed that the S_6 was more predominant at the lower background pressure while a higher background pressure favoured the C_2 site emission.

7.5 References

[1] Y. Zhydachevskii, L. Lipi, "Broadband down-conversion in Bi^{3+} - Yb $^{3+}$ -codoped yttrium and yttrium e aluminum oxides", *Mater. Chem. Phys.*, **143,** 622–628 (2014)

[2] X. Y. Huang, X. H. Ji, Q. Y. Zhang, "Broadband downconversion of ultraviolet light to near-infrared emission in Bi^{3+}-Yb^{3+}-codoped Y_2O_3 phosphors", *J. Am. Ceram. Soc.*, **94,** 833–837 (2011)

[3] U. Rambabu, S. Do Han, "Broad band down conversion from ultra violet light to near infrared emission in YVO_4:Bi^{3+}, Yb^{3+} as spectral conversion phosphor for c-Si solar cells", *Ceram. Int.*, **39,** 1603–1612 (2013)

[4] W. Xian-Tao, Z. Jiang-Bo, C. Yong-Hu, Y. Min, L. Yong, "Quantum cutting downconversion by cooperative energy transfer from Bi^{3+} to Yb^{3+} in Y_2O_3 phosphor", *Chinese Phys. B*, **19,** 77804–77809 (2010)

[5] Y. Zhang, J. Hao, "Metal-ion doped luminescent thin films for optoelectronic applications", *J. Mater. Chem. C*, **1,** 5607–5618 (2013)

[6] D. A. Jameel, "Thin Film Deposition Processes", *Int. J. Mod. Phys. Appl.*, **1,** 193–199 (2015)

[7] L. B. Freund, S. Suresh, "Chemical vapor deposition", *in Thin Film Materials: Stress, Defect Formation and Surface Evolution* , Chapt. 1.2.2 9–10 *Cambridge University Press, United Kingdom*, (2003)

[8] L. B. Freund, S. Suresh, "Physical vapor deposition", *in Thin Film Materials: Stress, Defect Formation and Surface Evolution* , Chapt. 1.2.1 6–9 *Cambridge University Press, United Kingdom*, (2003)

[9] M. Cho, D. Ko, K. Jeong, S. W. Whangbo, C. N. Whang, S. C. Choi, S. J. Cho, "Structural transition of crystalline Y_2O_3 film on Si (111) with substrate temperature", *Thin Solid Films*, **349,** 266–269 (2000)

[10] Y.-Q. Zhai, L.-L. Wang, J. Chen, S.-H. Feng, "Synthesis of Blue-Green Phosphors $Sr_4Si_3O_8Cl_4$:Eu^{2+} by Gel-Combustion Method and Their Luminescent Properties", *J. Chem.*, **2013,** 1–6 (2013)

[11] A. Misra, M. Nastasi, "Fundamental aspects of residual stress evolution in thin metal films during energetic particle deposition", *in Adhesion Aspects of Thin Films: Volume 1* (ed. Mittal, K. L.) 17–30 *VSP, Zeist, The Netherlands*, (2001)

[12] A. Yousif, R. M. Jafer, J. J. Terblans, O. M. Ntwaeaborwa, M. M. Duvenhage, V. Kumar, H. C. Swart, "TOF SIMS induced artificial topographical effects on the $Y_2(Al,Ga)_5O_{12}:Tb^{3+}$ thin films deposited on Si substrates by the pulsed laser deposition technique", *Appl. Surf. Sci.*, **313,** 524–531 (2014)

[13] R. Simura, A. Jouini, J. H. Mun, A. Brenier, A. Yoshikawa, G. Boulon, T. Fukuda, "Growth and spectroscopic properties of Yb^{3+}-doped Sc_2O_3 crystals grown by the micro-pulling-down method", *Opt. Mater. (Amst).*, **30,** 18–21 (2007)

[14] E. Coetsee, H. C. Swart, J. J. Terblans, O. M. Ntwaeaborwa, K. T. Hillie, W. A. Jordaan, U. Buttner, "Characterization of Y_2SiO_5:Ce thin films", *Opt. Mater. (Amst).*, **29,** 1338–1343 (2007)

[15] E. Coetsee, J. J. Terblans, H. C. Swart, J. M. Fitz-Gerald, J. R. Botha, "Luminescence of Y_2SiO_5:Ce nanocrystalline thin films", *e-Journal Surf. Sci. Nanotechnol.*, **7,** 369–374 (2009)

Chapter 8: Conclusions and Future work

In this dissertation, a number of parameters regarding the synthesis of the Y_2O_3:Bi^{3+},Yb^{3+} phosphor material was addressed and optimised to obtain the optimum luminescence. The powders were successfully synthesised using the co-precipitation technique. The effects of the preparation environment and the concentration of the Bi^{3+} and Yb^{3+} ions on the luminescence properties of the Y_2O_3:Bi^{3+},Yb^{3+} phosphor powders were all determined.

The first parameter investigated was the pH of the solution during the synthesis of the Y_2O_3:Bi^{3+} phosphor. With an increase in the pH, an increase in both the crystallite size and the visible emission intensity was observed. The visible emission revealed that the Bi^{3+} ion might occupy one of two sites present in the Y_2O_3 host matrix, namely the S_6 and C_2 site. Both these sites have different emission wavelengths with the S_6 site having an emission wavelength of 409 nm and the C_2 site at 490 nm. The visible emission also revealed that the pH level had a minimal effect on which sites the Bi^{3+} ion will occupy, as the emission intensity ratio between the two sites remained constant with an increase in pH.

After the optimal pH was obtained (pH = 10) the next parameter that was analysed was the Bi^{3+} concentration present in the Y_2O_3 host. While keeping the pH constant the concentration of Bi^{3+} was varied from 0.5 to 5.0 mol%. The XPS and EDS showed that the Bi^{3+} ions were successfully and homogenously incorporated into the sample. The PL spectra showed that with an increase in Bi^{3+} concentration, an increase in the emission intensity was observed until a maximum at 2.0 mol% Bi^{3+} where it then sharply decreased. The drastic decrease in the emission intensity was due to concentration quenching, where energy was lost due to cross-relaxation between the Bi^{3+} ions. The CL spectrum revealed that with an increase in the Bi^{3+} concentration the probability of Bi^{3+} occupying the S_6 site decreased due to the limited number of S_6 sites available in the Y_2O_3 host matrix.

The third parameter that was investigated was the Yb^{3+} concentration. While keeping the pH level and Bi^{3+} concentration constant the Yb^{3+} concentration was varied from 2.0 to 40.0 mol%. The XRD showed that the Y_2O_3:Bi^{3+},Yb^{3+} samples still retained the single phase cubic structure of the host material even at a Yb^{3+} concentration of 40 mol%. The EDS spectra showed that both the dopants were homogenously spread throughout the sample. The PL

spectra revealed that with an increase in the Yb^{3+} concentration there was a decrease in the visible Bi^{3+} emission intensity due to possible energy transfer from the Bi^{3+} ions to the Yb^{3+} ions. In the CL spectra, an increase in the Yb^{3+} concentration yield an increase to the Bi^{3+} emission intensity originating from the S_6 site. That was probably caused by either the Yb^{3+} ions that forced more of the Bi^{3+} ions into the S_6 site or that the 500 nm C_2 site emission of Bi^{3+} was better utilised by the Yb^{3+} ions or even a combination of the two. Under UV excitation (325 nm) an increase in the infrared emission intensity was observed until a Yb^{3+} concentration of 10.0 mol% after which a decrease in the emission intensity was again observed due to concentration quenching. Utilising the optimal Bi^{3+} (2.0 mol%) and Yb^{3+} (10.0 mol%) concentrations the quantum efficiency of the Y_2O_3:Bi^{3+},Yb^{3+} powder phosphor was 24 % and 2 % for the visible and infrared emission, respectively under UV excitation. Under infrared excitation (980 nm) a green emission was detected which originated from the Er^{3+} impurities (present in the Yb_2O_3 starting material) and not the Bi^{3+} ions.

The final part of the study was to investigate the luminescence properties of Y_2O_3:Bi^{3+},Yb^{3+} phosphor as a thin film which were synthesised using the spin coating and PLD technique. XRD patterns showed that the Y_2O_3:Bi^{3+},Yb^{3+} thin films were successfully synthesised using both the spin coating and PLD technique. However, the Y_2O_3:Bi^{3+},Yb^{3+} thin film contained an addition monoclinic phase of Y_2O_3 in addition to the single phase cubic crystal structure. Films prepared using the spin coating technique were significantly smoother than those prepared using the PLD, although at higher molarities. With an increase in the number of coats, the films experienced peeling off from the substrate as they were unable to properly adhere to the substrate. The thin films were prepared using the PLD technique with two different lasers, a Nd:YAG laser and a KrF laser. The Nd:YAG laser produced significantly rougher films as compared to the KrF laser. This difference in the roughness can be attributed to the difference in the wavelength that was used during deposition or most likely the difference in the laser energy as the KrF laser pulse energy was five times higher than the Nd:YAG laser. The PL of the films varied greatly from the different techniques. Films that were prepared using the spin coating technique yielded good infrared emission whereas the PLD prepared films yield poor infrared emission. While in the visible emission, the PLD thin films instead yielded a stronger emission than the spin coated thin films. The weaker emission was attributed to the effect of internal reflection which may occur in films that are reasonably smooth.

Future work

This study serves as only a stepping stone in highlighting the use of phosphor materials in solar cell applications. Although phosphor materials are generally available in powder form, they serve their greatest potential in the form of thin films. However more work is required such as:

- Optimising both the techniques used to prepare the thin films such as the effect of annealing temperature on the luminescence properties of the phosphor powder.
- By introducing an alternative substrate preparation method such as the addition of a seed layer in order to determine how the surface texture of the substrate will affect the adhesion between the substrate and thin film.
- Varying more environmental parameters within the PLD chamber such as background gas pressure and the type of gas used in order to study their effects on both the morphology and the thickness of the thin films.
- Using a smooth thin film, controlled changes to the surface morphology will be manually introduced through chemical or laser etching to show how surface texturing will affect the luminescence properties of the thin film. The aim of surface texturing to help collect and direct most of the incident light onto the solar cell and to minimise the amount of incident light being reflected off the thin film or the solar cell, thus improving the overall efficiency of the solar cell.
- Applying the thin film to a commercial solar cell and its effect on the current, voltage and energy output to determine whether the efficiency of the solar cell could be improved. Finally, if the efficiency does improve, finding methods to produce such thin films on a larger scale for possible commercial use.